A new experimental setup for studies on wake flow instability and its control

by

Bengt E. G. Fallenius

April 2009
Technical Reports from
Royal Institute of Technology
KTH Mechanics
SE-100 44 Stockholm, Sweden

Akademisk avhandling som med tillstånd av Kungliga Tekniska Högskolan i Stockholm framlägges till offentlig granskning för avläggande av teknologie licentiatsexamen onsdagen den 6 maj 2009 kl 10.15 i sal E51, Osquars backe 14, Kungliga Tekniska Högskolan, Stockholm.

Universitetsservice US–AB, Stockholm 2009

Bengt E. G. Fallenius 2009, **A new experimental setup for studies on wake flow instability and its control**

Linné Flow Centre, KTH Mechanics, SE-100 44 Stockholm, Sweden

Abstract

A new experimental setup for studies on wake wake flow instability and its control, which has been designed and manufactured, is introduced and described. The main body is a dual-sided flat plate with an elliptic leading edge and a blunt trailing edge. Permeable surfaces enable boundary layer suction and/or blowing that introduce the feature of adjusting the inlet condition of the wake created behind the plate. This, in combination with a trailing edge that is easily modified, makes it an ideal experiment for studies of different control methods for the wake flow instability. Additionally, a vortex detection program have been developed in order to detect, analyse and compare small-scale vortical structures in the wake behind the plate for different inlet conditions and control methods applied to the wake flow. Instantaneous velocity fields behind a cylinder subjected to suction or blowing through the entire cylinder surface have been analysed with this program. The results of the analysis show that the major change for different levels of blowing or suction is the location of vortices while the most common vortex size and strength are essentially unchanged.

Preface

This Licentiate thesis in fluid mechanics treats the design of a new experimental setup, from which enhanced knowledge about how the hydrodynamic stability of the flow in the wake of a bluff body can be controlled. The thesis is divided into two parts, where the first part starts with a brief overview of bluff bodies and wake flows. This is followed by a description of the new setup and a Matlab® program that has been developed for vortex analyses of the particle image velocimetry measurements. The second part consists of two papers.

April 2009, Stockholm
Bengt Fallenius

Contents

Abstract iii

Preface iv

Part I. Overview and new setup

Chapter 1. Introduction 1

Chapter 2. Bluff bodies and wake flow 2
2.1. Bluff bodies 2
2.2. Wake flow 4

Chapter 3. New experimental setup 7
3.1. Boundary layer control 7
3.2. The Boundary Layer wind tunnel 8
3.3. Test section 9

Chapter 4. Vortex detection program 18
4.1. Definitions of a vortex 18
4.2. Velocity field filtering 21

Chapter 5. Summary 26

Chapter 6. Papers and authors contributions 27

Acknowledgements 28

References 29

Part II. Papers

Paper 1. Vortex analysis in the wake of a porous cylinder subject to suction or blowing 35

Paper 2. On the vortex generation behind a passive V-shaped mixer in a pipe flow 79

Part I

Overview and new setup

CHAPTER 1

Introduction

The flow around and in the near downstream region of bluff bodies is a research area that has caught the interest of many people for a long period of time. The main reason is the challenge to understand the physics of the flow. Another reason for the large interest is the large number of technical applications, where different flow phenomena occur. An example is the low pressure region behind vehicles travelling at high speeds that gives a drag force on the vehicle and hence, has a direct impact on fuel efficiency and road stability. Another is vibrations and fatigue in structures caused by periodic vortex shedding.

Learning how to control these phenomena, and the vortex shedding in particular, can lead to improved energy efficiency and reduction of noise and vibrations in high aspect ratio structures. In industrial processes such as papermaking, control of the wake instability would enable the manufacturing of multiple layer paper, which by use of rough unbleached fibres in the middle of the paper sheet would maintain or improve the quality while the cost and the load on the environment are reduced.

This thesis treats the design of a new experimental setup that aims at studies and the development of different methods to control the hydrodynamic instability of the wake behind bluff bodies. In addition, a tool to analyse the flow structures has been developed by means of a vortex detection program.

In times when computer capacity increases exponentially and the cost decreases, more complex events may be simulated and one might question the need for expensive experiments. Though, as the accuracy of the simulations increases, it is even more important to be able to validate the computer codes and find the real value of different physical parameters.

However, for high Reynolds number flows today's computers are still not fast enough to perform direct numerical simulations of the governing equations. Thus, turbulence modelling is required, which always have to be validated against accurate experimental data. Futhermore, at low Reynolds numbers, where interesting flow stability problems occur, there is today the possibility to numerically perform global mode stability analyses, which is performed on entire velocity fields and gives rise to large eigenvalue problems to be solved. There is thus a search for new experimental setups, which can produce data to test and validate numerical stability codes and physical boundary conditions.

CHAPTER 2

Bluff bodies and wake flow

In this chapter an overview of what can be called a bluff body is given and how a uniform stream is affected by its presence.

A two-dimensional body is a body with an arbitrary cross-sectional area, which is extended to infinity in the direction perpendicular to this area. The flow around a body can be considered two-dimensional[1] if the aspect ratio, defined as the extension width over the equivalent diameter of the cross-section, is large enough. This means that the end-effects do not influence the flow at the centre of the body. However, in a mean velocity perspective the flow will always be two-dimensional provided that the aspect ratio is large enough (see e.g. Norberg 1994). In the following we are assuming two-dimensional flow.

2.1. Bluff bodies

The drag force on objects placed in a flow can be divided into two parts, namely skin friction drag $F_{D,f}$, which is due to the boundary layer formation and the pressure drag $F_{D,p}$, also denoted form drag, which is due to the pressure distribution around the object.

In figure 2.1 a simple example is shown. A two dimensional cylinder with the perimeter $c = c(r, \theta)$, is subjected to a uniform velocity field (U_0), which causes tangential wall-shear stress $\tau_w = \tau_w(r, \theta)$ and a pressure distribution $p = p(r, \theta)$ around the body. The corresponding skin-friction drag per unit width ($F'_{D,f}$) is given by the integrated wall-shear stress projected in the direction parallel to the oncoming uniform velocity field as

$$F'_{D,f} = \int_{c(r,\theta)} \tau_w(r, \theta) \sin\theta \ \mathrm{d}s \ , \tag{2.1}$$

where $\mathrm{d}s = r\mathrm{d}\theta$ is the path along the perimeter c. The pressure difference in the streamwise direction is obtained through direct integration around the body after projecting $p\mathrm{d}s$ in the direction parallel to the oncoming uniform velocity field. The result is the form drag per unit width ($F'_{D,p}$), which is obtained as

[1]Note, for high enough Reynolds numbers (see section 2.1) physical flow phenomena will introduce 3D effects and consequently the two-dimensionality will be altered.

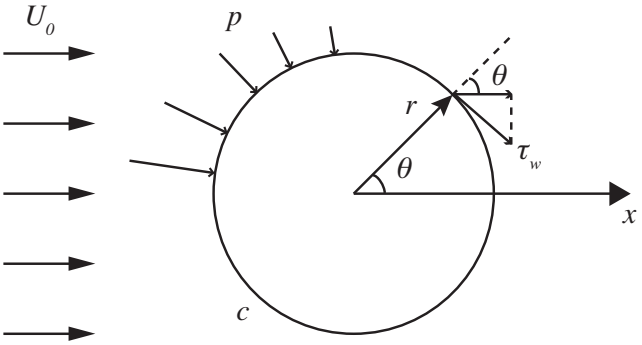

FIGURE 2.1. Drag forces acting on the cylinder. The drag on a cylinder may be divided into a pressure/form (p) and skin-friction (τ_w) contribution.

$$F'_{D,p} = \int_{c(r,\theta)} p(r,\theta)\cos\theta \ \mathrm{d}s \ . \tag{2.2}$$

The sum of the two drag contributions gives the total drag force of the body as,

$$F_{D,tot} = (F'_{D,f} + F'_{D,p}) \cdot L_w \ , \tag{2.3}$$

where L_w is the extension width of the two-dimensional body. Generally speaking there are two types of bodies with very different flow characteristics. The first type are aerodynamically smooth bodies, which are found in many engineering applications where a low drag and/or high lift is desired, such as airplane wings and similar bodies that end with a continuously decreasing thickness in the streamwise direction. The second type is the opposite of an aerodynamically shaped and body, i.e. bluff bodies, which typically has a blunt trailing edge and separated flow somewhere around the surface of the body. This makes the pressure recovery around the body incomplete and hence gives a contribution to the pressure drag. To illustrate how different the total drag is between these two types of bodies an example is given below.

Example
Consider two objects placed in a free stream with the velocity U_∞, kinematic viscosity ν and density ρ. One of the bodies is a cylinder with the diameter d and the other is a NACA 0018 airfoil[2].

The Reynolds number (Re) is a flow parameter, which is defined as a characteristic velocity times a characteristic length of the flow over the kinematic viscosity. This parameter can be seen as the ratio between flow destabilising

[2]The number 0018 states that the maximum thickness of the airfoil is 18% of the chord.

forces, i.e. inertia forces, and flow stabilising forces, i.e. viscous forces. For the flow around a cylinder the Reynolds number becomes

$$Re = \frac{U_\infty d}{\nu} \,, \tag{2.4}$$

where d is the diameter. If Re is set to 2000, the drag coefficient $C_D = F'_D/(q_\infty d)$ is about unity. Here, $q_\infty = 0.5\rho U_\infty^2$ is the dynamic pressure and F'_D denotes drag force per unit width. To obtain the same F'_D of the airfoil the chord length has to be about $100d$, which gives a Reynolds number based on the chord of about 2×10^5. Hence, the thickness of the airfoil that gives the same drag force per unit width as the cylinder is $18d$. In figure 2.2 the two bodies are shown according to scale.

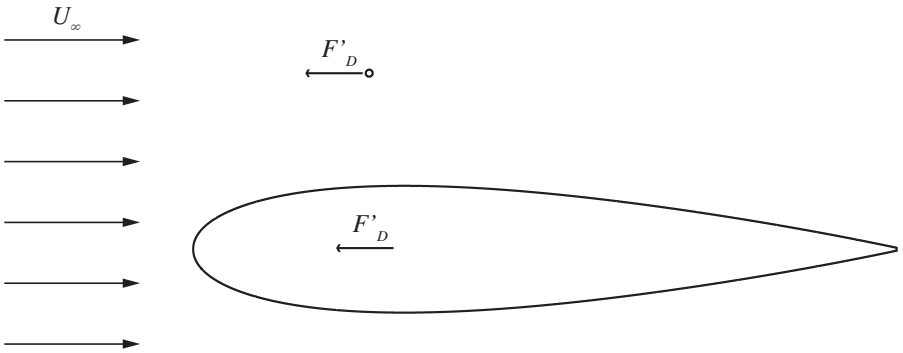

FIGURE 2.2. The drag force caused by the flow on a cylinder with diameter d is the same as for a airfoil with a maximum thickness of $18d$ and a chord of $100d$. Note, the figure is according to scale.

2.2. Wake flow

As illustrated in the previous section, the drag force on an object is not solely determined by its frontal area. It is rather the shape of its trailing edge, which is important. A blunt trailing edge gives rise to a low-pressure region, also called the near wake.

The size of such a wake is governed by the Reynolds number that depends on the free stream velocity and the size of the object. Depending on the geometry of the body, there can be sudden changes of the wake flow properties at different Reynolds numbers (see section 2.1). As an example, one can look at the drag coefficient for a circular cylinder. In the range $10^2 < Re < 10^5$ it is close to unity, while at $Re \sim 10^5$ it drops suddenly down to about 0.3, whereafter it subsequently increases and levels out again at $Re \sim 10^7$ to about

0.6. For a smooth cylinder, the drop is due to formation of separation bubbles and boundary layer transition to turbulence on the cylinder surface. The drag coefficient for a square cylinder behaves differently, it is constant equal to 2 for Reynolds numbers within the range of incompressible flow, since the separation points do not move from the sharp leading edges. Although, rounding of the corners of the square cylinder makes the drag coefficient change towards that of a circular cylinder.

Another important phenomenon is the periodic vortex shedding that occurs behind objects with a blunt trailing edge. It is characterised by the alternating shedding of vortices from the two sides of the object. This phenomenon is also Reynolds number dependent and sets in at around $Re = 40 - 50$ for a circular cylinder and around $Re = 115 - 125$ for a square cylinder, depending on the flow quality. The frequency of the periodic shedding can be estimated through the Strouhal number (St), a non-dimensional frequency, given as

$$St = \frac{fd}{U_\infty} \ , \tag{2.5}$$

where f is the frequency of the periodic shedding. The Strouhal number varies with geometry and Re. However, for Re in the range $10^2 - 10^5$ the Strouhal number is almost constant, 0.2 and 0.13 for the circular and square cylinder, respectively. For rectangular cylinders it depends on the aspect ratio l/d, where l is the streamwise length of the object.

The periodic vortex shedding induces alternating positive and negative side forces, which can induce vibrations of the object. This can be a source of noise and other interferences. In worst case the shedding frequency coincides with the eigenfrequency of the structure/object, which can lead to material fatigue and structural failure. An example of this was the Tacoma Narrows bridge in the state of Washington, USA, which soon after its construction in 1940 started to oscillate with an increasing amplitude until the central part of the bridge broke apart and fell down into the water.

The vortex shedding phenomenon is purely two-dimensional and is called the von Kármán vortex street after Theodore von Kármán (see Kármán 1912), who first studied and described this phenomenon. Figure 2.3 shows a NASA satellite image that captures an area of 365×150 km^2 near the island of Jan Mayen in the north Atlantic ocean. In the image one may observe a von Kármán vortex street evolving downstream of the Beerenberg volcano that raises 2200 m above the sea level. The stratified layers in the atmosphere makes the flow locally two-dimensional around the otherwise three-dimensional volcano.

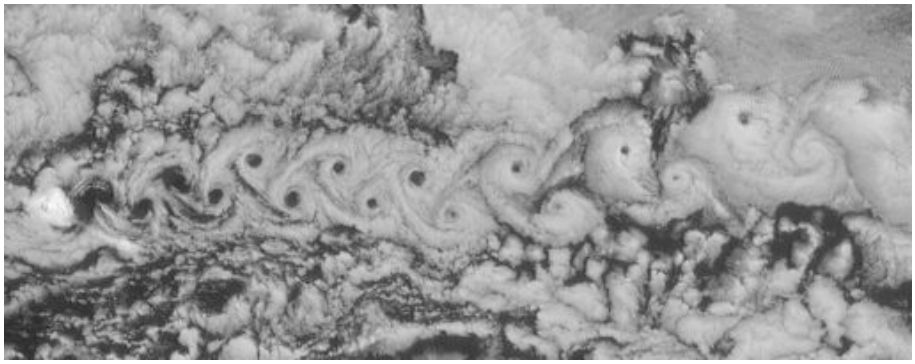

FIGURE 2.3. A more than 300 km long von Kármán vortex street near the island of Jan Mayen. (NASA)

CHAPTER 3

New experimental setup

A new experimental setup for studies on wake flow instability and control, including a new test section, has been designed and built at the department of Mechanics, KTH. The setup consists of a flat plate, from here on denoted rectangular forebody, with an elliptic leading edge and a blunt trailing edge. Permeable surfaces on both sides of the rectangular forebody add the unique feature of being able to vary the boundary layer along the body and thereby the inlet flow condition of the wake. In addition, the blunt trailing edge is interchangeable, enabling various means of base flow control.

3.1. Boundary layer control

Modulation of the boundary layer profile at the trailing edge of the rectangular forebody, i.e. the inlet condition of the wake, is managed by withdrawal and/or injection of air through the permeable surfaces by applying suction and/or blowing, respectively. Suction reduces the boundary layer thickness and at sufficiently high levels it will completely disappear. A special case of boundary layer suction is the so called asymptotic suction boundary layer (ASBL). The analytical expression for the ASBL profile was first derived by Griffith & Meredith (1936), but was not fully experimentally verified until 2003 by Fransson & Alfredsson. The expression for the streamwise velocity component in the ASBL reads

$$U(y) = U_\infty \left(1 - e^{yV_0/\nu}\right) \ , \tag{3.1}$$

where U_∞ is the free stream velocity, $V_0 = \text{const.}$ is the suction velocity, y is the wall-normal direction and ν is the kinematic viscosity. Note, here V_0 is defined as being negative, implying that $U \to U_\infty$ as $y \to \infty$. The analytical expression (3.1) enables direct integrations of the integrands corresponding to the displacement (δ_1) and the momentum loss thickness (δ_2), which result in

$$\delta_1 = \int_0^\infty \left(1 - \frac{U(y)}{U_\infty}\right) \mathrm{d}y = -\frac{\nu}{V_0} \tag{3.2}$$

and

$$\delta_2 = \int_0^\infty \frac{U(y)}{U_\infty}\left(1 - \frac{U(y)}{U_\infty}\right) \mathrm{d}y = -\frac{1}{2}\frac{\nu}{V_0} \ , \tag{3.3}$$

respectivly. This means that the shape factor $H = \delta_1/\delta_2$ is equal to 2. The boundary layer thickness δ_{99}, defined as the wall distance where U reaches 99% of U_∞, becomes

$$\delta_{99} = \frac{\nu}{V_0}\log(0.01) = \delta_1 \log(100) \ . \tag{3.4}$$

In the asymptotic suction region the Reynolds number based on the displacement thickness becomes

$$Re = \frac{U_\infty \delta_1}{\nu} = -\frac{U_\infty}{V_0} \ . \tag{3.5}$$

This provides the ASBL with a unique feature, namely, that one may vary the Reynolds number and the boundary layer thickness independent of each other.

3.2. The Boundary Layer wind tunnel

The Boundary Layer (BL[1]) wind tunnel is located at the department of Mechanics at KTH, and has been chosen as the experimental facility to host the new setup. The idea with the BL tunnel is to have a short time swap between different experiments by having exchangeable test sections. Below a brief description of the wind tunnel is given. For a more thorough description the interested reader is referred to Lindgren (2002).

The BL wind tunnel is a closed circuit tunnel, powered by an 15 kW axial fan. It was the first tunnel where expanding corners were utilised, making it possible to have a 9:1 contraction ratio together with an short overall wind tunnel length. The space for the testsection if 4.2 m and the cross sectional area of the contraction outlet is 0.5×0.75 m^2. The maximum flow velocity is 48 m/s and the turbulence levels[2] are 0.04%, 0.06% and 0.04% in the streamwise, wall-normal and spanwise directions, respectively, at the nominal[3] free stream velocity of 25 ms^{-1}. At this nominal velocity the variation in total pressure is less than $\pm 0.1\%$ and the variation in temperature is less than ± 0.07 °C over the cross sectional area.

---

[1] BL also corresponds to the initials of the wind tunnel designer Björn Lindgren.

[2] The following turbulence levels correspond to the high-pass filtered intensities, with a cut-off frequency of 20 Hz.

[3] During the design of the BL-windtunnel, most of the planned experiments were aimed for a free stream velocity of 25 ms^{-1}.

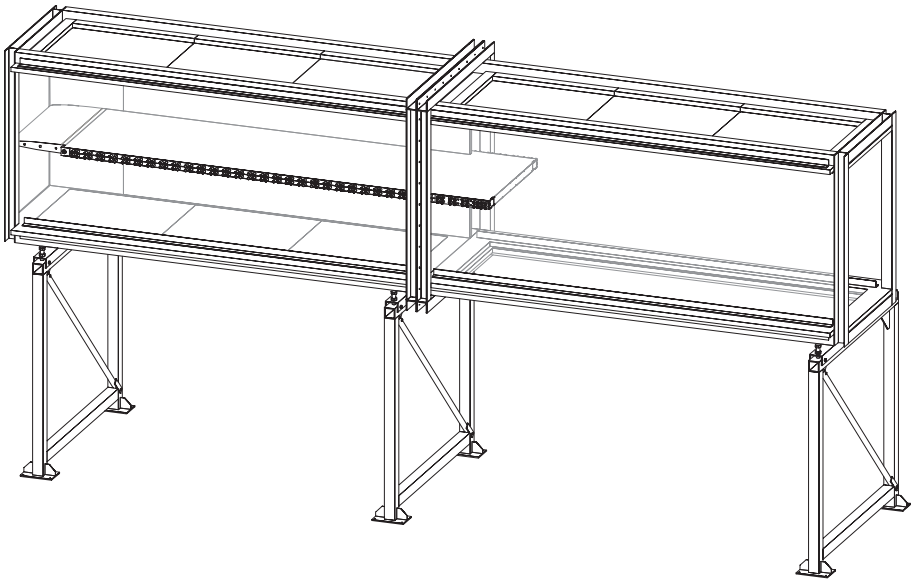

FIGURE 3.1. The main body mounted in the new test section of the wind tunnel. Tubing and meausurement equipment excluded.

3.3. Test section

The new experimental setup consists of a main body, which is mounted into a new exchangeable test section, see figure 3.1. The test section is based on two steel frames and has a total length of 4 m. Plexiglas together with plywood have been used for the walls since a high level of optical access is desired for measurements with high speed Stereoscopic Particle Image Velocimetry (S-PIV). Top and bottom walls have hatches for easy access into the test section important both for adjustments and cleaning.

3.3.1. *Main body*

The main body in the new experimental setup is symmetric, i.e. a dual-sided plate with permeable surfaces. Changing the pressure difference across the permeable surfaces will affect the boundary layer growth along the plate and consequently the inlet condition of the wake.

In figure 3.2 a schematic of the main body shows the principle and its feasibility. Note, the dimensions are not according to scale due to the high aspect ratio of the body. The co-ordinates are defined as, x in the streamwise direction, y normal to the body and z in the spanwise direction. The corresponding velocity components are U, V and W, respectively. A free stream flows past the body with the streamwise velocity U_∞. In the schematic the

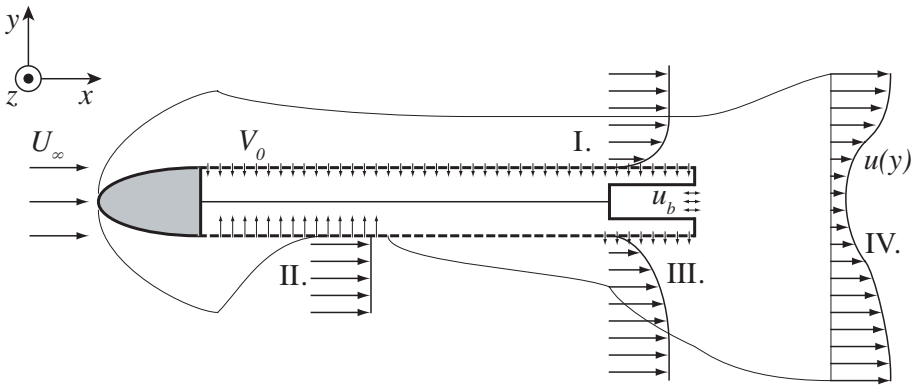

FIGURE 3.2. Schematic of the the bluff body in the new setup. Note, not according to scale.

upper side of the body is subjected to suction through the permeable surface, with the uniform suction velocity V_0. By varying the direction and velocity of the flow through the permeable surfaces, different boundary layer profiles can be obtained. Moderate levels of suction gives an asymptotic suction boundary layer (I), while a high suction velocity can result in an inviscid slip-condition (II). Blowing can also be applied through the full length or only partly (III). Depending on the chosen flow through the surfaces the initial condition of the wake and consequently the shape of the wake profile (IV) may be varied.

Figure 3.3 shows the assembly of the main body, which starts with a 300 mm long leading edge (1), followed by a 2 m long flat plate (2–4) and ending with a trailing edge (5, 6).

Leading edge. The leading edge has been milled out from a solid block of aluminium and is symmetric in the xz-plane. The symmetric profile is described by a modified super ellipse,

$$\left[\frac{a-x}{a}\right]^{m(x)} + \left[\frac{y}{b}\right]^{n} = 1 \ , \ 0 < x < a \ ,$$

where $m(x) = 2 + (x/a)^2$ and $n = 2$, see Saric *et al.* (2002). The aspect ratio, given by the quotient between the semi-major axis a and the semi-minor axis b, is 12.5. The advantage with a modified super ellipse versus an ordinary super ellipse is the continuous derivative of the curvature at the junction between the leading edge and the following flat plate.

Flat plate. The flat plate is a sandwich construction with identical top and bottom sections (2) and (3). These are decoupled from each other by a separating aluminium sheet (4). In between the separating sheet (4) and the

permeable plates (3) there are two frames consisting of 33 T-profiles directed in the spanwise direction with a spacing of 60 mm in the streamwise direction. The T-profiles are clamped in between two solid aluminium bars along the streamwise direction. Between every T-profile two 10 mm holes are drilled through the bars and where pipes and tubing are connected for withdrawal and/or injection of air. In the case of excess pressure, i.e. injection, there is nothing holding the permeable plates in position, therefore these plates are point-wise glued to the frame.

Trailing edge. The three last sections of the T-profile arrays are exchangable in order to allow for different control devices such as, an internal chamber (5) for base-bleed through a slotted plate (6), air-jets perpendicular to the main stream or simply different types of splitter plates.

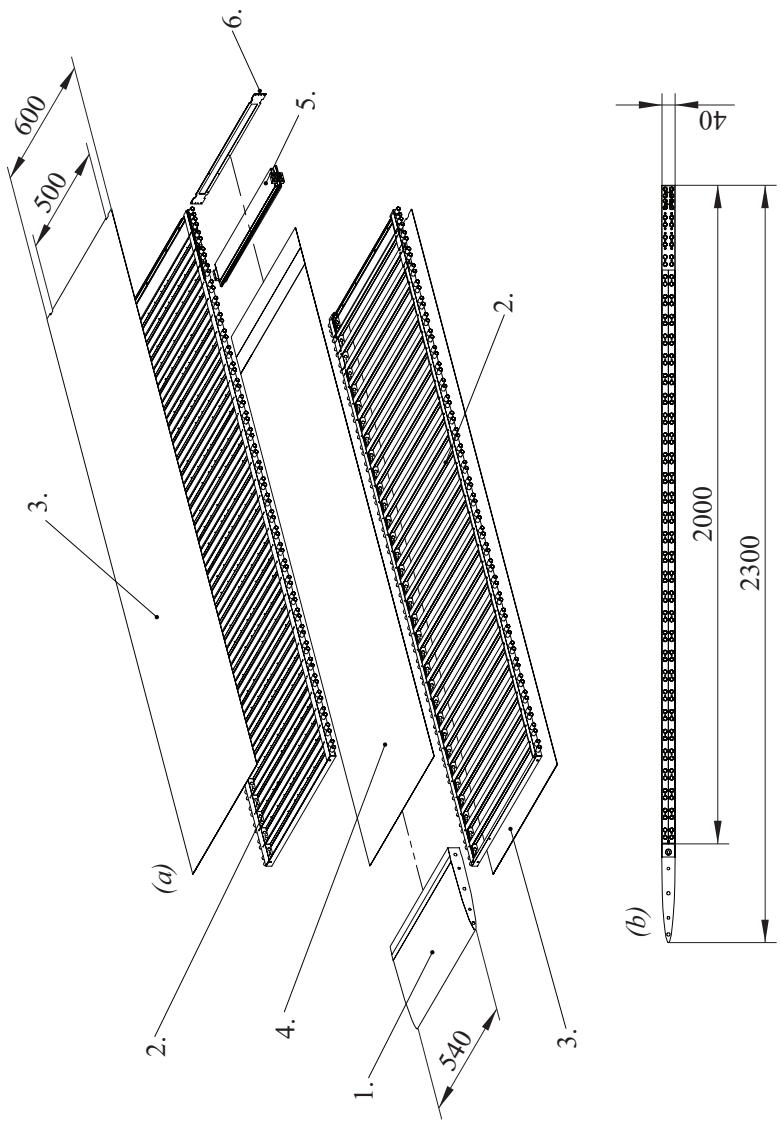

FIGURE 3.3. The main body showing the sandwich construction in *(a)* and the side view in *(b)*. All dimensions are in [mm]. 1. Leading edge, 2. Supporting frame, 3. Permeable plate, 4. Separating sheet, 5. Rear chamber and 6. Slotted end plate.

3.3.2. *Permeable plate*

Boundary layer control and drag reduction by suction through permeable sheets have been studied over several decades, mainly with applications within the aeronautical field. This extensive research has led to many investigations about permeable materials, which are suitable for boundary layer control.

Studies on the asymptotic suction boundary layer as well as the flow past a circular porous cylinder have been carried out at the department of Mechanics, KTH, see Fransson & Alfredsson (2003); Yoshioka *et al.* (2004) and Fransson *et al.* (2004), respectively. In those experiments, a sintered plastic material with a maze-like structure were used. However, experiences from the setups have shown that such a material is not suitable for extensive particle image velocimetry measurements, since the smoke that is used as seeding clogs the pores. Furthermore, such material has problems with ageing, which results in undesirable cracks and changes of the material properties and must typically be replaced regularly.

For the new setup, a material without the above drawbacks was preferable, which resulted in the choice of laser drilled titanium sheets. This material has several advantages, it is stiff, it can stand strong detergent used for cleaning, it is resistant to corrosion and it has a smooth surface after the perforation process. The discrete holes of the perforation makes the inspection of the cleanness easy simply by placing a light source behind the sheet. Similar materials such as aluminium and stainless steel were also considered, however, the former is difficult to perforate and the latter has problem with debris in the perforation process, which results in a rugged surface.

There are two main types of permeable materials, granular and fibrous materials with a labyrinth-like structure and materials perforated straight through. A major difference between these two types of materials is the relation between the flow velocity and the pressure drop over the material. The flow velocity through a labyrinth-like material increases linearly with the pressure difference, following Darcy's law, which reads

$$V = \frac{\kappa}{\mu}\frac{\Delta p}{t} \ , \tag{3.6}$$

where V is the flow velocity through the material of thickness t. Δp is the pressure difference across the material and μ and κ is the dynamic viscosity and permeability, respectively.

However, for perforated materials the relation between V and Δp is different. The velocity, through such material, may be approximated by the flow through individual pipes. A theoretical analysis was carried out in Goldstein (1938), yielding narrow pipes, which may be applied on perforated materials. Provided that $t/(r \cdot Re_{2r}) \ll 1$, where r and Re_{2r} correspond to the radius of the holes and the Reynolds number based on the hole diameter and the mean

velocity through a single hole, respectively, the relation reads

$$V = \left(\frac{2\Delta p}{\rho\{\beta + 32t/(r \cdot Re_{2r})\}} \right)^{\alpha} . \tag{3.7}$$

Here, $\alpha = 1/2$ and $\beta = 2.41$. This theoretical relation has been verified experimentally by Poll, Danks & Humphreys (1992).

The titanium sheets used in the present study are denoted 2TA1 and have a thickness of $t = 0.9$ mm. The hole diameter is $2r = 60$ μm in average and the distance from centre to centre is 0.75 mm which gives a distance to diameter ratio of 12.5. The row to row distance was also chosen to be 0.75 mm and each row in the streamwise direction is shifted. Figure 3.4 shows pictures of the holes on both sides of the sheets. Due to the focus of the laser beam during drilling, the holes have a taper angle of approximately 3 degrees. This makes the hole larger on the drilling side compared to the back, which has the desired diameter of 60 μm.

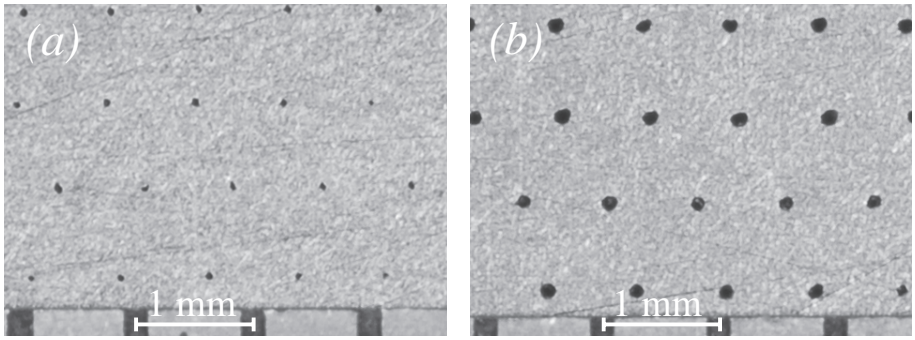

FIGURE 3.4. Images of the laser drilled titanium sheet. (a) the smaller hole diameter on the outlet side of the laser beam. (b) the larger hole diameter on the inlet side. At the bottom of the images a reference ruler is shown.

Measurements to determine the permeability of the material were also performed. Figure 3.5 shows the setup. A sample of the titanium sheet was clamped between two pipes with an inner diameter of 5 cm (a). One end was connected to a vacuum cleaner (b) and the other end to a flowmeter (c). The flow velocity was varied by changing the voltage (d) supplied to the vacuum cleaner. By measuring the pressure drop over the sample (e) for different flow velocities the permeability could be determined. A barometer (f) and a thermometer (g) were used to calculate the air density. The result of the permeability measurement is shown in figure 3.6(a) where ($\circ$) and ($\square$) represent suction and blowing, respectively. For the present perforated sheet with a typical cross flow velocity of 3 cm s^{-1} we get $t/(r \cdot Re_{2r}) > 1$ and, hence,

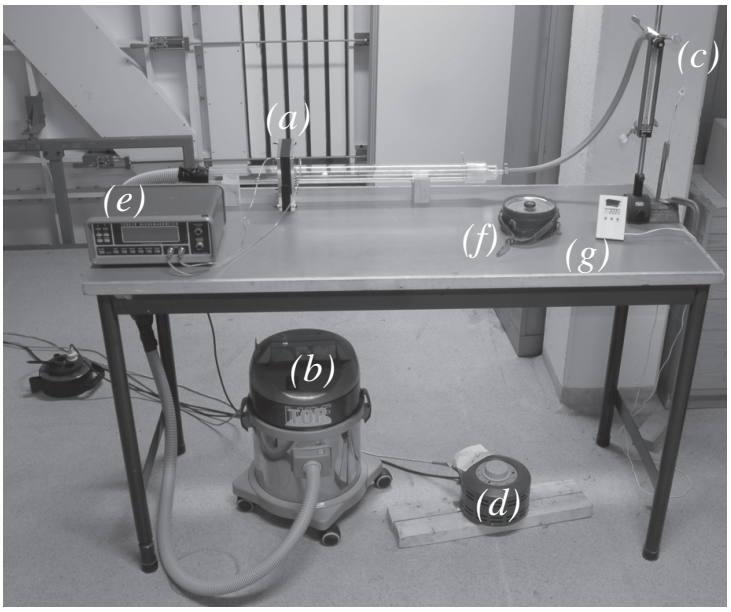

FIGURE 3.5. Setup of permeability measurements. (a) sample mount, (b) vacuum cleaner, (c) flowmeter, (d) transformer, (e) difference pressure gauge, (f) barometer and (g) thermometer.

relation (3.7) does not hold. However, the constant β and the exponent α in relation (3.7) may be determined through curve fitting to the data in a least square sense. We obtain $\beta = 42.0$ and 38.9 and $\alpha = 6/7$ and $9/11$ for the suction and the blowing case, respectively, which are shown with solid and dashed lines in figure 3.6(a). The difference is attributed to the different inlet conditions (see figure 3.4). During the laser drilling process, the pressure drop over the sheet for a chosen flow velocity of 5 cm s^{-1} was monitored in order to secure the quality of the perforation. The drilling was conducted in the spanwise direction and the pressure drop was measured at the end of each row and in figure 3.6($b - c$) the pressure drop along the sheets is shown.

The streamwise distance between the T-profiles extending in the spanwise direction has carefully been chosen. There must be enough space for tubing and at the same time the titanium sheets have to withstand the imposed pressure difference across them. A study in the commercially available multihysics and finite element solver program Comsol® was performed in order to ensure that neither bulging nor curving of the sheet will occur when blowing and/or suction are applied. To compensate for the porosity of the material, the elasticity module was reduced based on the diameter of the holes. This gives an

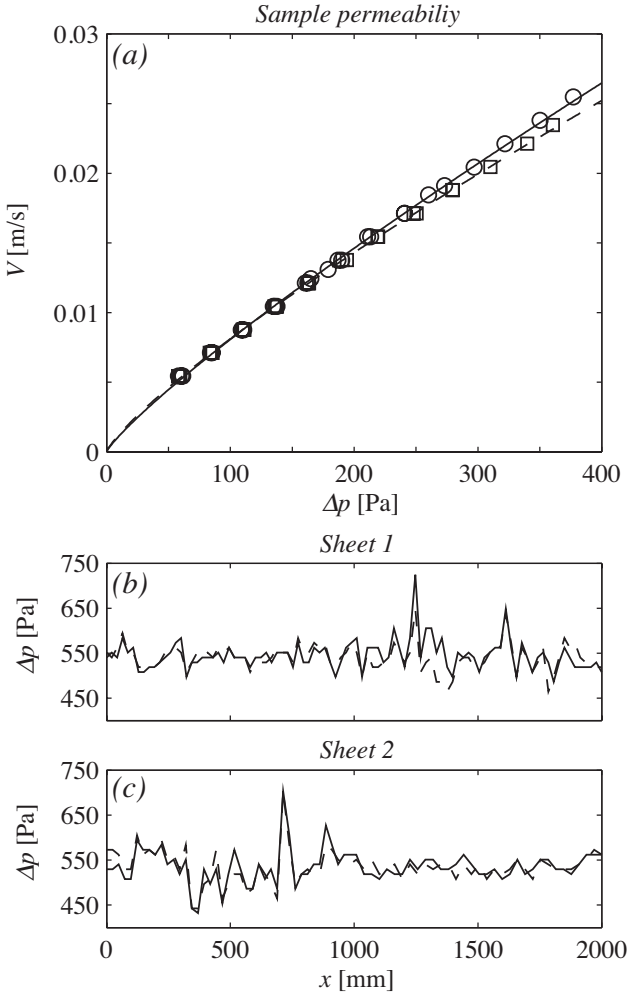

FIGURE 3.6. (a) permeability measurement on the sample. ($\circ$) suction and ($\square$) blowing configuration, with least square fits with the relation (3.7) in (—) and ($--$), respectively. ($b-c$) pressure drop along the sheets in the streamwise direction at a cross flow velocity of 5 cm s^{-1}. (—) and ($--$) represents the left and right side of the sheets, respectively.

elasticity module of 102 GPa instead of 106 GPa, which was supplied by the manufacturer.

The average of the pressure drop measured during the manufacturing was 535 Pa. This was used as a load in the displacement calculations using Comsol®

with the argument that the contemplated velocity will be less than 3 cm s^{-1}. Figure 3.7 shows that the maximum displacement is less than 50 μm for the blowing as well as the suction case. This is considered to be an acceptable displacement considering both the flatness of the material and the boundary layer thickness. The suction case in figure 3.7 shows, regularly, regions extend-

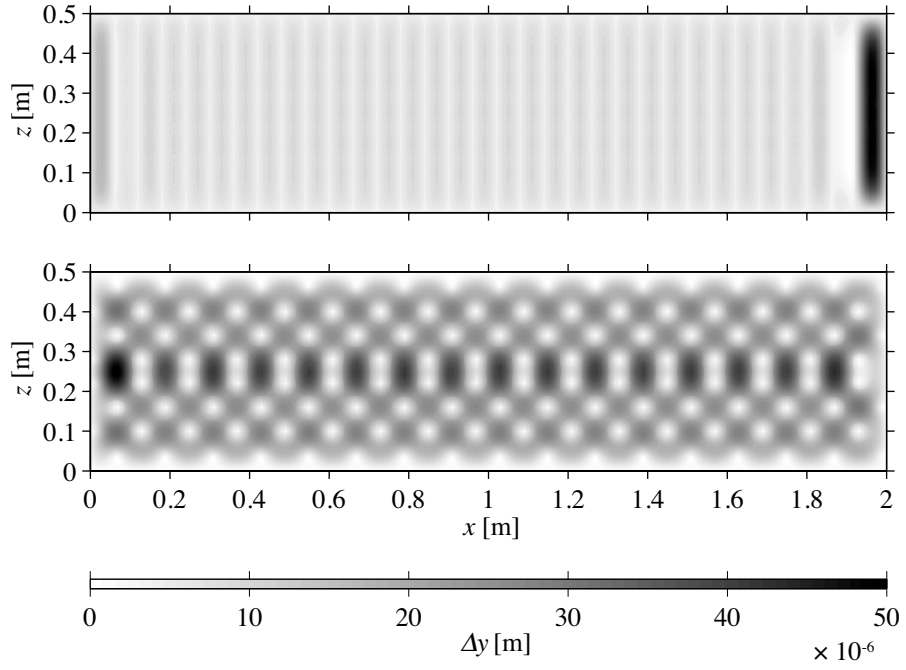

FIGURE 3.7. A finite element computation of the displacement in the y-direction due to suction *(upper)*, with negative displacement and blowing *(lower)* with positive displacement.

ing in the spanwise direction where there is no displacement (white regions). These regions correspond to the location of the spanwise pointing T-profiles. In contrary, the blowing case shows, locally, regions of no displacement (i.e. white regions), which correspond to the point-wise glued elements holding the sheet in place (see section 3.3, *Flat plate*).

CHAPTER 4

Vortex detection program

A search of the literature gives many different definitions of a vortex, see e.g. Jeong & Hussain (1995). In order to develop a vortex detection program one has to come up with some criteria that are characteristic for a vortex. A major drawback with experiments is that most available data is two-dimensional, i.e. the velocity field is only known in one plane. This seriously limits the definition of a vortex, which leads to a less restrictive definition compared to a vortex defined in a three-dimensional velocity field.

This chapter will therefore start with a brief summary of different vortex definitions and discuss their pro and cons in order to shed some light on the limitations of the present vortex detection algorithm.

4.1. Definitions of a vortex

How to define a vortex is an issue that have been discussed for several decades due to the complexity of turbulent flow fields. Numerical modelling has made the dynamics of flow fields more accessible for studies and different methods can more easily be compared. Jeong & Hussain (1995) summarise and discuss the most frequently used definitions of a vortex. Roughly speaking, the different definitions can be divided into intuitive and analytical approaches. The former is based on local properties of the flow such as local pressure minima p, the paths of the streamlines

$$\frac{\mathrm{d}x}{u} = \frac{\mathrm{d}y}{v} = \frac{\mathrm{d}z}{w} \ , \tag{4.1}$$

and the magnitude of vorticity

$$|\omega| \equiv |\nabla \times \mathbf{u}| \ . \tag{4.2}$$

The latter is based on properties of the velocity gradient tensor $\nabla \mathbf{u}$.

Jeong & Hussain (1995) states two requirements for a vortex core as a preliminary check for an evalutation of the different methods. Firstly, a vortex core must have a net vorticity and hence, net circulation, and secondly, the geometry of the identified vortex should be invariant in a Galilean transformation. A short summary of the review follows.

4.1.1. *Intuitive approaches*

Pressure minima. When the centrifugal force is balanced by the pressure force, a local pressure minimum is located at the axis for the swirling motion. This is shown to be true only in a steady inviscid planar flow, why this is not a valid condition in general.

Closed or spiral pathlines or streamlines. Closed or spiral pathlines or streamlines have been proposed to be used to identify the swirling motion of a vortex. The lifetime of a vortex might however not be long enough for a particle to complete a full revolution that is required for the closed pathline, which means that vortices will occur without being detected. Furthermore, neither closed or spiral pathlines or streamlines are invariant with respect to Galilean tranformation, so only vortices that are translated within a certain range of velocity will be detected.

Vorticity magnitude. Defining a vortex as a region where its vorticity magnitude is higher than some threshold has also been suggested as a method. This method turns out to be quite arbitrary since, firstly, it dependents on the threshold and secondly, as soon as the background shear is within the same magnitude a distinction between the shear and the vortex may be unfeasible.

4.1.2. *Analytical approaches*

Considering the more analytical approaches, the drawbacks are fewer, although there are still cases where those approaches are unsuitable. Two older methods are presented and compared to the most accepted and used method, namely the $\lambda_2 - method$.

Complex eigenvalues of velocity gradient tensor, the Δ-method. This approach considers the eigenvalues, λ, of the velocity gradient tensor $\nabla \mathbf{u}$, which satisfies the characteristic equation

$$\lambda^3 - P\lambda^2 + Q\lambda - R = 0 \ . \tag{4.3}$$

Considering an incompressible flow ($u_{i,i} = 0$) the three invariants of $\nabla \mathbf{u}$ above become

$$P \equiv u_{i,i} = 0 \ , \tag{4.4}$$

$$Q \equiv \frac{1}{2}(u_{i,i}^2 - u_{i,j}u_{j,i}) = -\frac{1}{2}u_{i,j}u_{j,i} \tag{4.5}$$

and

$$R = \det(u_{i,j}) \ . \tag{4.6}$$

Chong *et al.* (1990) showed that complex eigenvalues imply that the local streamline pattern is closed or spiral in a reference frame moving with the

point, i.e. when the discriminant

$$\Delta = \left(\frac{1}{3}Q\right)^3 + \left(\frac{1}{2}R\right)^2 \tag{4.7}$$

is positive. Although this method is Galilean invariant, it shows when trying the method on some special cases, such as mixing layers and swirling jets, that Δ is slightly positive even outside vortex cores resulting in that the boundary of the vortices becomes noisy and the size of the vortices are overestimated.

The second invariant of the velocity gradient tensor, the Q-method. It has been suggested to define vortices as regions where $Q > 0$, with the additional condition that the pressure is lower than the ambient value. One may rewrite Q in terms of the symmetric and the antisymmetric parts of $\nabla\mathbf{u}$, i.e. the strain rate tensor and the rotational tensor, respectively. Hence, Q represents the local balance between shear strain rate and vorticity magnitude. According to (4.7) the Q-method is more restrictive than the Δ-method, however, the most appropriate method is not obvious *a priori*.

λ_2-method. The frequently used λ_2-method (Jeong & Hussain 1995) comes from inspection of the acceleration gradient

$$a_{i,j} = -\frac{1}{\rho}p_{,ij} + \nu u_{i,jkk} \ , \tag{4.8}$$

which is derived by taking the gradient of Navier-Stokes equations. Pressure minimum has been used as a starting point without being used as a requirement. The left hand side of (4.8) can be divded into a symmetric and an antisymmetric part where the antisymmetric part is the vorticity transport equation. Leaving out the unsteady irrotational straining and viscous effects in the symmetric part one gets

$$-\frac{1}{\rho}p_{,ij} = S_{ik}S_{kj} + \Omega_{ik}\Omega_{kj} = \mathbf{S}^2 + \mathbf{\Omega}^2 \ , \tag{4.9}$$

where $S_{ij} = (u_{i,j} + u_{j,i})/2$ and $\Omega_{ij} = (u_{i,j} - u_{j,i})/2$ are the symmetric and the antisymmetric parts of $\nabla\mathbf{u}$, and defined as the strain rate tensor and the rotational tensor, respectively. Local pressure minima existing only due to vortical motion, are then present if two of the eigenvalues of $\mathbf{S}^2 + \mathbf{\Omega}^2$ are negative. Since $\mathbf{S}^2 + \mathbf{\Omega}^2$ is symmetric its eigenvalues λ_1, λ_2 and λ_3 are real, which requires that $\lambda_2 < 0$ within the vortex core if $\lambda_1 \geq \lambda_2 \geq \lambda_3$.

This definition is then compared, by Jeong & Hussain (1995), with the two methods above for various cases and it is found to be the most general method to identify vortices. It is referred to as the λ_2-method and has been widely accepted and is even implemented in many numerical codes. The method, however, requires that the Hessian of the pressure is known, i.e. all three

components of the velocity gradient tensor, which are never available in experiments. For this reason the Δ- as well as the Q-method are the most widely used on two-dimensional experimental data.

4.1.3. *Two-dimentional velocity fields*

In order to detect vortices that are embedded in two-dimensional velocity fields, commonly acquired through PIV-measurements, Adrian *et al.* (2000) suggested that decomposition of the velocity field by low-pass filtering is an adequate way to visualise small-scale vortices. In their study, a Gaussian filter was used for the decomposition and the vortices were then detected by using the approach suggested by Chong *et al.* (1990), i.e. identifying closed or spiral streamline patterns by looking at the complex eigenvalues of the high-pass filtered two-dimensional velocity gradient tensor,

$$\nabla \mathbf{u}''_{2D} = \begin{bmatrix} \frac{\partial u''}{\partial x} & \frac{\partial u''}{\partial y} \\ \frac{\partial v''}{\partial x} & \frac{\partial v''}{\partial y} \end{bmatrix} . \tag{4.10}$$

Regions where the imaginary eigenvalues are positive and greater than a threshold are then defined as a vortex. Agrawal & Prasad (2002) also used a Gaussian filter to perform the decomposition suggsted by Adrian *et al.* (2000), while vortices were identified by looking at the neighbouring vectors of each point. If the angular orientation of the surrounding vectors experienced a monotonically angular variation from 0 to 2π the point was considered to be a vortex centre. The same decomposition will be used here, while the Δ-method according to Chong *et al.* (1990) will be used for the vortex identification.

4.2. Velocity field filtering

4.2.1. *Decomposition*

A turbulent flow field consists of a spectrum of different scales, from the largest geometrically allowed down to the smallest viscous scale, namely the Kolmogorov scale. To reveal the small-scale structures that are embedded in the measured turbulent flow field, the latter is decomposed into a low-pass filtered velocity field and a high-pass velocity field, corresponding to the spatially large and small scale structures, respectively. If these velocity fields are added together, one recovers the fully measured flow field, see figure 4.1. The decomposition is performed in the same manner as in e.g. Agrawal & Prasad (2002), i.e. convolving a low-pass filter on the full velocity field $\mathbf{u}$, and thereby get a velocity field $\bar{\mathbf{u}}$ that contains the larger scales of the full velocity field. To get the small scale velocity field $\mathbf{u}''$, the large-scale field is then subtracted from the full velocity field as

$$\mathbf{u}'' = \mathbf{u} - \bar{\mathbf{u}} . \tag{4.11}$$

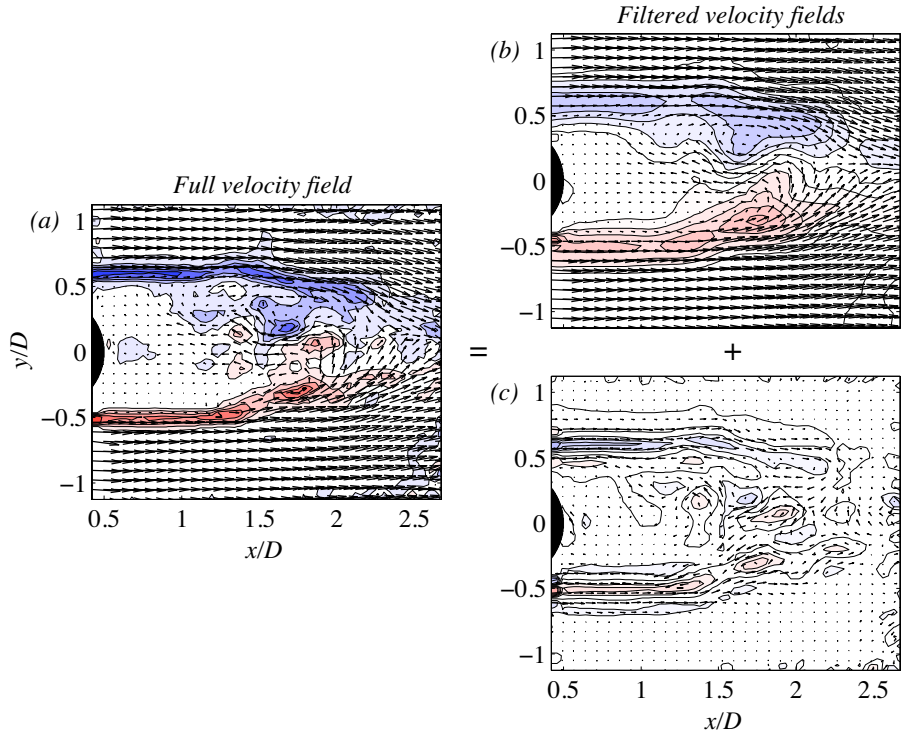

FIGURE 4.1. (*a*) An instantaneous velocity field behind a porous cylinder with continuous suction through the surface of 2.6% of the oncoming velocity. (*b*) and (*c*) show the low- and high-pass filtered velocity fields, respectively.

4.2.2. *Gaussian filter*

The filter used for the decomposition is a Gaussian filter that averages the single point (m, n) with the surrounding points. This will give a smeared out velocity field which will emphasise and keep the large scale structures according to

$$\bar{\mathbf{u}}(m,n) = \frac{\sum_{j=-k}^{k}\sum_{i=-k}^{k} g(i,j)\mathbf{u}(m-i,n-j)}{\sum_{j=-k}^{k}\sum_{i=-k}^{k} g(i,j)} \,, \tag{4.12}$$

where (i, j) is the indices in x and y, respectively. Here, k is defined as the radius of the filter and since a discrete velocity field is considered, it has a quadratic shape, with each point (m, n) being affected by a surrounding squared region. The Gaussian kernel (g) is defined as

$$g(i,j) = \exp\left[-\frac{(i\Delta x)^2 + (j\Delta y)^2}{2\sigma^2}\right] , \tag{4.13}$$

where Δx and Δy are the grid spacing and σ is the padding of the filter. The parameters k and σ can then be chosen by introducing an anisotropy measure d^2_{rms}, which is defined as the absolute value of the normalised difference between the velocity variance components,

$$d^2_{rms} = \left|\frac{u^2_{rms} - v^2_{rms}}{U^2_\infty}\right| . \tag{4.14}$$

In figure 4.2(a) the maximum value of the anisotropy is shown as contour lines for varying k and σ for the velocity field downstream of a cylinder. A consistent requirement for the choice of filter would be to allow a certain amount of anisotropy in the final high-pass filtered velocity field. Typically one here chooses a $\max\{d^2_{rms}\} \leq 0.01$, which is in the order of one magnitude lower than for the unfiltered case. Figure 4.2(b) shows the shape of the Gaussian filter for $k = 5$ and $\sigma = 5$. The filter is normalised, i.e. the total weight is equal to 1, and the small difference in weight between the minima and maxima implies that this filter will smear out smaller scales, while larger scales will remain, which is the pupose with low-pass filtering.

4.2.3. *Statistics*

In each instantaneous PIV-image, contours where the imaginary part of the complex eigenvalues, λ_{ci}, corresponds to a threshold value is defined as a vortex. Each contour is then examined in order to determine relevant properties such as location, size, circulation and swirl strength of the vortex. This is executed in the following manner. The centre of the vortex is identified by finding the x- and y-coordinates of the maximum imaginary eigenvalue, $\lambda_{ci,max}$, within the contour. This eigenvalue is also stored as a measure of the swirl strength of the vortex (see e.g. Zhou *et al.* 1999). The size of the vortex is then determined by first calculating the area inside the threshold contour level. An equivalent radius to a corresponding circle (C) with its origin at $\lambda_{ci,max}$ is then used as a starting radius for calculating the circulation, γ, through direct integration along C's perimeter $\mathbf{l}$ according to

$$\gamma = \oint_C \mathbf{u}'' \cdot d\mathbf{l} . \tag{4.15}$$

This process is repeated while stepping outwards from the vortex centre until the maximum value of the circulation is reached, which then is stored. The corresponding radius is also stored as the vortex size. The two different vortex size measures are shown in figure 4.3(b). Note, that the background velocity

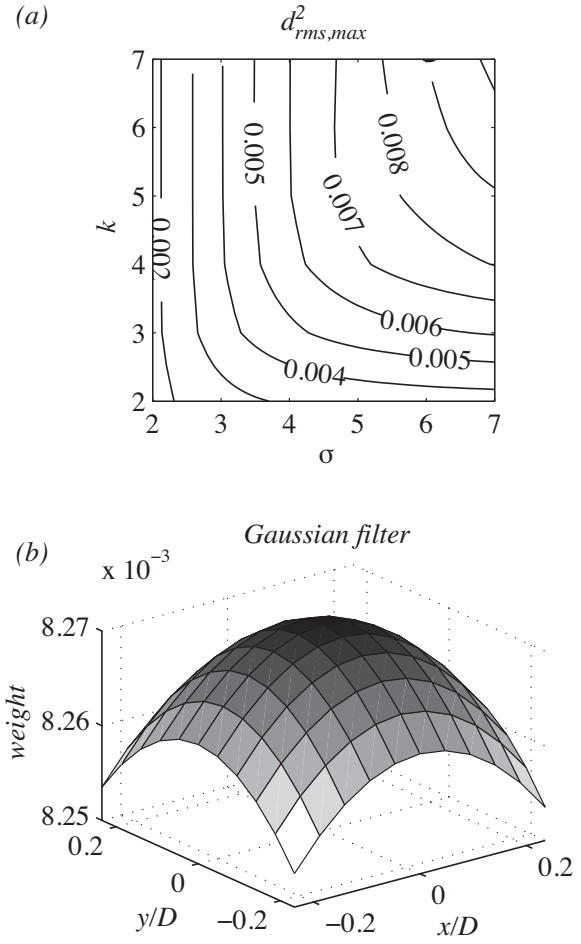

FIGURE 4.2. The maxmimum values of the anisotropy measure $d^2_{rms,max}$ for different values of k and σ when filtering the flow field behind a circular cylinder with the diameter $D = 50$ mm. *(b)* The corresponding shape of the normalised Gaussian filter for $k = 5$ and $\sigma = 5$.

vector field is the full velocity field in where the vortices are not necessarily shown.

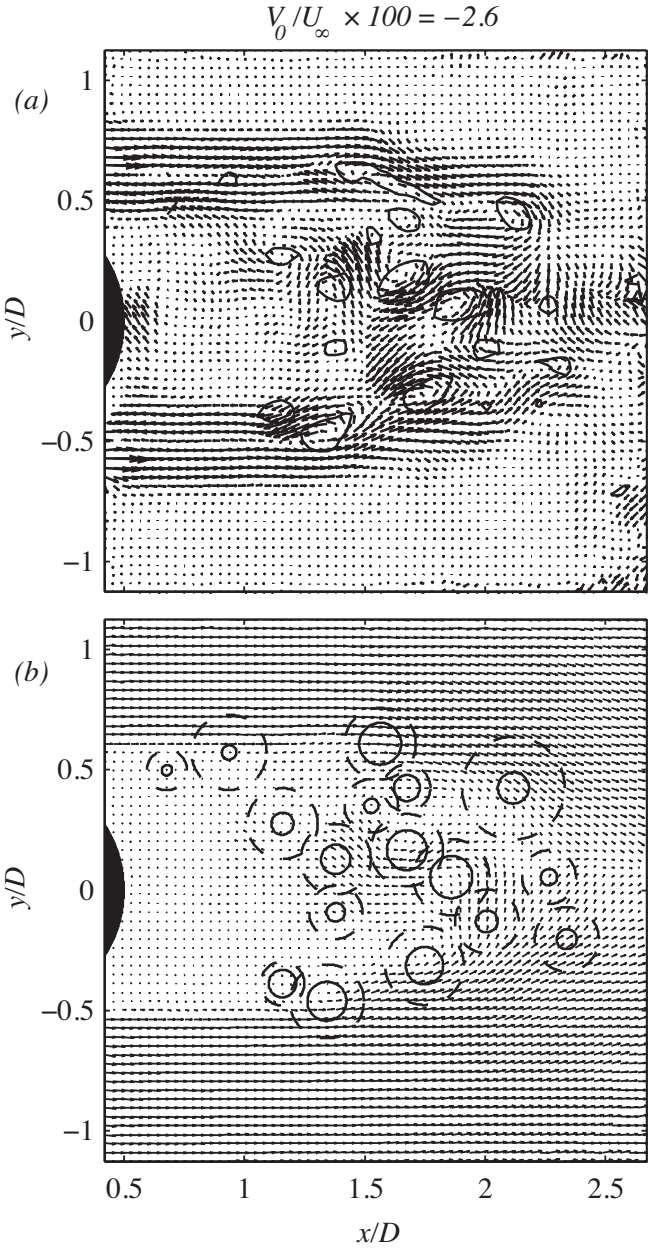

FIGURE 4.3. Instantaneous velocity field of the flow behind a circular cylinder subjected to suction. (*a*) shows the small scale velocity field where contour lines are regions of $\lambda_{ci} > 15$ and (*b*) the unfiltered velocity field where (—) corresponds to the equivalent radius of the threshold contour and (−−) corresponds to the radius of the vortex, based on the definition of maximum circulation.

CHAPTER 5

Summary

In this thesis a new experimental setup for studies on wake flow instabilities and control is introduced. A main body consisting of a flat plate, with an elliptic leading edge and a blunt trailing edge, was designed as a sandwich construction with an hollow interior and has been manufactured. Permeable surfaces on both sides give the unique possibility to perform boundary layer suction or blowing along the plate and thus, mastering the inlet profile of the wake. The dual layer design enables an asymmetric wake to be created, by independently adjusting the pressure difference across the surfaces on the two sides. Furthermore, the plate has separate compartments, which makes local manipulation of the boundary layer possible.

An exchangeable trailing edge of the plate adds the possibility to implement various types of active control devices, such as feed-back controlled jets or base-bleed. Passive control devises such as splitter plates and other obstacles for manipulation of the periodic separation is also easily mounted.

The new test section is designed for the use of modern measurement techniques such as high-speed stereoscopic PIV, which generates a high amount of data about the flow field. To effectively handle all the acquired data, a Matlab® program that automatically filters a two-dimensional velocity field and identifies small-scale vortices has been developed. The program stores information about vortex location, size, strength and circulation, which makes statistical analyses for different flow conditions a straightforward process.

Combining the new experimental setup with the developed tool for velocity field analyses, the understanding of the wake flow behaviour for different inlet conditions as well as control methods, will be enhanced. The aim is that this will contribute to the efforts in finding new means to reduce drag and oscillating structural forces on bluff bodies in different technical applications.

CHAPTER 6

Papers and authors contributions

Paper 1

Vortex analysis in the wake of a porous cylinder subject to suction or blowing.
B. E. G. Fallenius (BF) & J. H. M. Fransson (JF).

This work is based on experiments on a porous cylinder subjected to suction or blowing, performed by JF. A computer program that was initiated by JF is used to identify small-scale vortices. BF debugged and restructured the program and ran it on the experimental data. The results have been produced by BF and the article has been written jointly by the authors. Parts of this work have been presented at the European Fluid Mechanics Conference 2008, Manchester, Great Britain, and at the XXII International Congress of Theoretical and Applied Mechanics 2008, Adelaide, Australia.

Paper 2

On the vortex generation behind a passive V-shaped mixer in a pipe flow.
B. E. G. Fallenius (BF) & J. H. M. Fransson (JF).

The experiments were carried out by BF and JF in collaboration with the Marcus Wallenberg Laboratory. BF has extracted the results from the measurements and the paper has been written jointly by the authors. Parts of this work are published in AIAA Paper 2008-3057, and have been presented at the 14th AIAA/CEAS Aeroacoustics Conference 2008, Vancouver, British Columbia, Canada.

Acknowledgements

First of all I would like to express my gratitude to my supervisor Docent Jens Fransson for giving me the opportunity to perform the graduate studies as well as the professional guidance you are giving me. Also, I would like to thank my co-advisor Prof. Henrik Alfredsson for the nice and inspiring working environment in the fluid physics laboratory.

I also would like to thank Docent Fredrik Lundell, Dr. Nils Tillmark, Prof. Alessandro Talamelli and Prof. Laszlo Fuchs for encouraging advices, comments on my work and for introducing interesting references to me. Göran Rådberg and Joakim Karlström are greatly acknowledged for the skilful manufacturing of the new setup and for patiently making last minute changes, as well as for giving constructive suggestions of improvements in the design. Thanks also to Marcus Gällstedt and Ulf Landén for introducing me to toolmaking as well as my very first experimental setup.

Thanks to Ola, Malte and Shahab for the fun and relaxing atmosphere we have in our office, which is essential for my work.

Special thanks to Veronica, Ramis, Gabriele, Thomas, Allan and Outi for the reception and support that has continued ever since I started. Thank you also Fredrik H., Anna, Shiho, Monika, Olle, Fredrik La., Emma, Charlotte, Ulrika and Niklas for contributing to all the joy I have during the days in the lab. Linus, Niklas, Robert, Mattias, Tobias, Espen and all the other collegues and staff at OB18 have also made the days at the department of mechanics to a pleasure.

Last but not least I would also thank my family and friends outside KTH for their endless support.

The Swedish Research Council (VR) and the Göran Gustafsson Foundation is acknowledged for the financial support

References

Adrian, R. J., Christensen, K. T. & Liu, Z.-C. 2000 Analysis and interpretation of instantaneous turbulent velocity fields. *Exp. Fluids* **19**, 275–290.

Agrawal, A. & Prasad, A. 2002 Properties of vortics in the self-similar turbulent jet. *Exp. Fluids* **33**, 565–577.

Chong, M. S., Perry, A. E. & Cantwell, B. J. 1990 A general classification of three-dimensional flow fields. *Phys. Fluids* **2**, 765–777.

Fransson, J. H. M. & Alfredsson, P. H. 2003 On the disturbance growth in an asymptotic suction boundary layer. *J. Fluid. Mech.* **482**, 51–90.

Fransson, J. H. M., Konieczny, P. & Alfredsson, P. H. 2004 Flow around a porous cylinder subject to continous suction or blowing. *J. Fluids Struct.* **19**, 1031–1048.

Goldstein, S. 1938 *Modern developments in fluid dynamics, Vol.I*. Clarendon Press Oxford.

Griffith, A. A. & Meredith, B. A. 1936 The possible improvement in aircraft performance due to the use of boundary layer suction. *Tech. Rep.* 3501. Royal Aircraft Establishment.

Jeong, J. & Hussain, F. 1995 On the identification of a vortex. *J. Fluid. Mech.* **285**, 69–94.

Kármán, T. 1912 Über der Mechanismus des Wiederstandes, den ein bewegter Körper in einer Flüssigkeit erfährt. *Göttingen Nachr., Math.-Phys. Klasse* pp. 547–556.

Lindgren, B. 2002 Flow facility design and experimentsl studies of wall-bounded turbulent shear-flows. PhD thesis, Royal Institute of Technology.

Norberg, C. 1994 An experimental investigation of the flow around a circular cylinder: influence of aspect ratio. *J. Fluid. Mech.* **258**, 287–316.

Poll, D. I. A., Danks, M. & Humphreys, B. E. 1992 The aerodynamic performance of laser drilled sheets. *First European Forum on Laminar Flow Technology* pp. 274–277.

Saric, W. S., Reed, H. L. & Kerschen, E. J. 2002 Boundary-layer receptivity to freestream disturbances. *Annu. Rev. Fluid Mech.* **34**, 291–319.

Yoshioka, S., Fransson, J. H. & H., A. P. 2004 Free stream turbulence induced disturbaces in boundary layers with wall suction. *Phys. Fluids* **16**, 3530–9.

Zhou, J. Adrian, R. J., Balachandar, S. & Kendall, T. M. 1999 Mechanisms for generating coherent packets of hairpin vortices in channel flow. *J. Fluid. Mech.* **387**, 353–396.

Part II

Papers

1

Paper 1

Vortex analysis in the wake of a porous cylinder subject to suction or blowing

By Bengt E. G. Fallenius and Jens H. M. Fransson

Linné Flow Centre, KTH Mechanics, SE–100 44 Stockholm, Sweden

Wake flow effects behind a porous cylinder subject to varying levels of continuous suction or blowing have been investigated using particle image velocimetry. Due to large mean flow changes in the wake, but with opposite trends when suction and blowing are applied, the location of interesting events, such as the confluence point of the twin-vortices and the position of maximum backflow, move and consequently two different frames were used for the suction and the blowing cases. This limits the analysis to relative comparisons with the natural case, i.e. without suction or blowing applied. For moderate levels of suction and blowing (less or equal to 6.5% of the free stream velocity), suction can completely suppress the boundary layer growth and the flow becomes potential-like around the cylinder. Blowing gives the opposite effect with an increase of the wake size, which has been quantified by means of vortex formation length measures. The Reynolds number is around 4 000 implying that the wake flow is turbulent with a wide range of vortex sizes and intensities. It is shown that streamwise streaky regions with induced secondary vortices from the primary von Kármán vortices are present. In general, the secondary vortices are smaller, weaker and of opposite rotational sign compared to the primary ones. The streamwise streaky regions are reduced in their streamwise extent and move towards the shoulders of the cylinder, when suction is increased. Blowing has the opposite effect but experiences an interesting change in trend for high enough blowing levels, i.e. the smaller vortices become the strongest ones. This is suggested to be a result of the energy transfer from the primary to the secondary vortices.

1. Introduction

The phenomenon of periodic vortex shedding behind bluff bodies is of direct relevance to many practical and industrial applications, such as in telecom masts, aircraft and missile aerodynamics, civil and wind engineering, marine structures, and underwater acoustics. This periodic vortex shedding can lead to devastating structural vibrations that finally lead to material fatigue and structural failure.

The vortex shedding instability, in the wake behind bluff bodies, is a self excited oscillation that will set in even if all sources of noise are removed (see Gillies 1998), and can be shown to be attributed to the local stability property of the two-dimensional mean velocity wake profile behind a bluff body. Monkewitz (1988) identified a sequence of stability transitions by using a family of wake profiles, that resulted in $Re_C < Re_A < Re_K$, where Re_C (≈ 5), Re_A (≈ 25), and Re_K (≈ 47) are critical Reynolds numbers that mark the onset of convective, absolute, and von Kármán shedding instability, respectively. This sequence was in fully agreement with the qualitative model predictions by Chomaz *et al.* (1988) the same year. The onset of the global von Kármán shedding mode occurs via a so-called supercritical Hopf bifurcation (see e.g. Provansal *et al.* 1987). For a review on the stability properties of open flows in general the interested reader is referred to Huerre & Monkewitz (1990), and for reviews on cylinder flows in particular see e.g. Williamson (1996); Buresti (1998); Norberg (2003); Zdravkovich (1997, 2003).

The wake flow behind circular cylinders have been studied thoroughly the last century and lately also different methods to control its instability. Both passive and active control methods have successfully been applied. Here, the distinction between passive and active control methods is made based on whether the energy in the flow system is used for the control or if energy has to be added to the system in order to obtain the control. Examples of passive and active control methods are for instance, splitter plates or obstacle placements in the very near wake, and base-bleed or cylinder vibrations, respectively. Below a brief review of different control methods, that have been applied on circular cylinders, is given.

A simple passive control method is to place a thin splitter plate aligned in the streamwise direction on the centreline of the near wake (see Roshko 1955, 1961). For a specific length of the splitter plate the sinuous von Kármán mode is altered for a varicose mode that causes a pair of twin–vortices to be formed, one on each side of the plate. More recently, Grinstein *et al.* (1991) carried out numerical simulations on the effect of an interference plate in the wake of a plate and found that the base pressure coefficient could decrease by a factor of 3 depending on the length of the plate and its separation from the base.

Experiments on circular cylinders with forced rotary oscillations have shown to give a drag reduction of up to 80% at $Re = 15\ 000$ for certain ranges of frequency and amplitude of the sinusoidal rotary oscillation (see Tokumaru & Dimotakis 1991). Shiels & Leonard (2001) performed numerical simulations of this control approach where the above experimental findings were verified and showed indications that this kind of control could be even more efficient at higher Re.

Control approaches using feedback control have also been attempted. Roussopoulos (1993) carried out experiments in a wind tunnel with acoustic waves

from a loudspeaker as actuation as well as by vibrating the cylinder. In a numerical study by Park *et al.* (1994) blowing and suction through slots on the rear part of the cylinder were utilized as actuation. However, this investigation were performed at relatively low Reynolds numbers (< 300) and so far it does not exist any results on higher Re-flows.

Glezer & Amitay (2002) used synthetic jets, which provide a localized addition of momentum normal to the surface, on selected positions over the cylinder in order to delay separation in both laminar and turbulent boundary layers. They argued that this delay was caused by increased mixing within the boundary layer. In addition, the interaction between the jet and the cross flow has a profound effect both on the separated shear layer and on the wake; the magnitude of the Reynolds stresses is reduced indicating that the delay in separation is not merely the result of a transition to turbulence in the boundary layer.

Experiments with suction or blowing through the entire surface of the cylinder in order to control the vortex shedding have been considered by e.g. Pankhurst & Thwaites (1950); Hurley & Thwaites (1951); Mathelin *et al.* (2001*a*,*b*); Fransson *et al.* (2004). Pankhurst & Thwaites (1950) made combined experiments with continuous suction through the surface and a flap in form of a short splitter plate at different angles. They showed through surface pressure and wake velocity measurements that with the flap directed in the streamwise direction and for sufficient suction[1] ($C_q\sqrt{R} \gtrsim 10$) the separation is entirely prevented and a remarkable close approximation to the potential flow solution is achieved. Furthermore, Hurley & Thwaites (1951) performed boundary layer measurements on the same porous cylinder and found in general good agreement with laminar boundary layer theory. However, no time resolved measurements to determine the vortex shedding frequency were reported.

The von Kármán frequency is Reynolds number dependent, whilst the dimensionless frequency known as the Strouhal number is constant (≈ 0.2) in the range $10^2 \lesssim Re \lesssim 10^5$. Mathelin *et al.* (2001*a*,*b*) considered the case of continuous blowing through the entire cylinder surface (see Mathelin *et al.* 2001*a*, for a detailed description of the experimental setup). Among the effects observed are a wider wake and a decrease of the Strouhal number with increasing blowing. They report an analytical relation of an equivalent Reynolds number of the canonical case, which produces the same flow characteristics in terms of vortex shedding instability as the case with blowing versus the blowing rate. The result is that the Strouhal number decreases with blowing, which was experimentally verified by Fransson *et al.* (2004), who also considered the effect of continuous suction, which turns out to have the contrary effect on the Strouhal number. In Fransson *et al.* (2004) the changes in the flow due to blowing or

[1]Here C_q is a suction coefficient defined as the suction velocity per unit area divided by the free stream velocity.

suction were analyzed in terms of mean and fluctuating velocity profiles in the wake through hot-wire anemometry, pressure distributions on the cylinder, and drag and vortex shedding measurements. Furthermore, smoke visualizations of the flow field in the near wake of the cylinder for different blowing or suction rates were reported. Image averaging enabled the retrieval of quantitative information, such as the vortex formation length, which showed that the vortex formation length is decreased by 75% and increased by 150% for 5% of suction and blowing of the free stream velocity, respectively.

In this study the effect of continuous suction or blowing through the entire surface of a porous cylinder has been investigated with the emphasis on vortex statistics, which complements above cited works on porous cylinders. Vortex analysis, apart from the Kármán vortices, can only be performed with an instantaneous flow field measurement technique and here a two-dimensional Particle Image Velocimetry (PIV) system has been used. As stated above it has previously been shown that suction and blowing of continuous type have a large impact on the mean velocity field and consequently the drag force, but has not given any information about the effect on the individual vortices and small scale structures. The Reynolds number is around 4 000, which is in the subcritical regime (cf. Roshko 1961), implying laminar boundary layers around the cylinder with a purely laminar separation and a turbulent wake with a wide range of both vortex sizes and strengths.

The present paper has the following outline, in section 2 the experimental setup and measurement technique is reported, which is followed by a summary of the vortex detection algorithm (section 3) that has been adopted here. Next, the results are presented in section 4, where the suction and the blowing results are presented separately from each other. The paper ends with a summary and conclusion section (5).

2. Experimental setup and measurement technique

2.1. *Wind tunnel*

The experiments were performed in the BL wind tunnel[2] at KTH Mechanics, Stockholm. The cross sectional area of the test section is 0.5×0.75 m^2, and it is 4.2 m long with a maximum speed of 48 ms^{-1}. The flow quality in this tunnel is considered good with a turbulence intensity (of all three components) of less than 0.04% of the free stream velocity. The tunnel has a heat exchanger after the fan, prior to the first corner. At 25 ms^{-1} the temperature variation over the cross section area is less than ± 0.07 °C and the variation over a time period of 4 hours is less than ± 0.03 °C. At this speed the total pressure variation is less than ± 0.1%. The tunnel was successfully designed with expanding corners (larger outlet than inlet cross section area) in order to reduce the total wind

[2]Boundary Layer or Björn Lindgren named after its designer.

tunnel circuit length with only a negligible increase of the total pressure loss. The interested reader is referred to Lindgren (2002) for further details.

2.2. *Cylinder*

The same porous cylinder as was used by Fransson *et al.* (2004) for flow visualisation was used in the present investigation. The cylinder consists of a cross profile made of brass as an inner skeleton. A sintered plastic material shaped to a cylinder is then slided over the brass profile and sealed, creating four isolated chambers through where different amount of blowing or suction may be applied. The end parts were made of brass pieces and act as plugs on each side of the cylinder. These were equipped with four inlets for tube connections that were confluenced before connected to a flow meter (rotameter type). Tubing was also used to lead air to or from a low or high pressure vessel, respectively, depending on whether suction or blowing was desired. The pressure source was either a regular vacuum cleaner, for suction, or a compressor, for blowing.

In figure 1 a schematic of the experimental setup is shown with relevant measures. The cylinder was mounted vertically in the test section and has a diameter of $D = 50$ mm and a porous length of 600 mm. The porous material is a sintered plastic material with an average pore size of 16 μm, and the thickness (t) is 2.5 mm. Previous surface roughness measurements on a similar but flat porous plate (see Fransson & Alfredsson 2003) showed a deviation of ± 1 μm

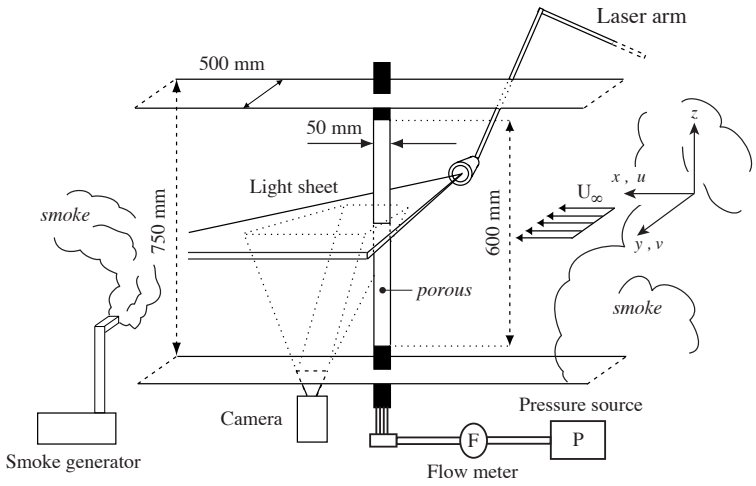

FIGURE 1. Schematic of the experimental setup. Flow is from right to left.

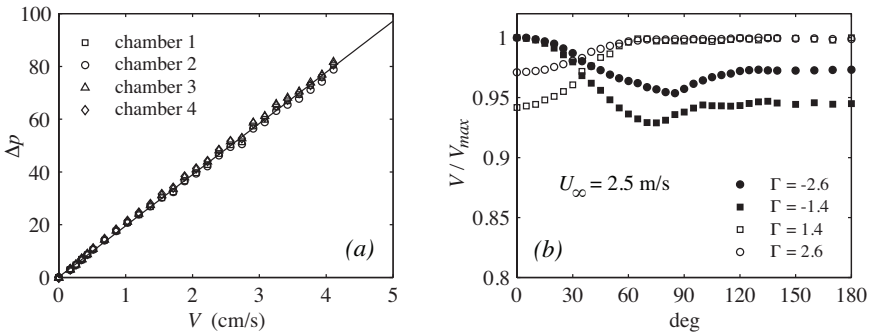

FIGURE 2. (*a*) Permeability determination of the porous material (repeated for all chambers). Solid line is the best fit to all data. (*b*) Suction/blowing distribution due to the static pressure variation around the circumference of the cylinder.

from the mean surface, which for the present case can be considered to be hydraulically smooth. The cylinder is made from a flat plate which is bent to form a circular cylinder. This means that there is a joint in the axial direction along the full length of the cylinder, and this gives rise to a small asymmetry with a 0.5 mm larger diameter in average when measured over the joint. The joint is therefore positioned at 180°, i.e. behind the cylinder in the streamwise direction, in order to avoid any flow asymmetry.

To determine the permeability of the material the pressure difference (Δp) over the cylinder wall and the flow rate $Q = V \times S$, where V and S are the velocity through the porous material and the surface area, respectively, were measured, when suction was applied. Through Darcy's law the permeability (κ) is then determined to be $\kappa = \mu t V/\Delta p = 2.31 \times 10^{-7}$ m^2, by best line fitting to the data (μ is the dynamic viscosity), see figure 2(*a*). Furthermore, a non-uniform suction/blowing rate is expected through the cylinder surface since the static pressure around the circumference of the cylinder varies when exposed to an oncoming flow and the fact that the tubing from the different chambers are confluenced before connected to the pressure source. However, the influence can be shown to be rather small. For the suction case the largest suction velocity occurs along the front stagnation line and then it decreases towards the rear. In the separated region the suction velocity is fairly constant and for a suction rate of 1.4% of the free stream velocity the suction velocity is about 6% smaller in this region as compared to the front. For larger suction rates the difference becomes smaller. In contrast, for the blowing case the smallest blowing velocity is along the frontal stagnation line and then increases and becomes constant from about 65° and downwards. In this case the maximum

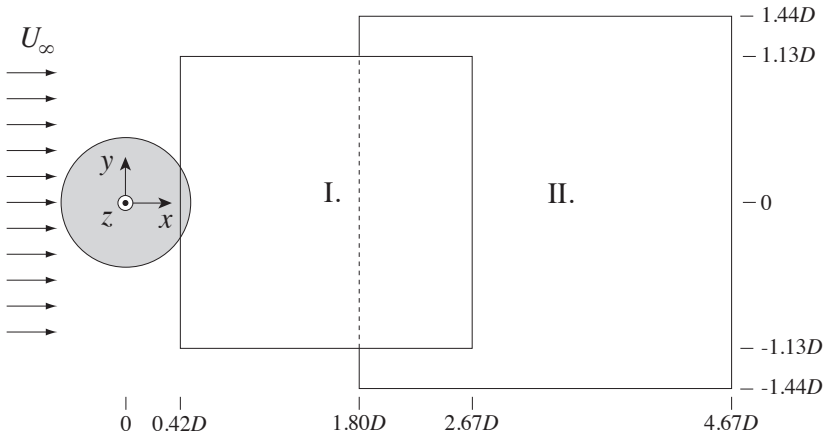

FIGURE 3. The position of the image frames and their coordinates in the PIV measurements for the suction case (I) and the blowing case (II).

variation is less than 7% and the variation decreases with increasing blowing rate, see figure 2(*b*).

2.3. *Measurement technique*

For the velocity measurements a Particle Image Velocimetry (PIV) system was used in order to allow entire flow fields to be captured instantaneously. The PIV-system used consists of a Spectra Physics 400 mJ double pulsed Nd:Yag laser operating at 15 Hz as a light source, and the camera is a double-frame Kodak ES1.0 8-bit CCD camera with 1018×1008 pixels. Furthermore, a laser arm was connected to the laser, which facilitates traversing of the laser sheet. The air was seeded with smoke particles generated by heating a glycol based liquid with a disco smoke generator, JEM ZR20 Mk II. The smoke inlet to the tunnel was in the open cross section between the end of the test section and the diffuser. Before the measurements the smoke was recirculated in the tunnel until the air became homogeneously seeded. See figure 1 for an illustration.

Since the location of the events of interest in the wake changes depending on whether suction or blowing is applied through the cylinder surface, the frame location of the PIV-images had different positions and sizes in the suction and blowing cases. Figure 3 shows the two frames where the suction case (I) starts by overlapping the cylinder at $x = 0.42D$ and stretches up to $x = 2.67D$ with $y = \pm 1.13D$. In the blowing case (II) the frame starts at $x = 1.80D$ and ends at $x = 4.67D$ with $y = \pm 1.44D$. The latter is slightly larger due to the wake growth, and the two regions where chosen so that they would capture the position of maximum backflow in their respective cases.

In the post-processing of the measured data conventional validation criteria were applied. Displacements of the particles larger than 25% of the interrogation area length was not allowed, in order to avoid low-velocity bias due to loss-of-pairs. This criterion is set before the measurements by choosing the appropriate time between the two consecutive captured images. Furthermore, spurious measurement errors were eliminated by applying a Peak-Value-Ratio (PVR) of 1.2, implying that the ratio of the highest to the second highest peak in the cross-correlation is not allowed to be smaller than 1.2. The result of the post-processing is a 62 grid with a grid point spacing of 1.85 mm and 3844 velocity vectors.

3. Vortex detection methodology

A vortex detection algorithm was developed in order to examine the effect on small-scale structures in the wake behind the porous cylinder when subjected to different levels of suction or blowing. Several different methods for detecting vortices are available and a review and comparison of the most common ones is found in Jeong & Hussain (1995). In this study they reported on the λ_2-method, which is shown to be the most appropriate method to detect vortices in a velocity field. The λ_2-method has been widely accepted since its introduction and has been implemented, as a post-processing option, into many numerical codes. However, for the λ_2-method to be applicable, the Hessian of the pressure, i.e. all three components of the velocity gradient tensor, has to be known. This implies that the velocity vector has to be known in the entire flow volume, which experimentally is unfeasible. From two-dimensional velocity fields, as in PIV-measurements, Adrian *et al.* (2000) showed that by applying a high-pass filter on the full velocity field the small-scale velocity structures are revealed. Vortices were then detected through a two-dimensional version of the Δ-method proposed by Chong *et al.* (1990). This method is based on the search for complex eigenvalues of the velocity gradient tensor, which implies that the streamlines have closed circular paths and used as the definition for a vortex. The same methodology will be used in the following.

3.1. *Decomposition of the velocity field*

The high-pass filtering of the full velocity field, $\mathbf{u}$, is performed by convolving a low-pass filter on $\mathbf{u}$. This low-pass filtered velocity field, $\bar{\mathbf{u}}$, is then subtracted from the full velocity field, which consequently gives the high-pass filtered velocity field $\mathbf{u}''$. The decomposition may be written as,

$$\mathbf{u}'' = \mathbf{u} - \bar{\mathbf{u}} \,, \tag{1}$$

and in figure 4 an example of the decomposition is shown. Here, an instantaneous velocity field behind the porous cylinder subject to a suction velocity of

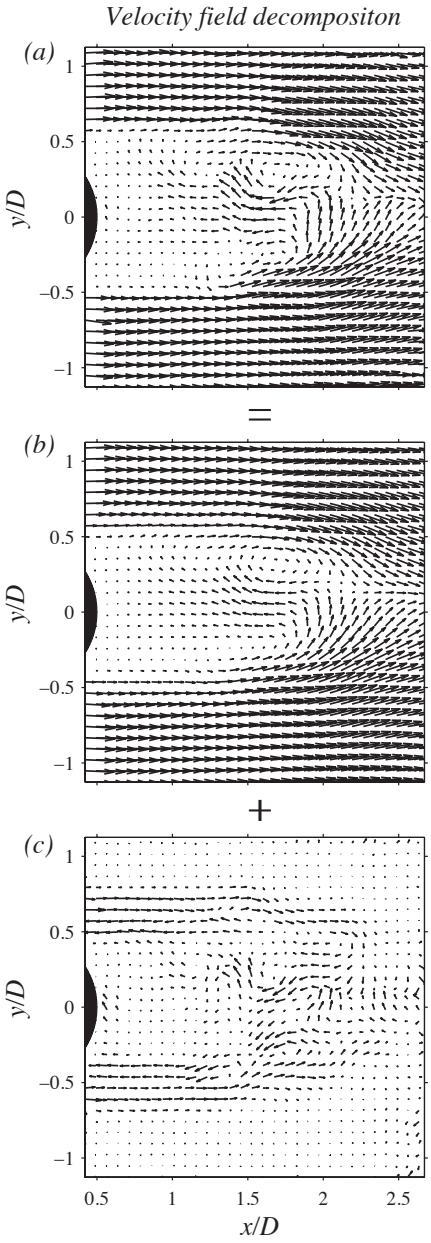

FIGURE 4. (*a*) An instantaneous velocity field, decomposed into a large-scale (*b*) and a small-scale (*c*) velocity field.

2.6% of the freestream velocity has been decomposed. In figure 4(a) the full velocity field is shown and in (b) and (c) the large scale and small-scale velocity fields are depicted, respectively.

In accordance with Agrawal & Prasad (2002), a Gaussian filter that averages the single (m, n)-point with the surrounding points is used for the decomposition, so that

$$\bar{\mathbf{u}}(m,n) = \frac{\sum_{j=-k}^{k}\sum_{i=-k}^{k} g(i,j)\mathbf{u}(m-i,n-j)}{\sum_{j=-k}^{k}\sum_{i=-k}^{k} g(i,j)} \ , \tag{2}$$

where (i, j) is the step in x and y, respectively, and k is the *radius*. The Gaussian kernel (g) is defined as

$$g(i,j) = \exp\left[-\frac{(i\Delta x)^2 + (j\Delta y)^2}{2\sigma^2}\right] \ , \tag{3}$$

where Δx and Δy are the grid spacing and σ is the padding of the filter. The parameters k and σ were chosen by introducing an anisotropy measure d^2_{rms} of the $\mathbf{u}''$–field, which is defined as the absolute value of the normalised difference between the velocity variance components,

$$d^2_{rms} = \left|\frac{u^2_{rms} - v^2_{rms}}{U^2_\infty}\right| \ . \tag{4}$$

The maximum value of d^2_{rms} is compared for varying combinations of k and σ, and $\max\{d^2_{rms}\} \leq 0.01$ was decided to be a suitable criterion after field inspections. In this way the filter parameters can be chosen in a consistent manner and with a qualitative measure of the filter strength. For the present flow field both k and σ were chosen to be equal to 5.

3.2. *Detection of vortices*

As previously stated, the vortex definition and detection method by Chong *et al.* (1990) is used to detect the small-scale vortices. This method was also suggested and used by Adrian *et al.* (2000). It amounts to identify regions where the eigenvalues of the two-dimensional high-pass filtered velocity gradient tensor,

$$\nabla\mathbf{u}''_{2D} = \begin{bmatrix} \frac{\partial u''}{\partial x} & \frac{\partial u''}{\partial y} \\ \frac{\partial v''}{\partial x} & \frac{\partial v''}{\partial y} \end{bmatrix} \ , \tag{5}$$

are complex. The eigenvalues of $\nabla\mathbf{u}''_{2D}$ are either real or complex conjugate and consequently vortices can easily be identified by plotting contours of the regions where the imaginary part λ_{ci} of the eigenvalues are positive. A threshold level is required to have a distinct and reasonable boundary between the vortices.

The value of the chosen threshold level was found by studying the output of the vortex identification at different levels. Plotting contours of $\lambda_{ci} = 15$ turned out to be a good choice to distinguish vortices with reasonable boundaries in these particular wake flow mesurements.

3.3. *Vortex statistics*

For each instantaneous velocity field image the vortices are first identified and then their position, size, strength and circulation are determined. These vortex parameters are stored for statistical analyses before the next instantaneous velocity field is being processed.

The position within each identified region, where the highest λ_{ci} is found determines the centre of the vortex expressed in the discrete coordinates x and y. The highest eigenvalues in each region is also, per definition, the swirl strength of the vortex, (see e.g. Zhou *et al.* 1999). Futhermore, the area of the contour region containing the imaginary eigenvalues is calculated, and a circle C around the vortex centre with an equivalent radius to this area is used as a starting point for calculating the circulation γ. This is done through direct integration along C's perimeter $\mathbf{l}$ according to

$$\gamma = \oint_C \mathbf{u}'' \cdot d\mathbf{l} \ . \tag{6}$$

The γ calculation is repeated for a continuos stepwise increase in the radius until the value of the circulation has saturated. This radius is defined as the vortex radius and its corresponding diameter will be denoted d_γ from here on.

4. Experimental results

In the following the results of the vortex analysis in the wake of a porous cylinder is reported. Vortex parameters such as vortex position, size, strength and circulation are reported for different levels of suction and blowing through the cylinder surface. The rate of suction or blowing is quantified by the parameter $\Gamma = V_0/U_\infty \times 100$, where V_0 is the velocity through the cylinder surface and U_∞ is the free stream velocity. Negative and positive values of Γ are associated with suction and blowing, respectively.

The number of PIV-image pairs along with the number of identified vortices for both the suction and the blowing cases at the different levels of Γ are presented in table 1. A relatively high number of samples have been collected for different levels of suction and blowing, which makes the statistical comparison reliable. Since different frames have been used for the suction and the blowing cases (see figure 3), the study limits itself to relative changes from the reference $\Gamma = 0$ in both the suction and the blowing cases. A direct comparison of the effect of suction versus blowing is, thus, not possible.

suction			blowing		
Γ	no. of IP	no. of vortices	Γ	no. of IP	no. of vortices
0	1054	13122	0	1022	11587
-0.7	1054	19943	0.7	1086	13323
-1.4	1054	17996	1.4	1054	12005
-1.9	1054	16494	1.9	1054	12942
-2.6	1054	19273	2.6	1024	13384
-3.2	1054	15030	3.2	1055	14996
-3.9	1054	19109	3.9	1054	15706
-5.0	1118	19503	5.0	1054	21189
-6.5	401	3574	6.5	1054	17069

TABLE 1. The number of PIV-image pairs (IP) taken during the experiments and the number of detected vortices for each Γ in both the suction and the blowing cases.

An example of an instantaneous velocity field for the natural case ($\Gamma = 0$) along with a case where suction is applied through the cylinder surface ($\Gamma = -5$) is shown to the left in figure 5, frame I. To the right in this figure the positions where $U < 0$, which indicates the presence of back-flow, are marked with (+)-symbols for the two cases. Figure 5, frame II, shows similar instantaneous velocity fields, but for the blowing case. The instantaneous back-flow figures are representative for their respective cases. In the suction case one can see that the backflow-region moves closer to the cylinder while in the blowing case it moves away from the cylinder.

From these instantaneous images one can calculate the back-flow coefficient, χ, which is defined as the amount of time there is back-flow in a particular position in the flow field. A χ-value of 1 means that there is always back-flow in this position and 0 means the opposite. Figure 6, frame I and frame II, shows the mean velocity field along with the back-flow coefficient. One can here see how the region of back-flow decreases and increases for the suction and the blowing cases, respectively. Furthermore, the white dot shows the location where the back-flow coefficient has its maximum.

In a mean perspective moderate levels of suction or blowing have a large impact on the wake. With suction the wake decreases in size and for Γ about -6 the flow around the cylinder becomes *potential-like* and hence the drag is significantly reduced compared to the natural case ($\Gamma = 0$). With blowing the *twin-vortices* in the wake, appearing in the mean velocity field, grow in size, which causes a large region of back-flow and consequently the drag increases. This was quantified by Fransson *et al.* (2004), where the drag coefficient was plotted versus Γ.

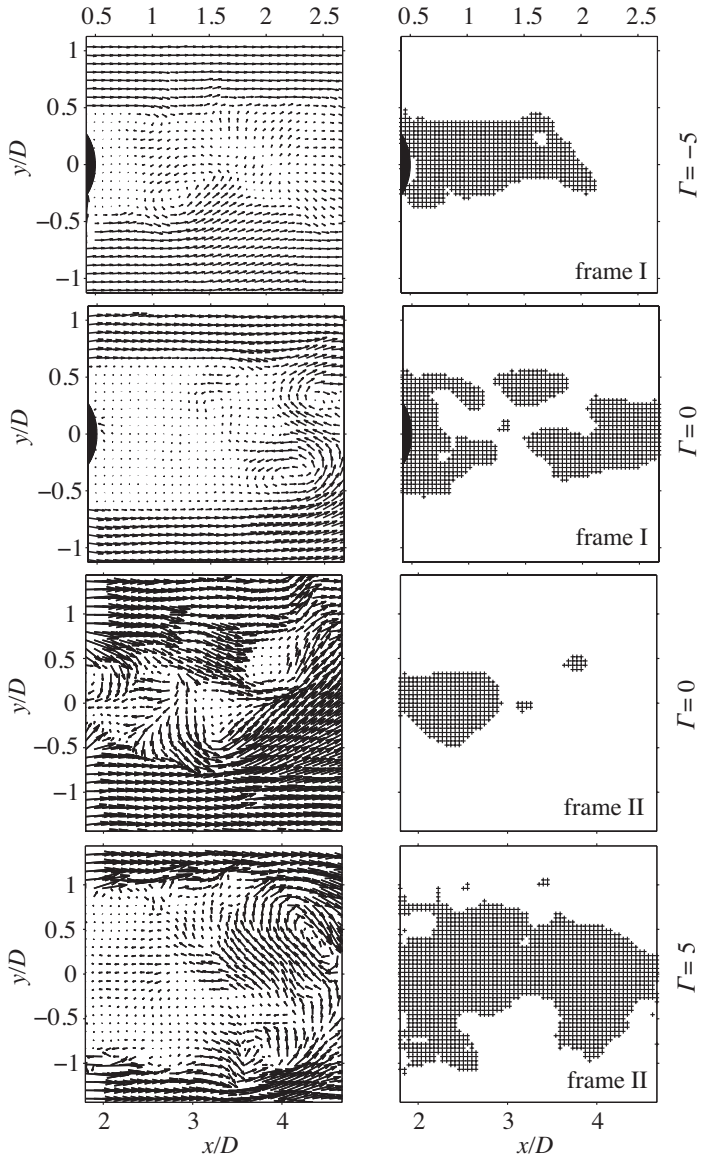

FIGURE 5. Instantaneous vector velocity fields (left column) and their corresponding back-flow ceofficent maps (right) for the natural case and when suction ($\Gamma = -5$) and blowing ($\Gamma = 5$) are applied.

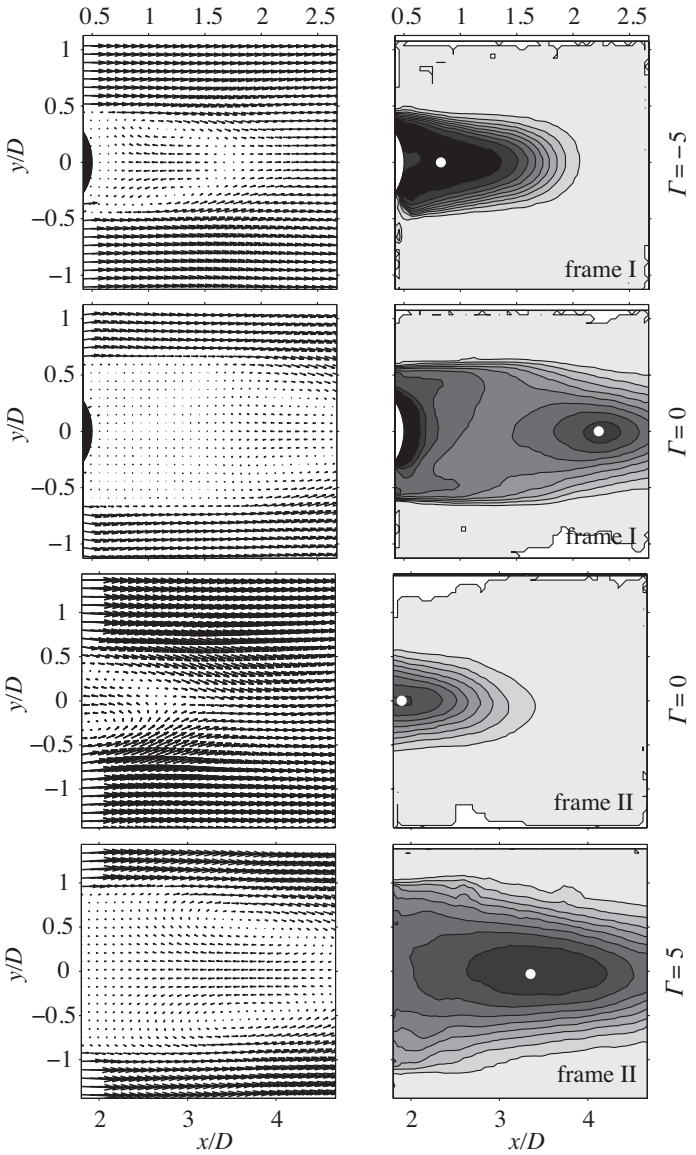

FIGURE 6. Mean vector velocity fields (left column) and their corresponding back-flow coefficient maps (right column) for the natural case ($\Gamma = 0$) and when suction ($\Gamma = -5$) and blowing ($\Gamma = 5$) are applied. The filled contours correspond to an increment of 0.1 from 0 (white) to 1 (black).

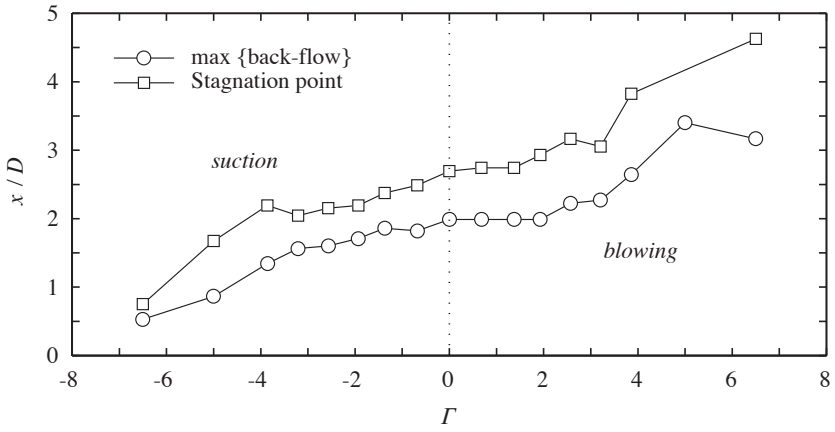

FIGURE 7. The effect of suction and blowing on the near-wake extension. Both the position of maximum back-flow and the stagnation point (or the confluence point of the two stationary vortices) can be seen as a measure of the vortex formation length. The averaged ratio between the two is 1.42.

The size of the wake may be estimated by either the position of maximum χ (i.e. the white bullets in figures 6) or the stagnation point in the wake. The latter corresponds to the confluence point of the two stationary *twin-vortices*. In figure 7 these two measures of the vortex formation length are plotted versus Γ. From this figure it is clear that suction reduces the extent of the near-wake, and the maximum back-flow and the stagnation point measures decrease with 60% and 32%, respectively, from $\Gamma = 0$ to $\Gamma = -5$. In contrast, blowing increases the near-wake extension with 70% and 66%, respectively, from $\Gamma = 5$ to $\Gamma = 0$.

Having stated that moderate levels of suction or blowing have a large impact on the mean velocity field around the cylinder, it is interesting to see how the vortices in the wake are affected. Starting with the suction case, and followed by the blowing case, the statistics for the vortices will be presented.

4.1. *Suction*

Location of vortices. In figure 8(a) the Probability Density Functions (PDFs) of the streamwise position of the detected vortices are plotted. The number of bins are 30, and the PDFs are normalised such that the area under the individual curves equals unity. Furthermore, to improve visibility the plotted curves have been smoothed by averaging each point with the neighbouring four points. Here, one may observe that the position of maximum probability moves from

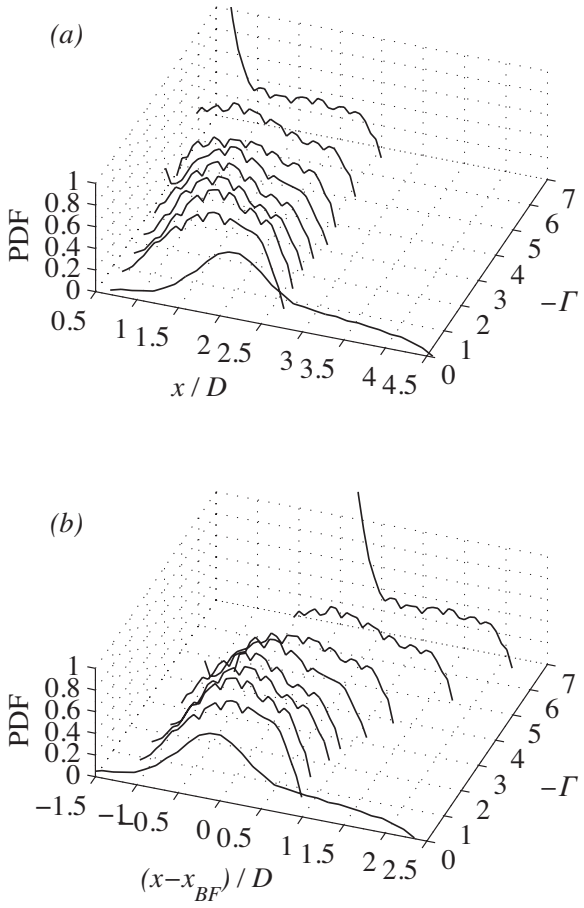

FIGURE 8. (*a*) PDFs of the streamwise position of vortices. (*b*) Same as in (*a*), but scaled by the position of maximum backflow, x_{BF}.

about $x/D = 2.2$ downstream of the cylinder for $\Gamma = 0$ to about $x/D = 1.2$ for $\Gamma = -5$. It turns out that this position moves along with the position of maximum backflow (x_{BF}) in the wake. This is illustrated in figure 8(*b*), where x_{BF} from each suction rate has been subtracted from the streamwise position. The location of the maximum value of the PDFs are now close to zero, i.e. independent of the suction rate. At high levels of suction ($\Gamma < -5$), the wake almost disappears, and the result might differ from lower levels. For $\Gamma = 0$ the results for the two frames, both the suction case (frame I) and the blowing case (frame II), have been combined, which shows that no other peaks are present. It should be noted that vortices close to the streamwise boundaries

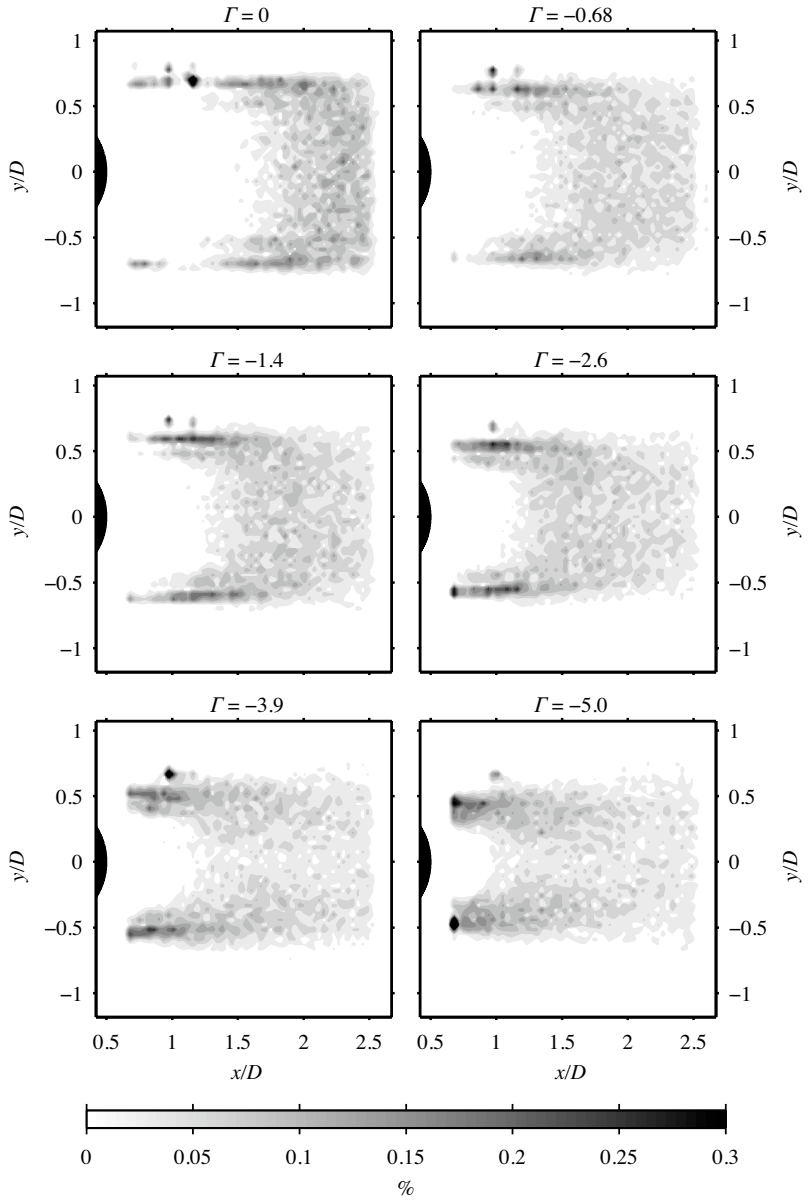

FIGURE 9. Percentage of the total number of vortices in each point where vortices are detected. The number of contour steps are 30.

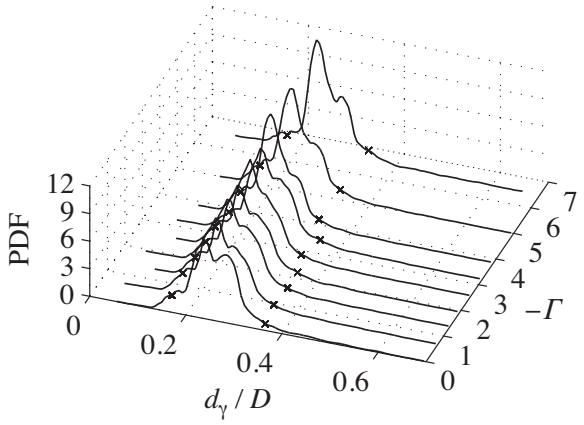

FIGURE 10. PDFs of the diameter of the vortices. (×)-symbols mark the limits of the 5% smallest and 5% largest vortices. To improve visibility, the plots are truncated at $d_\gamma/D = 0.7$, disregarding at most 0.09% of the data.

of the frame may be partly outside the frame and thereby disregarded by the vortex detection program. This causes the PDFs of the streamwise position of the vortices to end rather abrupt, especially for high levels of suction, which should be interpreted as a limitation of the detection program rather then the absence of vortices. Furthermore, to avoid spurious vectors near the cylinder, the program detects vortices only for $x/D > 0.6$.

While figure 8 indicates the probability for vortices to occur in a certain streamwise position, figure 9 shows the number of vortices in percentage of the total number of vortices in each point where vortices are detected. The figure shows that, as suction increases the vortices, which initially is quite uniformly distributed in the wake, move from the centre of the wake towards two streaky regions aligned with the streamwise tangents of the cylinder ($y/D = \pm 0.5$). The streaky regions seem to be divided into an inner and an outer streak with a larger amount of vortices in the outer one.

Vortex size. Figure 10 shows the PDFs of the vortex diameters d_γ, defined as the saturation value of the circulation when stepping out from the vortex core (cf. section 3.3). The number of bins used for each PDF is 100 and the plotted curves are normalised and smoothed as previously described. As seen in the figure, suction have little affect on the most common vortex diameter, which in average, over all suction cases is $0.23D$. The (×)-symbols for each Γ mark the limits of the 5% smallest and 5% largest vortices.

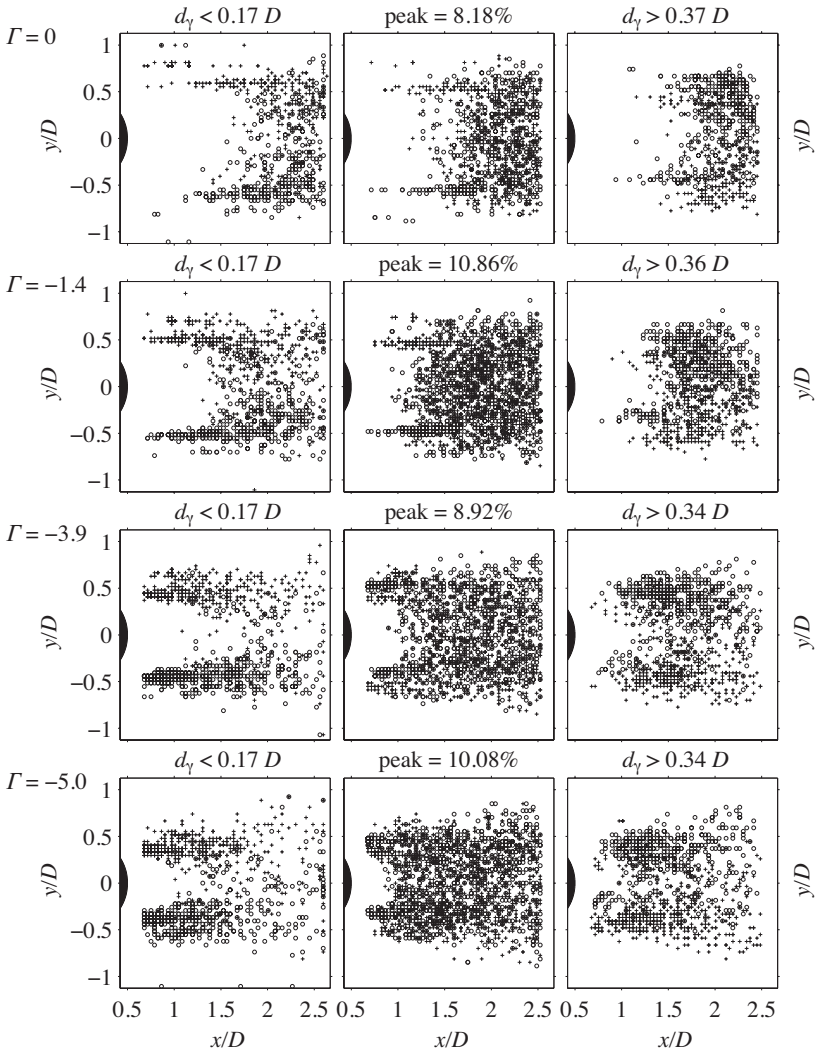

FIGURE 11. The position of the vortices corresponding to the smallest, most common and largest vortex sizes. Left column: shows the 5% smallest vortices. Mid-column: shows the vortices within ±0.5% of the peak value in the PDFs. The subtitle shows the amount of vortices in percentage of the total number of vortices. Right column: shows the 5% largest vortices. (+) and (∘)-symbols correspond to CCW and CW rotational directions, respectively.

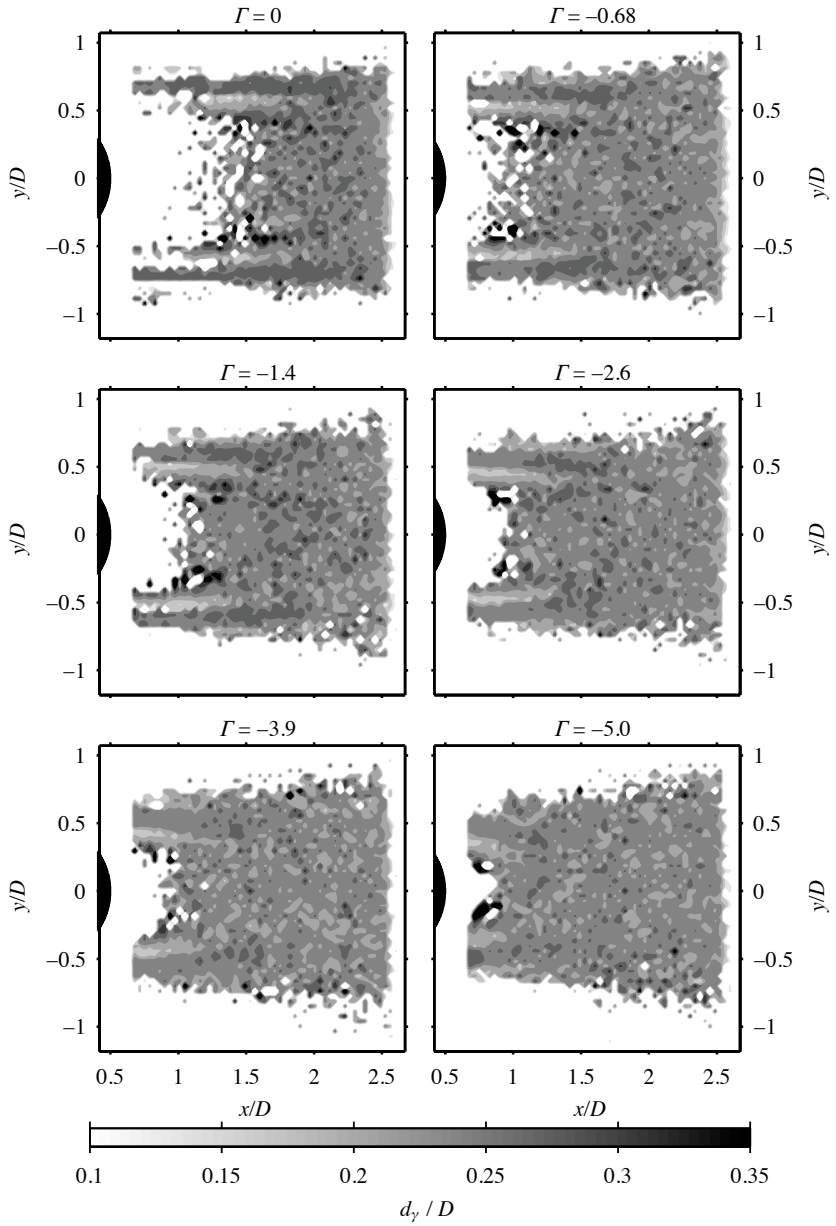

FIGURE 12. Mean vortex diameter in each point. The number of contour steps are 10.

Figure 11 shows, in the left and right columns, the location of the 5% smallest and 5% largest vortices, respectively, together with their corresponding cut-off values which is given in each subtitle. The mid-column shows the location of the vortices, which have a diameter falling within $\pm 0.5\%$ of the peak value from the PDFs in figure 10. The amount of vortices within this range is about 10% of all the detected vortices. Here, the rotational direction of the vortices are also shown, which is given by the sign of the circulation. Vortices with positive circulation are marked with (+)-symbols, which by definition means a counter-clockwise (CCW) rotational direction, while vortices with negative circulation are marked with ($\circ$)-symbols and hence, have a clockwise (CW) rotational direction. The mid-column shows that vortices with the most common diameter are quite uniformly distributed in the wake and that both CCW and CW rotational vortices are encountered. Looking at the smaller (left column) and the larger (right column) vortices, one can see how they organize themselves into streamwise streaky regions, especially for the smaller vortices, as suction increases. A closer look reveals that the smaller vortices have the opposite rotational direction compared to the larger vortices, which may imply that they correspond to secondary vortices induced by the larger primary ones.

In figure 12 the mean value of the vortex diameters that have been detected in each point is shown as a filled contour plot. It shows that the streaky regions of smaller and larger vortices discussed in relation with figure 11 do not coincide since they are revealed in this mean perspective contour plot. However, for $\Gamma \leq -5$ the streaky regions have essentially disappeared. Furthermore, one may note that the presence of vortices (any size) moves upstream and closer to the cylinder as suction is increased.

Vortex strength. The PDFs of the vortex strength, λ_{ci}, are shown in figure 13 for the different suction levels. The most common vortex strength seems to be more or less unchanged for the different levels of suction. The mean vortex strength is about $\lambda_{ci} = 18.4 \pm 1$ and the limits for the 5% weakest and 5% strongest vortices are marked with ($\times$)-symbols. The number of bins are 100, and the curves are normalised and smoothed in the same manner as in previous plots.

Vortices with the most common strength have a similar distribution in the xy–plane as the the most common vortex diameter. This is realized by comparing the mid-columns of figures 11 and 14. The left and the right columns in figure 14 show the 5% weakest and 5% strongest vortices, respectively. Since the peak value is close to the limit of the 5% weakest vortices (cf. figure 13) the distribution of the left and mid-columns look quite similar. On the other hand, looking at the stronger vortices (right column) one finds that, as the suction level increases, the vortices move away from the wake centre and align themselves in streaky streamwise regions around the shoulders of the cylinder ($y/D = \pm 0.5$). Furthermore, one may conclude that the rotational direction

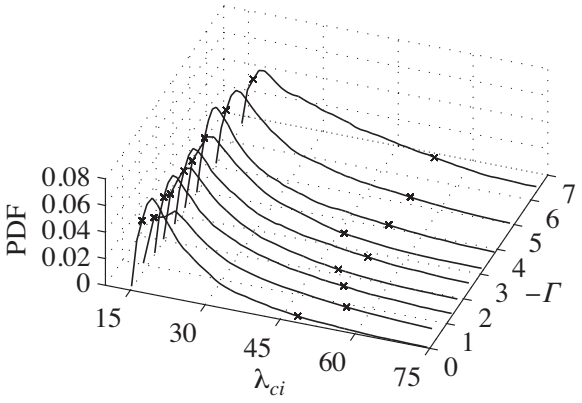

FIGURE 13. PDFs of the vortex strength for different levels of suction. The limit of the 5% weakest and 5% strongest vortices are marked with (×)-symbols. To improve visibility the results have been truncated at $\lambda_{ci} = 75$, disregarding at most 0.6% of the data.

of the stronger vortices is solely determined by on which side of the centre line they are located, which intuitively can be related to the shedding of vortices from the cylinder. The corresponding cut-off limits of the 5% weakest and strongest vortices are shown in the subtitles of each subfigure in figure 14. One may conclude that the vortices are intensified with increasing suction since both the limits increases with suction, which may be interpreted as a shift of the PDFs in the direction of stronger vortices.

The mean value of of the vortex strengths in each point where vortices have been detected is shown as a filled contour plot in figure 15. Here, the same behaviour as in figure 14 is found , i.e. as suction increases, stronger vortices form along the streamwise tangents of the cylinder, while weaker vortices are dominant in the centre of the wake. Furthermore, one may note that the presence of vortices (any size) moves upstream and closer to the cylinder as suction is increased.

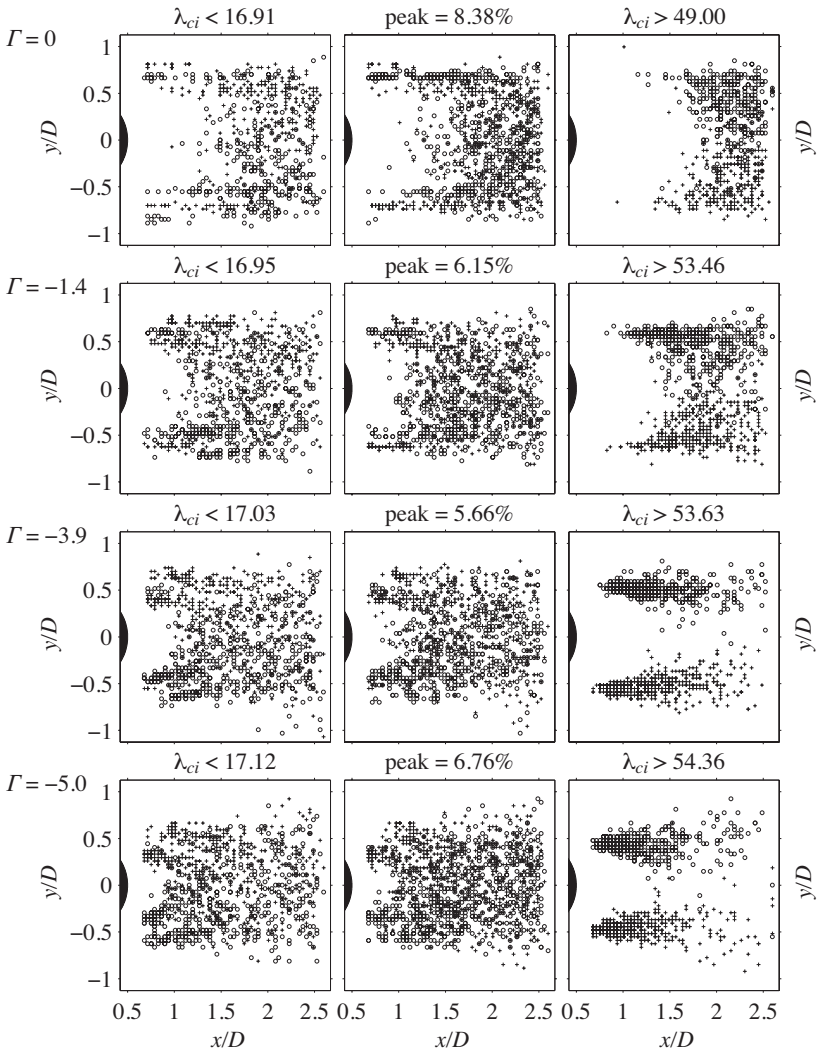

FIGURE 14. The position and limit of the 5% weakest vortices (left column), the position and percentage of the total number of vortices within ±0.5% of the peak value (mid-column) and the position and limit of the 5% strongest vortices (right column). (+)- and (∘)-symbols have CCW and CW rotational direction, respectively.

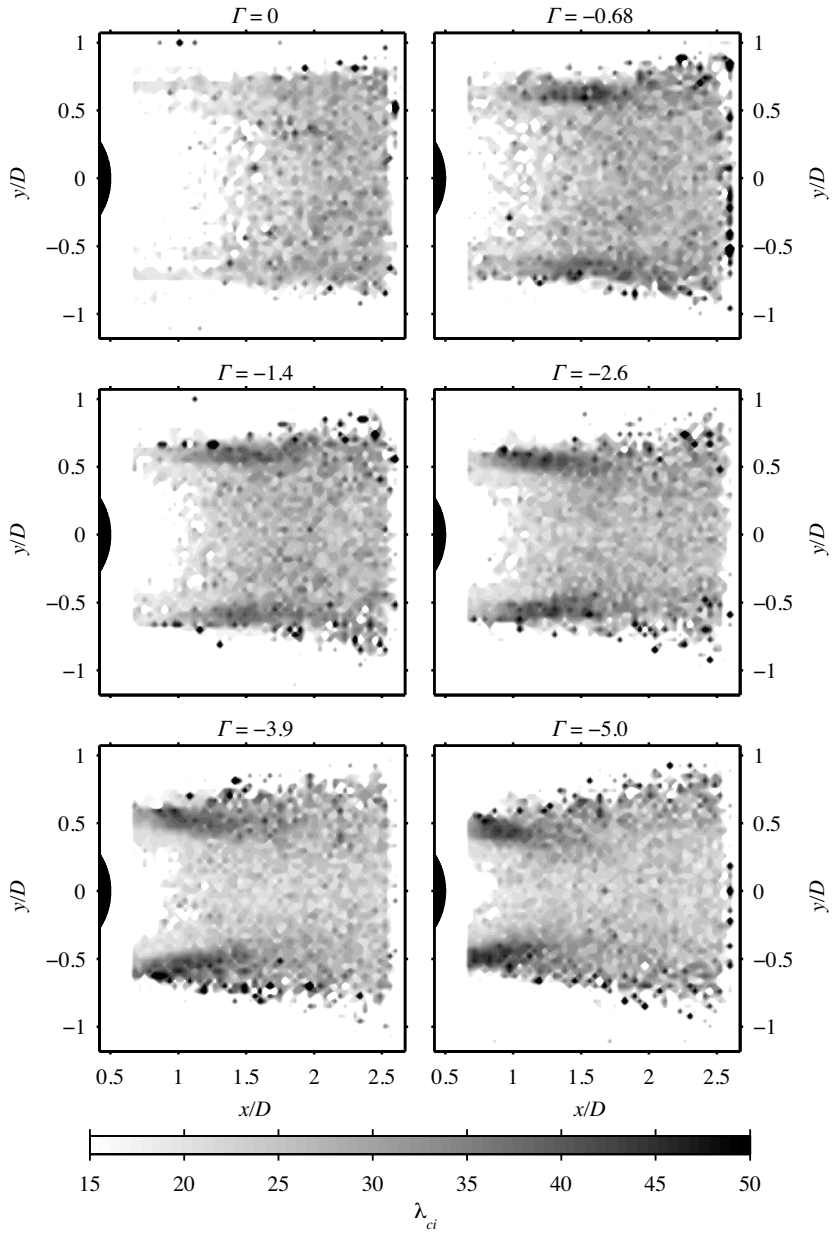

FIGURE 15. Mean vortex strength in each point where vortices are detected. The lower limit is determined by the threshold (=15) in the detection code and the upper limit has been trunkated at $\lambda_{ci} = 50$ to enhance visibility. The number of contour steps are 25.

Vortex circulation. In figure 16 the PDFs of the vortex circulation, γ, are shown. In order to increase visibility every second PDF is plotted with a bold line. For a large number of detected vortices and provided that the geometry is symmetric but also that suction, when applied, is applied uniformly, the circulation should have a symmetric distribution around zero. Both on the positive and the negative half of γ one may observe two peaks in the distribution. The highest peak is at $\gamma = \pm 0.04 U_\infty D$ with a maximum deviation of $\gamma = \pm 0.01 U_\infty D$. The second peak, appearing at higher absolute values of γ relative to the maximum peak, is more pronounced on the negative half of the PDF. It is persistent up to suction levels of $-\Gamma < 5$, whereafter it disappears. As for the other vortex parameters the limits for the 5% lowest and 5% highest values of circulation are marked with (×)-symbols in figure 16.

In figure 17 the vortices corresponding to the 5% lowest (left column) and 5% highest (right column) values of the circulation together with the vortices within ±0.5% of the maximum peak value (mid-column). A natural choice of vortex strength measure would be the circulation of a vortex. By comparing figures 14 and 17 one may conclude that the two measures give similar results. While the circulation γ is a measure with some physical relevance the λ_{ci} measure is not. On the other hand, λ_{ci} is the key parameter in the chosen vortex detection method (cf. section 3.2) and is at hand as soon as a vortex has been identified in the velocity field, while the circulation has to be calculated in

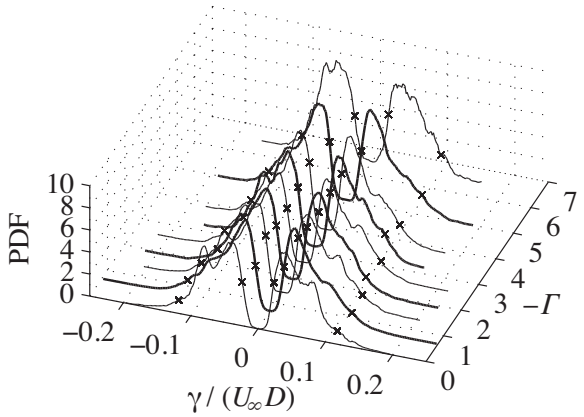

FIGURE 16. PDFs of the vortex circulation for different levels of suction. (×)-symbols mark the limits of the 5% smallest and 5% largest circulation based on the absolute value. To enhance visibility every second line is bold. The PDFs have been truncated at $\gamma/(U_\infty D) = \pm 0.25$, disregarding at most 0.05% of the data.

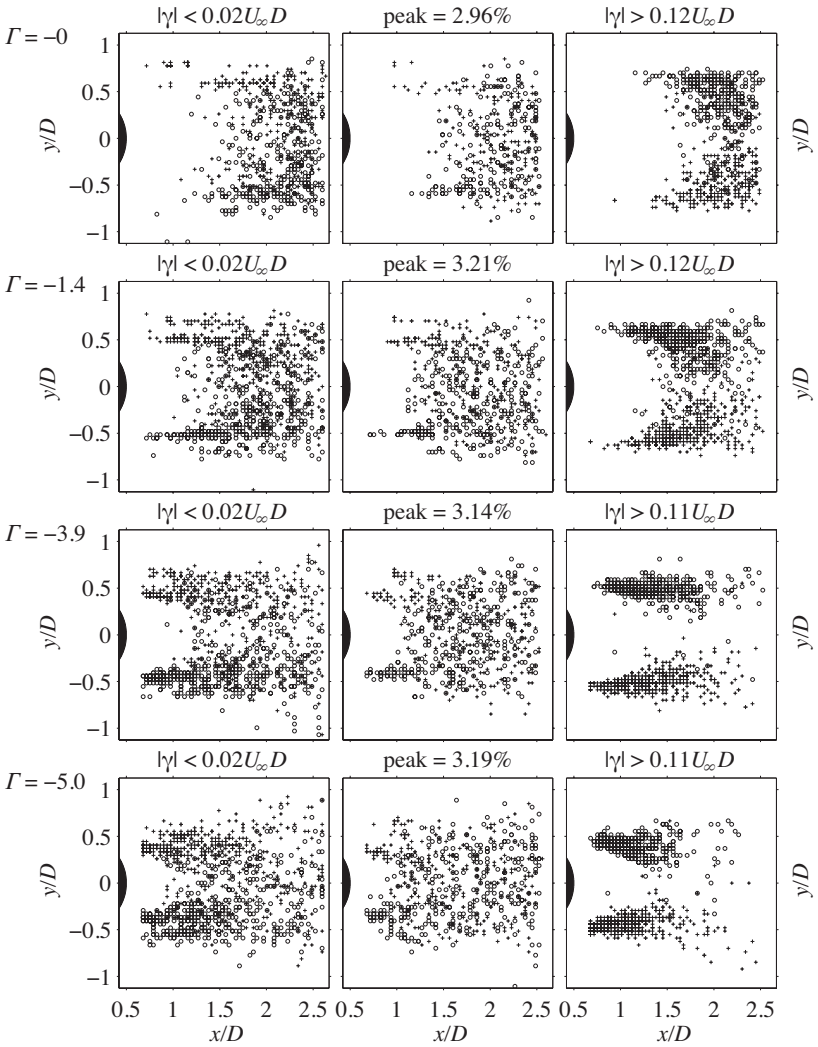

FIGURE 17. The position and limit of vortices corresponding to the 5% smallest absolute circulation value (left column), the vortex location and the percentage of the total number of vortices within ±0.5% of the absolute peak value (mid-column) and the position and limit of the vortices corresponding to the 5% largest absolute value (right column). (+)- and (∘)-symbols correspond to positive and negative circulation, i.e. CCW and CW rotational direction, respectively.

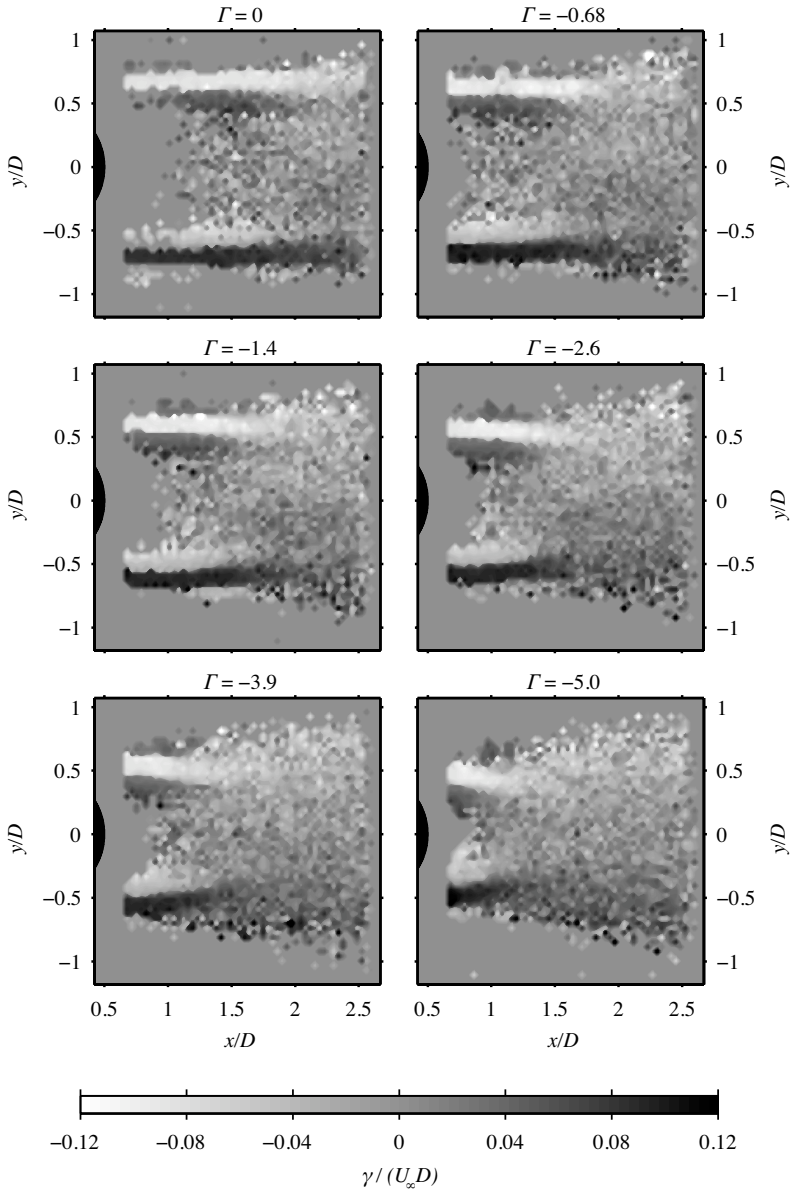

FIGURE 18. Mean vortex circulation in each point where vortices are detected. Negative circulation is clockwise rotation and positive counterclockwise. The number of countour steps are 20.

a *smart* and consistent way for each identified vortex and, hence, is not as easily accessed. In this context one should also mention that there is a clear advantage of the circulation measure over the λ_{ci} measure, which is the information of the rotational direction of the vortex. A careful inspection between figures 14 and 17 reveals some differences between the two measures, but are most likely attributed to the cut-off limits for the two different measures which will not extract exactly the same vortices. Vortices within $\pm 0.5\%$ of the maximum peak value in γ (mid-column) are more or less evenly distributed in the wake and the number of vortices in the very near wake of the cylinder increases as the suction level is increased. Otherwise, the concluding remarks are similar to what was concluded in the *vortex strength* paragraph and, hence, are not repeated here.

In a mean perspective, as shown in figure 18, the conclusion about the role up of secondary vortices due to the primary shedded vortices from the cylinder is strengthened. Streamwise streaky regions of negative (bright regions) and positive (dark regions) circulation are encountered on both sides of the cylinder. The streamwise extent of these regions are shortened and move towards the shoulders of the cylinder ($y/D = \pm 0.5$) as suction is increased. The primary vortex regions correspond to the bright one on the upper half and the dark one on the lower half in the figures. A careful inspection reveals streaky regions on both sides of the primary vortices with opposite sign, which supports the previously mentioned induction of secondary vortices.

4.2. *Blowing*

Location of vortices. Figure 19 shows the PDFs of the location of the vortices for increasing blowing, i.e. vortices identified in frame II. The number of bins are 30 and the curves have been smoothed by averaging every point with the neighbouring four. For $\Gamma = 0$ the distribution is combined with frame I and we recall the observation of one single peak in the PDF around $x/D = 2.2$, which is located in the overlap region between frame I and II. For blowing, in the interval $0 < \Gamma < 5$, it is shown that there is no major difference in the streamwise position of identified vortices nor the peak value in the PDFs, but there are two general remarks on the observed distributions that have to be mentioned. Firstly, the distributions start quite abrupt at around $x/D = 1.8$ and, secondly, for $\Gamma > 5$ there is a significant increase of identified vortices at the inlet boundary of frame II. The simplest explanation would be to blame the vortex detection program and to classify the remarks as being unphysical, however, in the process of analyzing the vortex parameters explanations will be attempted and we will consequently come back to above remarks in the end of this section.

In figure 20 the percentage of the total number of vortices in each point where vortices have been detected is shown. This confirms the unchanged distribution at lower levels of blowing, while at higher levels (here from $\Gamma = 5$) a high concentration is found along the inlet boundary of the frame, which is followed by a region with less vortices in the central region of the wake.

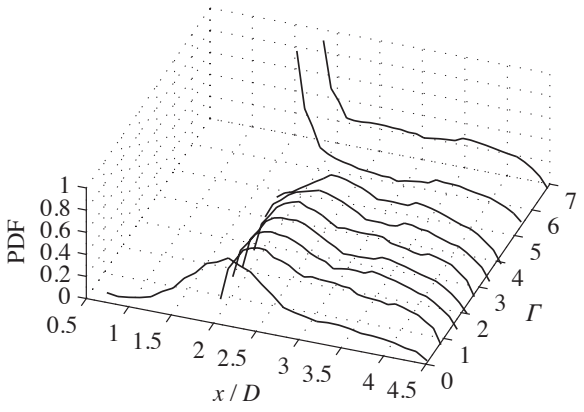

FIGURE 19. PDFs of the streamwise position of vortices for different levels of blowing.

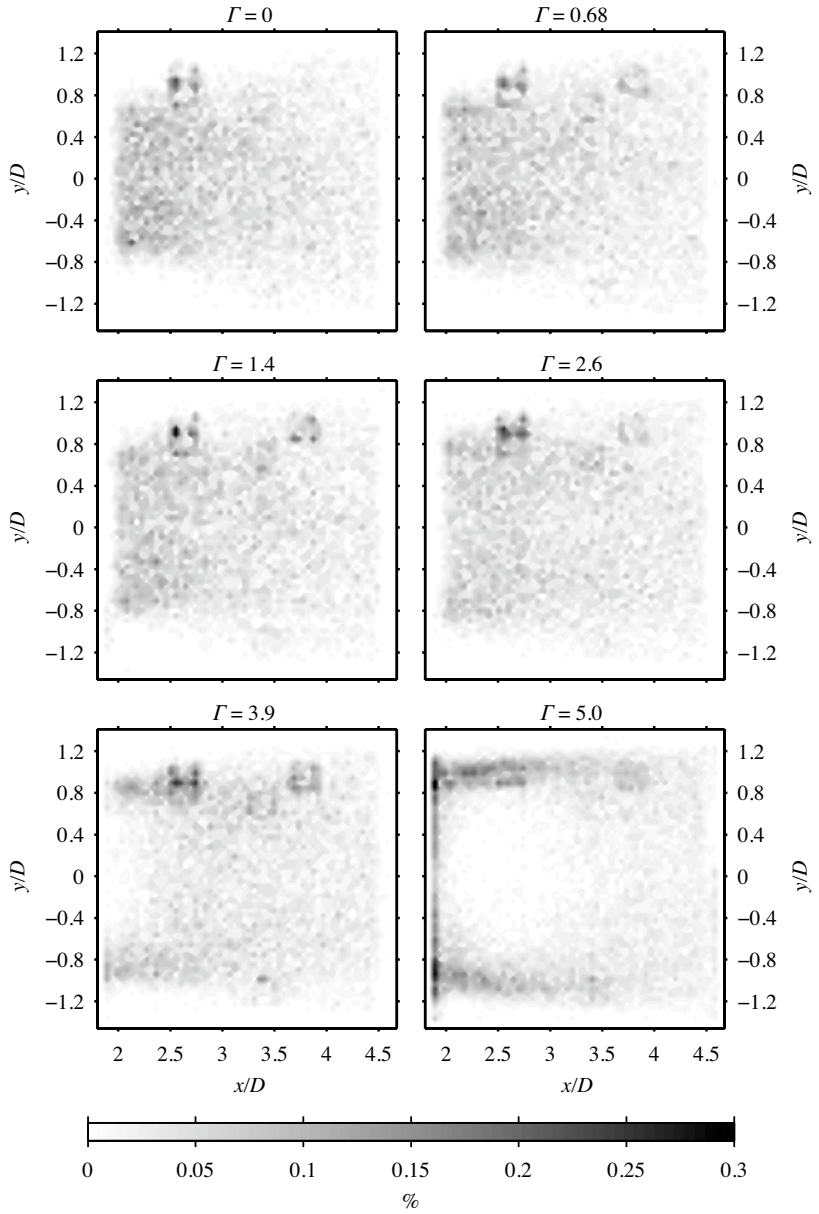

FIGURE 20. Percentage of the total number of vortices in each point where vortices are detected. The number of contour steps are 30.

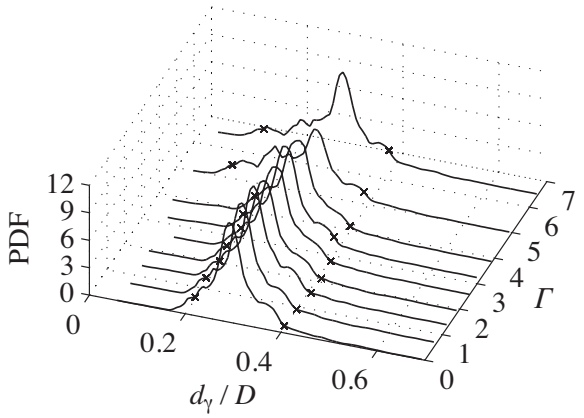

FIGURE 21. PDFs of the vortex diameters for different levels of blowing. (×)-symbols mark the limits of the 5% smallest and 5% largest vortices. To improve visibility, the plots are truncated at $d_\gamma/D = 0.7$, disregarding at most 0.1% of the data.

Vortex size. The PDFs of the vortex diameters are shown in figure 21 for different levels of blowing. These distributions are plotted in the same manner as in the suction case and with the limits of the 5% smallest and 5% largest vortices marked by (×)-symbols in the figure. One may conclude that the peak values are fairly unchanged when blowing is increased. The averaged peak value is $0.29D$, which should be compared with the averaged peak value in the suction case (figure 10) of $0.23D$. While in the suction case there is a small trend of decreasing diameters for the peak value, there is a small trend of increasing diameters in the blowing case. These trends may be explained by the actual cylinder diameter seen by the flow. A physically larger cylinder would naturally generate larger vortices in the flow field compared to a smaller cylinder, and the effect of blowing and suction causes an increase and a decrease of a fictitious cylinder diameter seen by the oncoming flow. However, a comparison between the PDFs from frame I (figure 10) and frame II (figure 21) for the natural case, i.e. $\Gamma = 0$, reveals that the distribution centered around its peak is moved towards larger diameters. This mismatch may, on the other hand, be explained by the locations of frame I and II. The largest vortices are connected to the von Kármán vortices and a central position in the flow field is the confluence point of these large eddies, which in the suction case (frame I) is just captured while in the blowing case (frame II) it is located about one third from the inlet boundary of the frame (see left column in figure 6).

Figure 22 shows the location of the 5% smallest (left column) and 5% largest (right column) vortices with their corresponding cut-off values given in

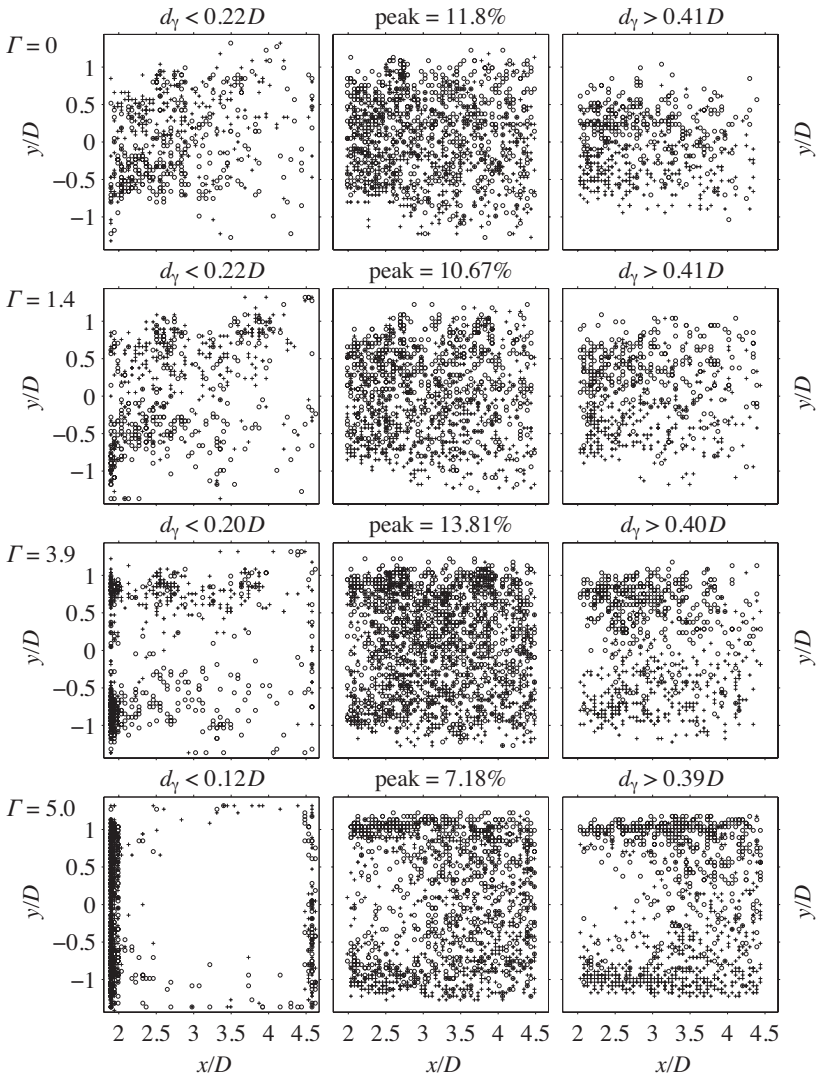

FIGURE 22. The positions and limit of the 5% smallest vortices (left column), the position and percentage of the total number of vortices within ±0.5% of the peak value (mid-column) and the position and limit of the 5% largest vortices (right column) for different levels of blowing. (+)- and (∘)-symbols have CCW and CW rotational direction, respectively.

the subtitles. In the mid-column the location of the vortices with diameters falling within ±0.5% of the peak value diameter are shown. Here, CCW and CW rotational direction are marked by (+)- and (∘)-symbols, respectively. Vortices with the most common diameter (mid-column) is quite evenly distributed in frame II. However, for the largest vortices (right column), just as in the suction case, the vortex diameters with CW and CCW rotational directions are found on the upper and lower frame halfs, respectively. For the highest blowing rate a clear increase of the wake size is observed with the largest vortices moving away from the wake centre, which is the result of an extension of the wake. For the smallest vortices (left column), the rotational direction is opposite compared to the largest, and have been induced by the primary von Kármán vortices as previously discussed for the suction case. The mean diameter in each point in the xy-plane does not reveal anything new and the figure is, hence, not reproduced here.

Vortex strength. PDFs of the vortex strength are shown in figure 23 for the different blowing rates. In average the peaks of the vortex strength is $\lambda_{ci} = 18.8 \pm 1$. The (×)-symbols mark the limits for the 5% weakest and 5% strongest vortices. In overall, one may conclude that there is no large effect for increasing blowing on the vortex strength distributions.

In figure 24 the 5% weakest and 5% strongest vortices are plotted in the left and in the right columns, respectively. The mid-column shows the vortices falling within ±0.5 of the PDF peak values in figure 23. In general one may say that the strongest vortices are connected to the largest vortices, this was the case for suction and up to blowing rates of $\Gamma = 3.9$. However, for $\Gamma \geq 5.0$

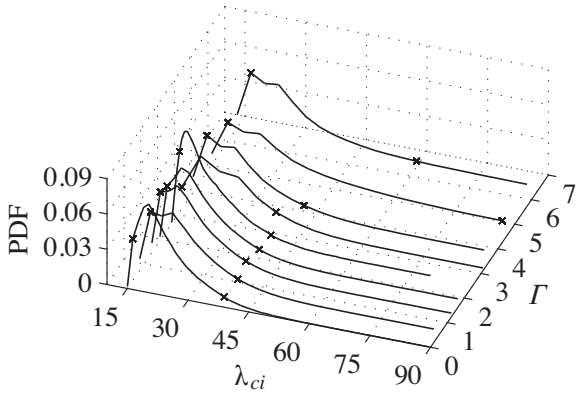

FIGURE 23. PDFs for the vortex strength. To improve visibility the results have been truncated at $\lambda_{ci} = 90$ disregarding at most 5% a of the data.

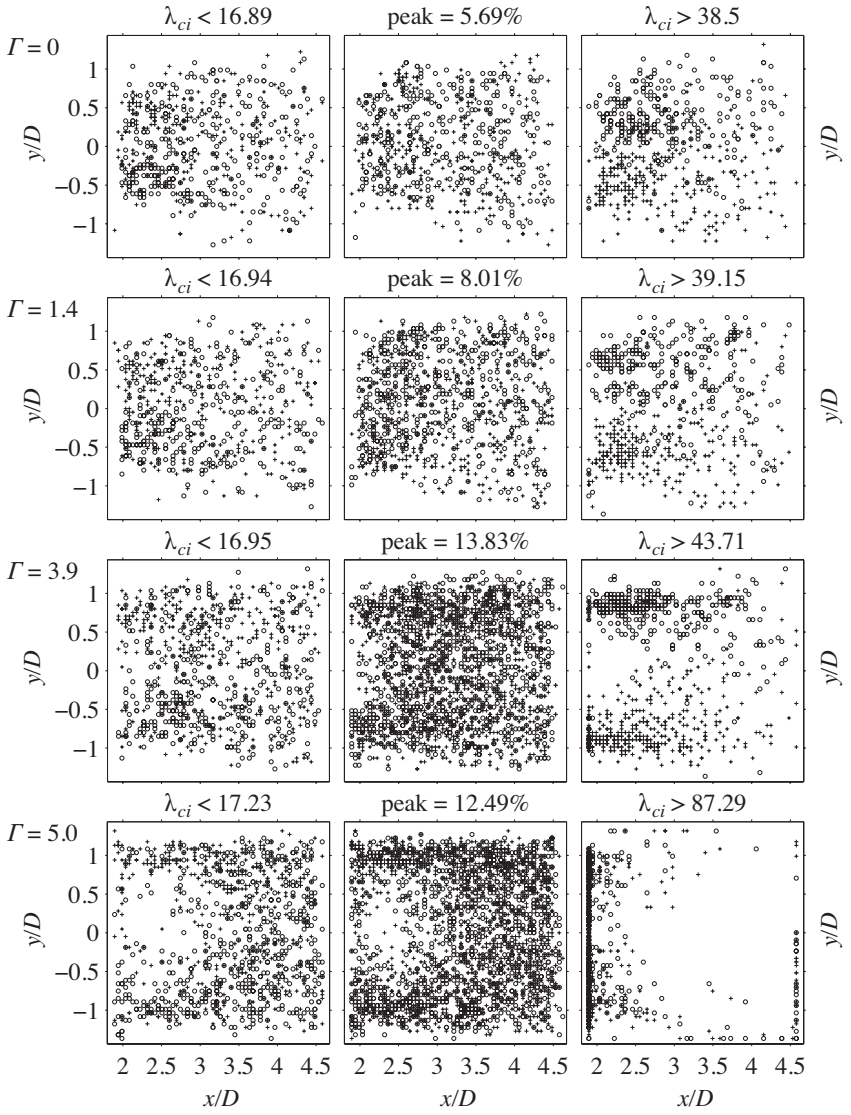

FIGURE 24. The position and limit of the 5% weakest vortices (left column), the position and percentage of the total number of vortices within ±0.25% of the peak value (mid-column) and the position and limit for the 5% strongest vortices (right column) at different levels of blowing. (+)- and (∘)-symbols have CCW and CW rotational direction, respectively.

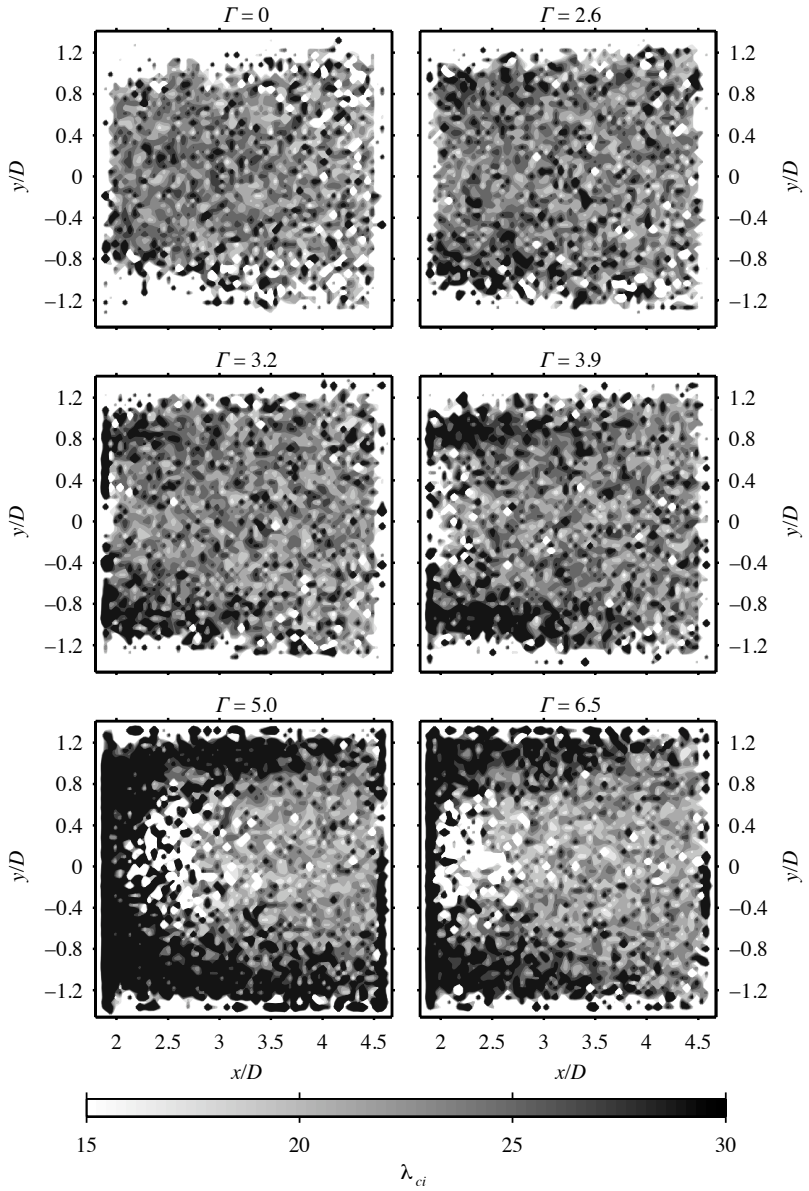

FIGURE 25. The mean vortex strength in each point where vortices are detected. The lower limit is set by threshold in the detection code and the upper limit has been trunkated at 30 to enhance visibility. The number of contour steps are 15.

it turns out to be the smallest vortices, which are strongest (compare the last rows of figures 22 and 24). This view is supported when the vortex strength is plotted in a mean perspective, see figure 25, keeping in mind the collection of the smallest vortices along the inlet boundary of the frame when blowing is increased.

Vortex circulation. For completeness the vortex circulation with increasing blowing is also shown. The results are, however, similar to the *Vortex strength* results. In figure 26 the PDFs for the vortex circulation are shown for increasing blowing. Again, the (×)-symbols mark the limits of the 5% lowest and 5% highest absolute values of the circulation. In order to increase visibility every second PDF is plotted with a bold line. The PDFs are symmetric and essentially unchanged when blowing is increased with an averaged peak value of the PDFs of $\gamma = 0.06U_\infty D$ with a maximum deviation of about $0.005U_\infty D$. The positions of the vortices, classified after their corresponding absolute circulation value, are shown in figure 27, which look very similar to figure 24.

The mean of the circulation in each point shows that the sign of the circulation and, hence, the rotational direction in a mean perspective, is governed by the location of the vortices relative the wake centre line, see figure 28. As the level of blowing increases, the mean circulation of the vortices at the upper and lower boundaries of the frame also increases. The high number of detected vortices at the inlet boundary of the frame, seen in figure 27, is not found

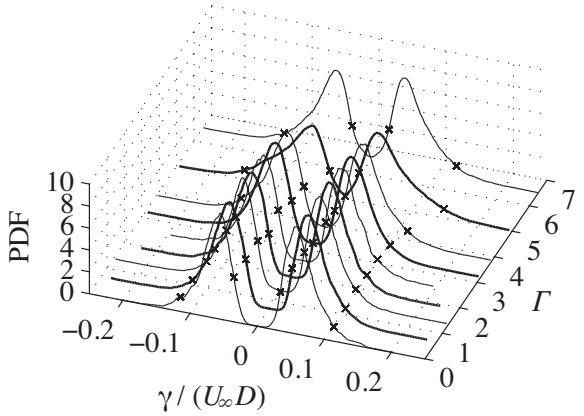

FIGURE 26. PDFs for the circulation for different levels of blowing. To improve visibility the line styles have been alternated and the results have been truncated at $\Gamma/(U_\infty D) = \pm 0.25$, disregarding at most 0.5% of the data.

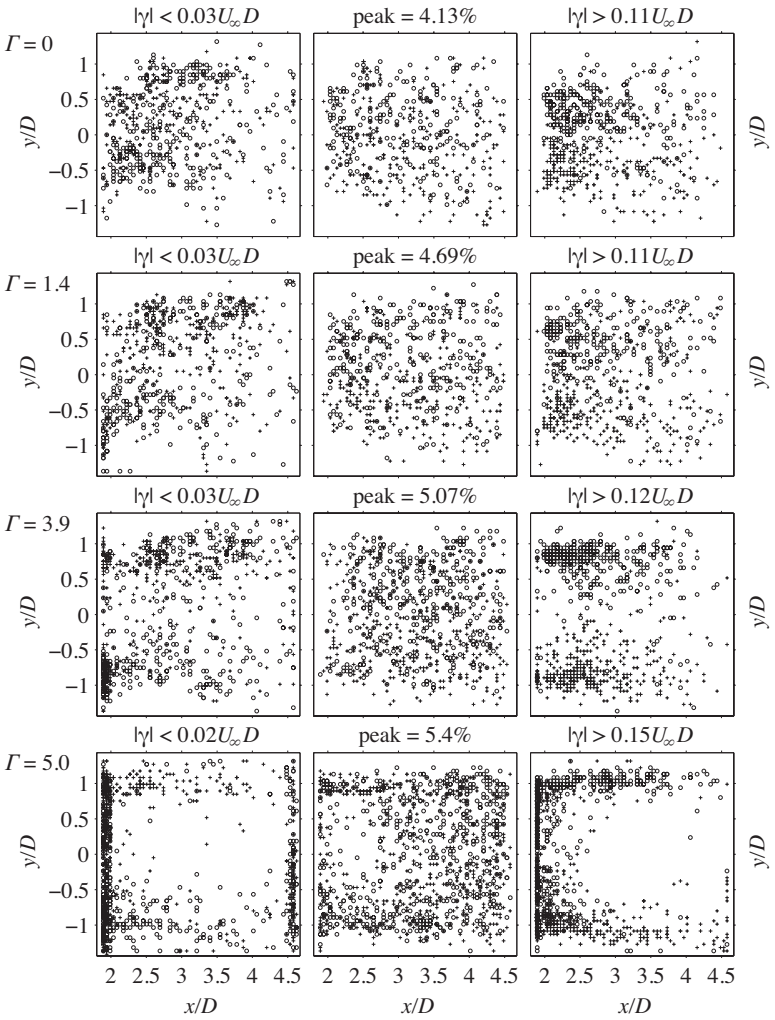

FIGURE 27. The position and limit of the vortices that have a circulation corresponding within 5% of the lowest absolute value (left column), the vortex location and the percentage of the total number of vortices that have a circulation of ±0.5% of the absolute peak value (middle column) and the position and limit of the vortices that have a circulation corresponding within 5% of the highest absolute value (right column). (+) and (∘) have positive and negative circulation, i.e. CCW and CW rotational direction, respectively.

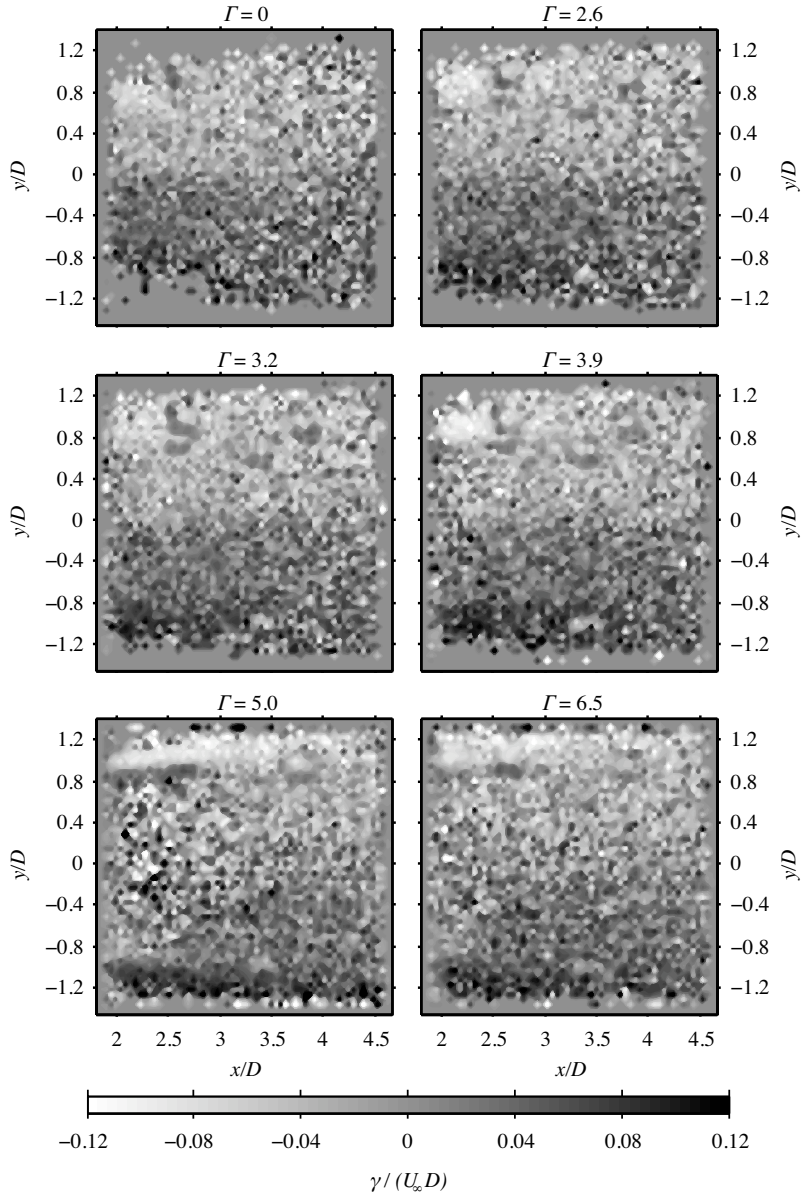

FIGURE 28. Mean vortex circulation in each point where vortices are detected. Negative circulation is equal to CW rotation and positive to CCW rotation. The number of countour steps are 20.

when looking at the mean value circulation, indicating that the mean of those vortices is zero.

Now, coming back to the remarks, which were stated in the first paragraph under *Location of vortices* in this section. The first remark may be explained by the sudden appearance of frame II and the way that the vortex detection program can handle this. Small vortices may be detected close to a boundary but not large vortices, since they will partly be located outside the frame and hence will be cut-out as a detected vortex. Therefore the number of detected vortices will be biased and the PDFs will show an abrupt increase from the inlet boundary due to the sudden, physical, possibility to detect large vortices. This also explains the second remark, and it is clear from figure 22 that it is the collection of small vortices at the boundary inlet to the frame which causes the significant increase in the total number of vortices along this boundary. One may further conclude that these small vortices are stronger than the largest vortices in the flow field and that they rotate in both directions.

5. Summary and conclusions

In this paper we report on the effect of continuous suction or blowing through the entire surface of a porous cylinder with the emphasis on vortex statistics. The Reynolds number is around 4 000, which implies that the boundary layers around the cylinder are laminar with a purely laminar separation and a turbulent wake. This implies that there is a wide range of both vortex sizes and strengths. Previously, it has been shown that continuous suction or blowing have a large impact on the vortex shedding frequency, mean velocity field and consequently the drag force. However, there is no information about the small-scale structures and how they are affected by suction or blowing. For this purpose a vortex detection program has been developed, which identifies vortices in two-dimensional instantaneous PIV images, with the purpose of analyzing small-scale structures in the wake behind bluff bodies. Vortex parameters such as strength, size and rotational direction, but also the locations of the vortex centres are outputs from the program. With a large number of PIV images vortex statistics may be created.

The results are presented by means of PDFs of the vortex parameters. For increasing suction the size of the wake decreases and the location of the maximum back-flow turns out to be a relevant position for the distribution of vortex location. For $\Gamma > -4$ the PDFs essentially collapse on each other when the location of maximum back-flow is subtracted from the streamwise axis.

By looking at the 5% largest/smallest and strongest/weakest vortices, and vortices within $\pm 0.5\%$ of the most common value of a particular vortex parameter, additional information is achieved and further conclusions may be drawn. Successively increasing suction creates streamwise streaky regions where small and large vortices, relative to the most common vortex size, are collected. These streamwise streaky regions move towards the shoulders of the cylinder

($y/D = \pm 0.5$) and are reduced in the streamwise direction with increasing suction. A close look reveal that the regions do not overlap and that the larger vortices are found on the outer side of the smaller vortices relative the wake centre line. The large vortices have rotational direction in accordance with the von Kármán vortices while the small vortices have the opposite rotational direction. This suggests that the larger vortices originate from the shedding of vortices from the cylinder, and may be seen as primary vortices, while the smaller vortices are secondary vortices which are induced by the primary ones.

From the vortex analysis one may also conclude that the vortices are slightly intensified with increasing suction and that the largest vortices are the strongest ones while the smallest ones are also the weakest ones. Generally speaking, the effect of continuous suction on the vortex parameters is quite week. What changes most is the location of the vortices in the xy–plane behind the cylinder.

With increasing blowing one may conclude that the peak value in the PDFs of vortex size is fairly unchanged. The averaged peak value in the blowing case is $0.29D$, which should be compared with the averaged peak value of $0.23D$ for the suction case. This means that the most common vortex diameter is between 20–30% of the cylinder diameter depending on the sign and level of Γ. Increasing suction shows a small trend of decreasing peak values while increasing blowing shows a small trend of increasing peak values.

An interesting result in the blowing case is that for high enough blowing rates ($\Gamma > 5$) there is a change in trend of the vortices. Suddenly, it is the smallest vortices that are the strongest ones and they are located at the near wake stagnation point, which rises due to the secondary flow from the cylinder with positive U and the wake back-flow with negative U. The reason for this change of trend can only be speculated upon. An hypothesis is that the change of trend is an artifact of the energy transfer from the primary to the secondary vortices and that they are forced towards the wake centre line when approaching the streamwise extent of the confluence point. These small vortices are pushed away from the cylinder by the surface blowing and pulled towards the cylinder by the wake back-flow, which will lead to a line up of vortices across the wake. Due to the vertical stagnation line the vortices will continuously be fed with new energy in both the positive and the negative rotational directions, which is the reason why the vortices are mixed between positive and negative circulation.

Acknowledgements

This work is part of the project "Active control of vortex shedding behind bluff bodies", which has been financially supported by the Swedish Research Council (VR). The Göran Gustafsson foundation is also acknowledged for their financial support of this work.

References

Adrian, R. J., Christensen, K. T. & Liu, Z.-C. 2000 Analysis and interpretation of instantaneous turbulent velocity fields. *Exp. Fluids* **19**, 275–290.

Agrawal, A. & Prasad, A. 2002 Properties of vortics in the self-similar turbulent jet. *Exp. Fluids* **33**, 565–577.

Buresti, G. 1998 Vortex shedding from bluff bodies. *Wind Effects on Buildings and Structures,* pp. 61–95, Riera & Davenport (eds.), Balkema, Rotterdam.

Chomaz, J. M., Huerre, P. & Redekopp, L. G. 1988 Bifurcations to local and global modes in spatially developing flows. *Phys. Rev. Lett.* **60**, 25–28.

Chong, M. S., Perry, A. E. & Cantwell, B. J. 1990 A general classification of three-dimensional flow fields. *Phys. Fluids* **2**, 765–777.

Fransson, J. H. M. & Alfredsson, P. H. 2003 On the disturbance growth in an asymptotic suction boundary layer. *J. Fluid. Mech.* **482**, 51–90.

Fransson, J. H. M., Konieczny, P. & Alfredsson, P. H. 2004 Flow around a porous cylinder subject to continous suction or blowing. *Journal of fluids and structures* **19**, 1031–1048.

Gillies, E. A. 1998 Low–dimensional control of the circular cylinder wake. *J. Fluid Mech.* **371**, 157–178.

Glezer, A. & Amitay, M. 2002 Synthetic jets. *Annu. Rev. Fluid Mech.* **34**, 503–529.

Grinstein, F. F., Boris, J. P. & Griffin, O. M. 1991 Passive pressure-drag control in a plane wake. *AIAA J.* **29**, 1436–1442.

Huerre, P. & Monkewitz, P. A. 1990 Local and global instabilities in spatially developing flows. *Annu. Rev. Fluid Mech.* **22**, 473–537.

Hurley, D. G. & Thwaites, M. A. 1951 An experimental investigation of the boundary layer on a porous circular cylinder. *Brit. Aero. Res. Council,* Rep. and Memo. 2829.

Jeong, J. & Hussain, F. 1995 On the identification of a vortex. *J. Fluid. Mech.* **285**, 69–94.

Lindgren, B. 2002 Flow facility design and experimentsl studies of wall-bounded turbulent shear-flows. PhD thesis, Royal Institute of Technology.

Mathelin, L., Bataille, F. & Lallemand, A. 2001*a* Near wake of a circular cylinder submitted to blowing - I Boundary layers evolution. *Int. J. Heat Mass Transf.* **44**, 3701–3708.

Mathelin, L., Bataille, F. & Lallemand, A. 2001*b* Near wake of a circular cylinder submitted to blowing - II Impact on the dynamics. *Int. J. Heat Mass Transf.* **44**, 3709–3719.

Monkewitz, P. A. 1988 The absolute and convective nature of instability in two–dimensional wakes at low Reynolds numbers. *Phys. Fluids* **31**, 999–1006.

Norberg, C. 2003 Fluctuating lift on a circular cylinder: review and new measurements. *J. Fluids Struc.* **17**, 57–96.

Pankhurst, R. C. & Thwaites, M. A. 1950 Experiments on the flow past a porous circular cylinder fitted with a Thwaites flat. *Brit. Aero. Res. Council,* Rep. and Memo. 2787.

Park, D. S., Ladd, D. M. & Hendricks, E. W. 1994 Feedback control of von Karman vortex shedding behind a circular cylinder at low Reynolds numbers. *Phys. Fluids* **6**, 2390–2405.

Provansal, M., Mathis, C. & Boyer, L. 1987 Benard-von Karman instability: transient and forced regimes. *J. Fluid Mech.* **182**, 1–22.

Roshko, A. 1955 On the wake and drag of bluff bodies. *J. Aeronaut. Sci.* **22**, 124–132.

Roshko, A. 1961 Experiments on the flow past a circular cylinder at very high Reynolds number. *J. Fluid Mech.* **10**, 345–356.

Roussopoulos, K. 1993 Feedback control of vortex shedding at low Reynolds number. *J. Fluid Mech.* **248**, 267–296.

Shiels, D. & Leonard, A. 2001 Investigation of a drag reduction on a circular cylinder in rotary oscillation. *J. Fluid Mech.* **431**, 297–322.

Tokumaru, P. T. & Dimotakis, P. E. 1991 Rotary oscillation control of a cylinder wake. *J. Fluid Mech.* **224**, 77–90.

Williamson, C. H. K. 1996 Vortex dynamics in the cylinder wake. *Annu. Rev. Fluid Mech.* **28**, 477–539.

Zdravkovich, M. M. 1997 *Flow around circular cylinders, Vol 1: Fundamentals*. Oxford University Press.

Zdravkovich, M. M. 2003 *Flow around circular cylinders, Vol 2: Applications*. Oxford University Press.

Zhou, J. Adrian, R. J., Balachandar, S. & Kendall, T. M. 1999 Mechanisms for generating coherent packets of hairpin vortices in channel flow. *J. Fluid. Mech.* **387**, 353–396.

2

Paper 2

On the vortex generation behind a passive V-shaped mixer in a pipe flow

By Bengt E. G. Fallenius and Jens H. M. Fransson

Linné Flow Centre, KTH Mechanics, SE-100 44 Stockholm, Sweden

To decrease the emissions from combustion engines an additive may be injected in the exhaust emissions. In order to optimally compound this additive with the exhaust emissions there is a need to create a stirring process, which in the simplest form amounts to placing a vortex generator in the flow. The drawback, at high velocities, may be its form as a noise generator. It is understandable that different means to alter the generation of noise, in a positive way, are sought after. It has been shown that such a positive effect is obtained if the vortex generator itself is allowed to be dynamic, i.e. if the vortex generator is thin enough so that its stiffness is reduced. In the present investigation the effect of flexible versus stiff vortex generators, in a pipe flow, on the fluid dynamics have been studied. It is shown that there are no major changes in the mean velocity field nor the strength, circulation and size of the generated vortices in the pipe. This result suggests that the mixing process is equally rapid for the flexible vortex generator as the stiff one, but with the advantage of having reduced the noise level.

1. Introduction

In an effort to reduce emissions from internal combustion engines, an additive can be injected in the exhaust emissions. To obtain a fast and homogeneous compound, a vortex generator can be installed near the point where the substance is added. An important issue in this context is the side effect of a generated acoustic field due to the presence of the vortex generator. For practical applications there are limitations on the excessive level of noise being generated, so there is an interest to keep the acoustic field as weak as possible. It has been shown that by allowing the introduced mixer to be flexible one can influence the acoustic source-strength in a positive way (see Karlsson *et al.* 2008). With this result in mind there is obviously an interest to study the effect of flexible vortex generators on the mixing process itself. In the present paper a direct comparison of the generated fluid structures between a stiff and a flexible vortex generator is made. The differences are quantified by means of

small-scale flow structure changes and mean velocity profile changes between a stiff and a flexible vortex generator. Here, we denote this type of vortex generator as a passive mixer since it does not cost any energy to perform the actual mixing, apart from the increased pressure drop in the pipe.

The paper has the following outline. Section 2 describes the experimental setup, the V-shaped vortex generators and the measurement technique. This is followed by a brief summary of the vortex detection program that has been used for the collection of the vortex statistics (section 3). The results are shown in section 4 and the summary and conclusions are found in section 5.

2. Experimental setup and measurement technique

The experiments were performed in the MWL[1] pipe flow facilitiy, which is an open facility mainly used for studies on aeroacoustics. The centre line velocity in the pipe was $U_C = 50$ m s^{-1} in all the measurements performed.

Figure 1 shows two photographs of the experimental setup. The pipe test section is made of plexiglas (a) with a length of 1496 mm and is located 3880 mm downstream of the pipe facility contraction. Downstream of the test section the pipe continues with an extension of 3560 mm. The inner diameter of the pipe is $D = 90$ mm and the wall thickness is 5 mm. At approximately 400 mm downstream of the test section entrance, the vortex generator was mounted through a slit through the pipe wall at an angle of 32° and clamped by a holder attached around the pipe (b). This is illustrated in figure 2 where a sketch of the geometry is shown with the coordinate system and the placement of the plate in the pipe in (a) together with the entire test section and a photograph of the actual vortex generator in (b) and (c), respectively. Two wedge-shaped vortex generators with varying thicknesses, t, and hence different stiffnesses, were studied. Apart from the thicknesses of $t = 3.0$ and 0.5 mm, from here on denoted the stiff and the flexible vortex generator, respectively, they were identical.

A two-dimensional Particle Image Velocimetry (PIV) system was used for the velocity measurements in the pipe. The laser beam from a Spectra Physics 400 mJ double pulsed Nd:Yag laser (shown in figure 1c), operating at 15 Hz, was mirrored to the cylindrical lens (d) creating a laser sheet. A screen (e) was used to reduce reflections and images were taken using a double-frame Kodak ES1.0 8-bit CCD camera (f), with a resolution of 1018×1008 pixels. For the calibration of the PIV-images, a calibration plate (g) was placed in front of the pipe and then removed. After calibration the laser sheet and the camera was moved to the centre line of the pipe by means of a manual traversing table (h).

The PIV-measurements were performed at four x/D-locations, namely, at $-3,\ 3,\ 6$ and 9 in both the xy–plane and the xz–plane (cf. figure 2).

[1]Marcus Wallenberg Laboratory

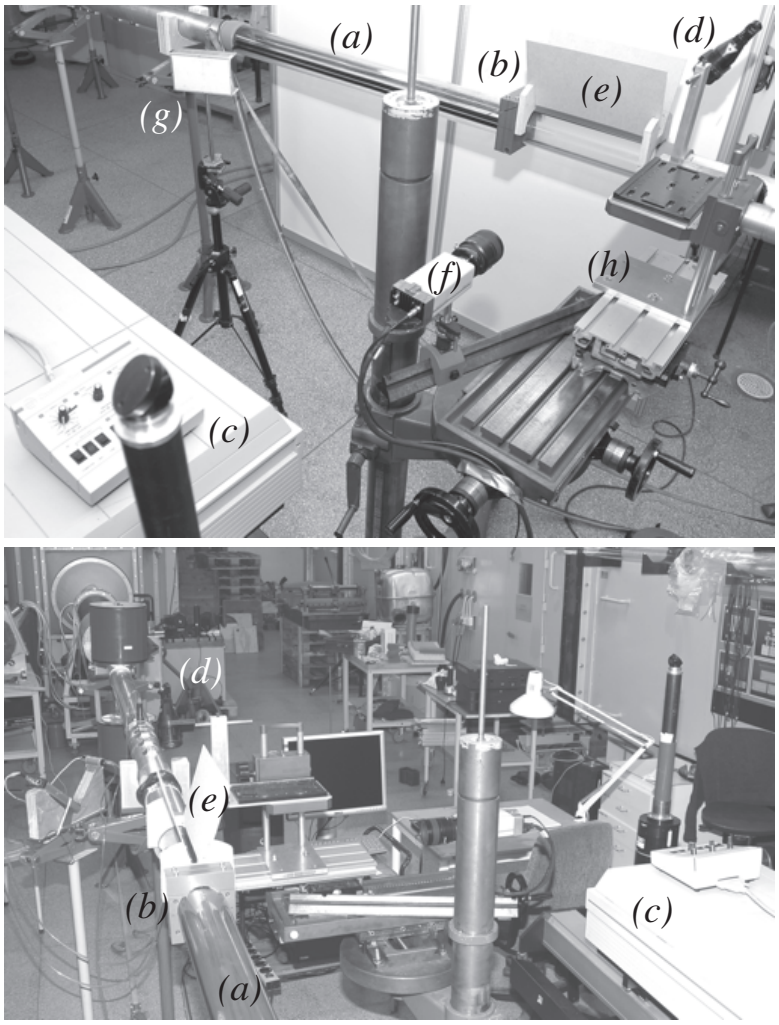

FIGURE 1. Photographs of the experimental setup. The test section (a), the vortex generator (b). The laser beam was mirrored from (c) to the cylindrical lens (d), and a screen (e) was used to reduce the reflections. The camera (f), calibration plate (g) and traversing (h).

Smoke particles, generated by heating a glycol based liquid with a disco smoke generator (JEM ZR20 Mk II), were used to seed the air and the smoke was injected through 5 hoses connected to the contraction (iv) of the pipe apparatus. The injection of smoke into the pipe was achieved by placing the smoke machine inside a pressurised chamber (cf. figure 3). This pressure chamber was regulated via a control valve (i) and the pressure difference between the pipe at the injection location and the chamber was adjusted for suitable smoke density for the captured PIV images using a pressure differential meter (ii). An absolute pressure meter (iii) in the chamber was also used in order to make sure that the pressure did not exceed the chamber specifications.

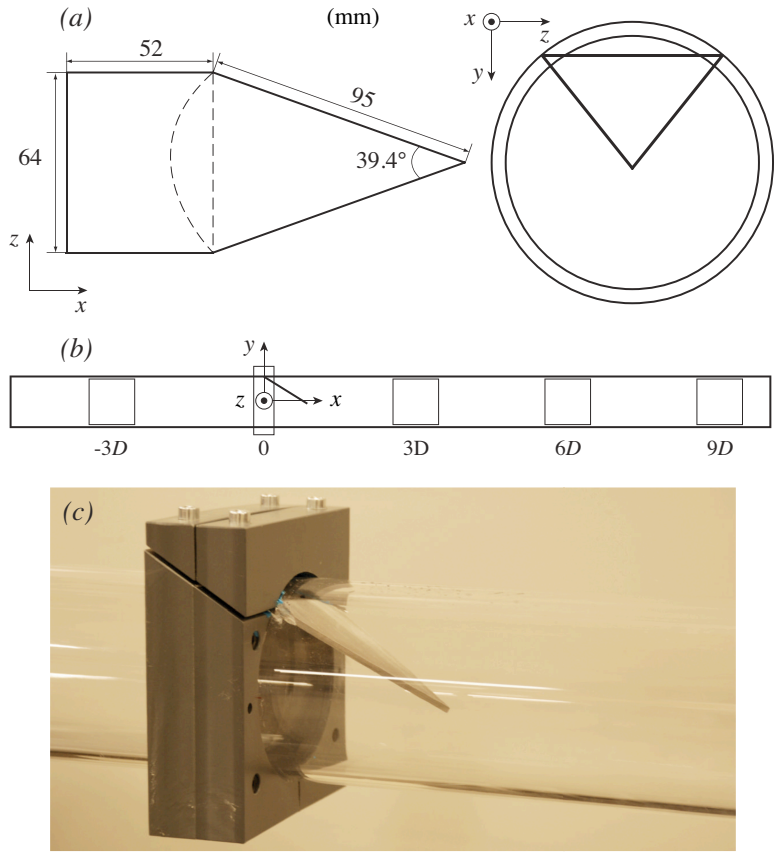

FIGURE 2. (*a*) The wedge-shaped vortex generator in the xz–plane and the position of the vortex generator in the yz–plane of the pipe. (*b*) and (*c*) show the test section in the xy–plane and a real photograph of the vortex generator, respectively.

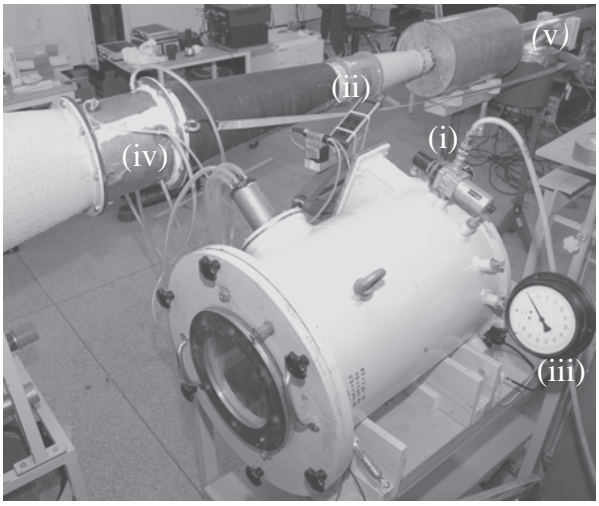

FIGURE 3. The pressurised chamber with (i) a pressure regulator, (ii) a differential pressure meter, (iii) absolute pressure meter. The smoke where injected in the contraction (iv) upstream of the pipe (v).

In order to find out whether the vortex generators were deflected by the flow or not, a Photron APX-RS high-speed camera, with the frame rate set to 3 kHz at a resolution of 1024×128 pixels, was used to capture the movement of the plates.

3. Identification of vortices

The vortex identification algorithm that has been used is similar to the one suggested by Adrian *et al.* (2000), i.e. small scale structures in an instantaneous two-dimensional velocity field is revealed by high-pass filtering. Vortices are identified by finding regions in the high-pass filtered velocity field where the velocity gradient tensor have imaginary eigenvalues, λ_{ci}, implying that the streamlines are closed or spiral, see Chong *et al.* (1990). Each region is then examined and properties of the identified vortices are stored for post-processing and statistical comparisons. A threshold for λ_{ci} has to be implemented to have distinct and reasonable boundaries of the vortices. The threshold in this study was chosen by studying contours for different values of λ_{ci} in the high-pass filtered velocity field. The value was after studying the outcome set to $\lambda_{ci} = 250$.

The high-pass filtering is carried out by convolving a Gaussian filter on the full velocity field $\mathbf{u}$, which results in a low-pass filtered velocity field $\bar{\mathbf{u}}$. The high-pass filtered velocity field is then obtained by subtracting the low-pass

filtered velocity field from the full velocity field, according to

$$\mathbf{u}'' = \mathbf{u} - \bar{\mathbf{u}} \ . \tag{1}$$

The low-pass filter is written as,

$$\bar{\mathbf{u}}(m,n) = \frac{\sum_{j=-k}^{k}\sum_{i=-k}^{k} g(i,j)\mathbf{u}(m-i,n-j)}{\sum_{j=-k}^{k}\sum_{i=-k}^{k} g(i,j)} \ , \tag{2}$$

where (i,j) is the step in x and y, respectively, and k is the *radius*. Note here that the shape of the filter is square, and hence, the radius is the number of surrounding grid-points in each direction that are averaged with the point (m,n).

The Gaussian kernel (g) is defined as

$$g(i,j) = \exp\left[-\frac{(i\Delta x)^2 + (j\Delta y)^2}{2\sigma^2}\right] \ , \tag{3}$$

where Δx and Δy are the grid spacing and σ is the padding of the filter. Here, the parameters k and σ were chosen by counting the number of vortices for varying values of k and σ, as well as different λ_{ci}. For $k = 5$ and $\sigma = 5$, there where no major change in the number of vortices.

The vortex parameters that are stored are the vortex core position, strength, size and circulation. The centre of the vortex is taken to be the highest λ_{ci} in each region. According to Zhou *et al.* (1999), the value of the highest λ_{ci} also corresponds to the vortex strength. The size of the vortex is determined by finding the radius for the maximum circulation γ, which is calculated according to

$$\gamma = \oint_C \mathbf{u}'' \cdot d\mathbf{l} \ , \tag{4}$$

where $\mathbf{l}$ is the perimeter of the circle C around the vortex centre, which is stepwise increased in size until the maximum value of γ is found.

4. Experimental results

PIV-measurements were performed in both the xy- and the xz-plane (cf. figure 2(a)). A typical image pair of the PIV-measurements is shown in figure 4. As seen in the images, a strong reflection is present in the lower part, which affected the quality of the captured velocity fields. From a mean velocity point of view only some of the points had to be disregarded. However, for the detection and analysis of the small-scale structures, the influence of the reflections on the results was larger, and consequently parts of the velocity field had to

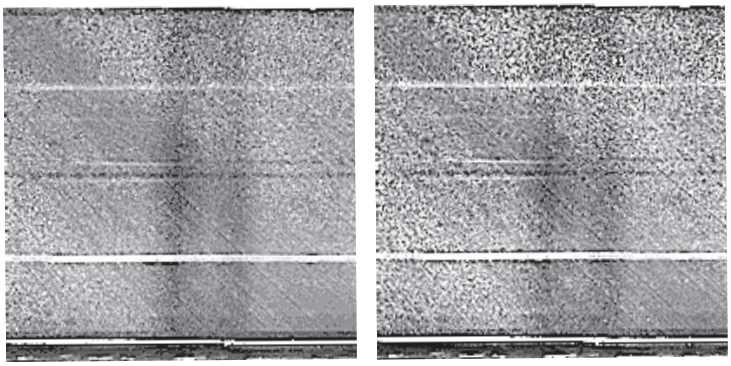

FIGURE 4. A (left) and B (right) images of a raw data image pair from the PIV-measurements at $x = 6D \pm 0.5D$ with the 3.0 mm vortex generator. The flow is from left to right.

Plane		xy		xz	
x-pos	t [mm]	no. of IP	no. of vortices	no. of IP	no. of vortices
$3D$	0.5	1024	27271	1024	20840
	3.0	1024	30343	1024	21661
$6D$	0.5	1056	15275	992	10916
	3.0	1088	14703	1056	10426
$9D$	0.5	1024	8283	800	6286
	3.0	1024	9653	1024	8413

TABLE 1. The number of PIV-image pairs (IP) taken during the experiments and the number of vortices identified in each plane and for the two different vortex generators.

be cut out. Due to the reflections the intervals $-0.12D \leq y \leq 0.42D$ and $-0.42 \leq z \leq 0$ in the xy–plane and the xz–plane, respectively, were used for vortex identification. The latter was decided to be cut at the centreline du to the symmetry of the geomtery.

Table 1 shows the number of image pairs (IP) the statistical results have been based on, and the number of vortices that were detected in the reduced velocity fields. In the table one can see that the number of vortices decreases along the pipe in the downstream direction.

The vibrations and maximum deflection of the plates were recorded with the high speed camera. The 3 mm vortex generator showed no noticeable deflection, while the 0.5 mm vortex generator had a static deflection of approximately 4 mm and oscillated with an amplitude in the order of the plate

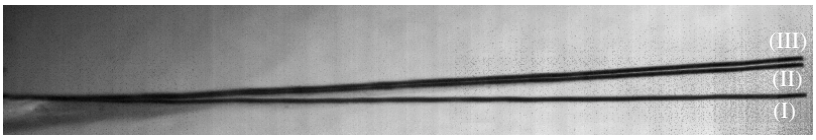

FIGURE 5. The position without any flow (I) of the 0.5 mm plate. (II) and (III) are the maximum negative and the maximum positive deflections of the oscillations, respectively.

thickness. This is shown in figure 5, where position (I) shows the plate without any flow in the pipe. (II) and (III) correspond to the maximum negative and the maximum positive deflection of the oscillations, respectively, which are caused by the flow. Note, that the image has been rotated so that the reference case without any flow is the horizontal one.

4.1. *Mean velocity profiles*

The upstream flow conditions were characterized at the location $x/D = -3$ from the vortex generator. In figure 6 the mean velocity profile is shown where the no-slip wall condition has been added with bullet symbols. Note that all the velocity profiles shown here are not only time averaged, they are also spatially averaged in the streamwise direction from $-0.5D$ to $0.5D$ from the given x-station. Furthermore, unphysical data points, due to near wall factors and reflections, have been removed in order not to cause confusion. The Reynolds number in the present experiment, based on the pipe diameter and the centre-line velocity, is around 3×10^5. The dashed line, in figure 6, corresponds to the empirical power law equation,

$$\frac{U}{U_C} = \left(\frac{1}{2}\right)^{-1/n} \left(\frac{1}{2} + \frac{y}{D}\right)^{1/n} , \quad -0.5 \leq y/D \leq 0 , \tag{5}$$

with $n = 7$. U/U_c in equation 5 is then mirrored along the centre line to get the profile in the range $0 < y/D \leq 0.5$. The chosen n-value is known to give a good agreement with experimental data in a smooth pipe, at Reynolds numbers on the order of 10^5, apart from the centre line where the two boundary layer profiles meet and give rise to a rather unphysical discontinuity in the profile derivative. In addition, due to the presence of microphones and loudspeakers (used for acoustical measurements in the same setup) as well as duct joints, there are some surface imperfections, which cause a mismatch across the entire profile as shown in figure 6. It is possible to observe that the empirical velocity profile is fuller close to the surface, till $y/D = \pm 0.4$, and less fully elsewhere, when compared with the experimentally measured velocity profile. However, due to the profile crossing around $y/D = \pm 0.4$ the integrated empirical and experimental mean velocity values agree remarkably well with each other. The

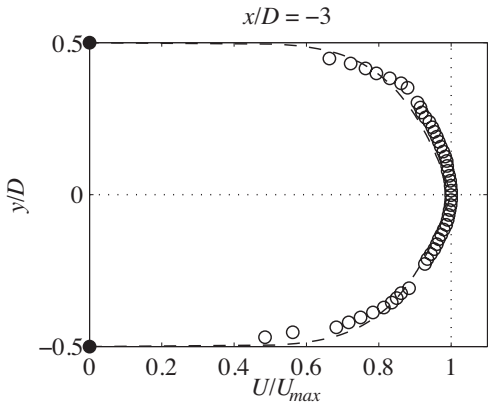

FIGURE 6. Upstream mean velocity profile at $x/D = -3$. Symbols correspond to the measured profile and the dashed line corresponds to the power law, eq. 5, with $n = 7$. Bullets are added data points fulfilling the no-slip condition.

calculated Mach numbers, based on the mean velocity, for both the empirical and the experimental cases become 0.12.

In figure 7 the effect of the 0.5 and the 3 mm thick vortex generators on the velocity field is compared for three different downstream stations. The xy and xz–planes (see figure 2) are shown in the first and in the second column of subfigures, respectively, in figure 7. The velocity profiles have been normalized with the maximum velocity of the two planes across the pipe. In the xy–plane an asymmetric mean velocity distribution is expected due to the accelerated and retarded flow on the bottom and the top side, respectively. The retardation is an effect of the direct blockage of the vortex generator and the acceleration on the bottom is the compensation. The vortex generator can be seen as a wing with a low pressure on the lee- side and a high pressure on the oncoming flow-side. This pressure difference induces strong and steady vortices for small to moderate angles of attack, which become unsteady for higher angles of attack or for flexible and vibrating wings where vortex shedding become the dominating flow phenomenon. These vortices complicate the flow description from a mean velocity point of view. However, the main conclusion drawn from figure 7 is that there is hardly any difference of the mean velocity distribution between the two different plates. Furthermore, a comparison between the xy and the xz–planes at $x/D = 9$ does hardly show any indication of an upstream located vortex generator since the velocity distribution seems to be more or less axi-symmetric. The xz–plane, as expected, shows a symmetric velocity distribution across the pipe. Maybe less expected is how remarkably well the two different velocity profiles agree with each other.

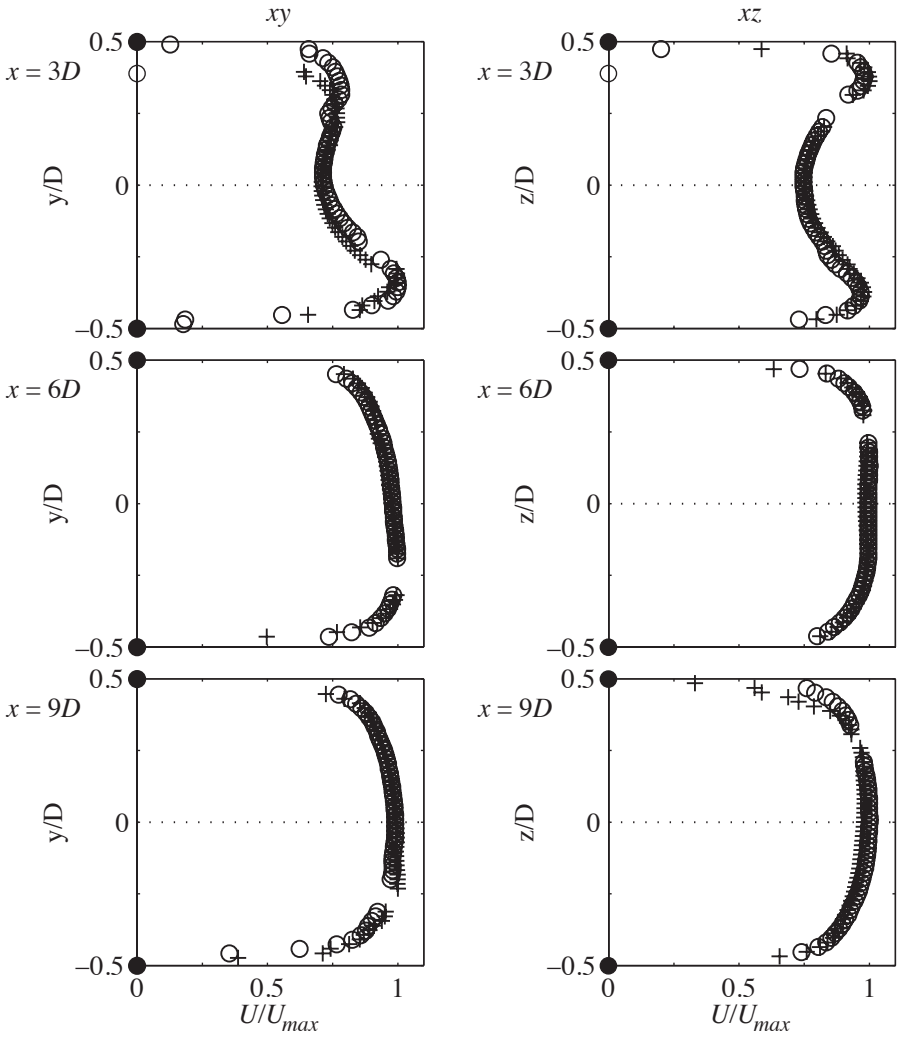

FIGURE 7. Mean velocity profiles of for the two planes at different positions. (+) and (∘) is the 0.5 mm and 3 mm plate, respectively. The bullets represents the no-slip condition.

4.2. *Vortex properties*

In figure 8 typical instantaneous high pass filtered velocity fields from the xy–plane and the xz–plane are shown for both the 0.5 and the 3.0 mm vortex generators. These fields reveal the smaller structures embedded in their corresponding mean velocity fields and are shown here in order to emphasize the fact that no major flow structure changes are detected between the 0.5 and the 3.0 mm plates. This view is strengthened by looking at the statistics of the vortex parameters, namely, the vortex strength, size and circulation. In this subsection the small differences will be highlighted and discussed.

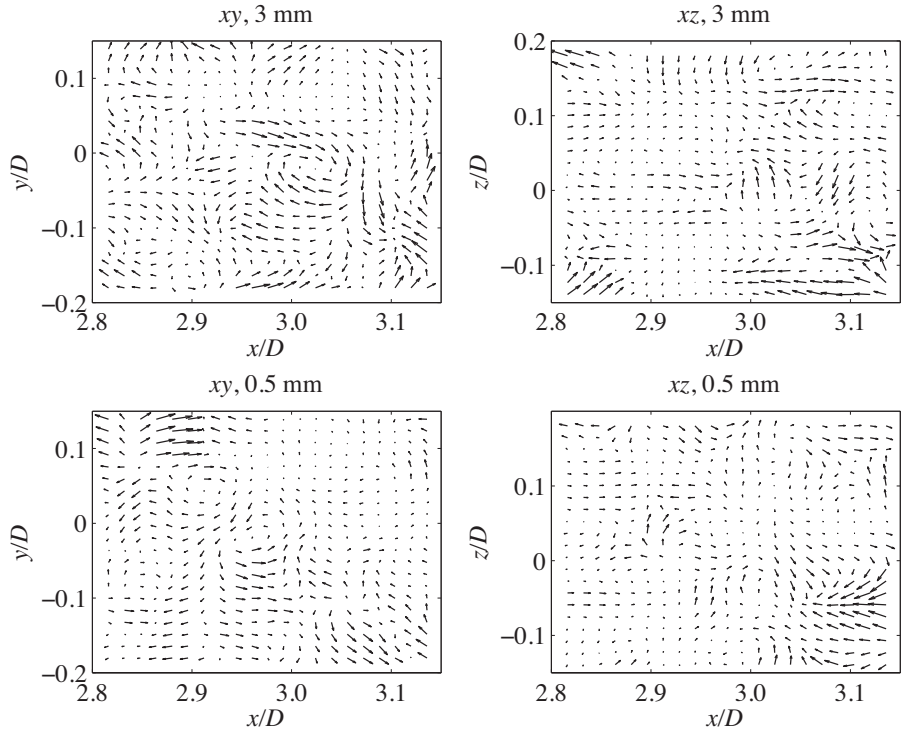

FIGURE 8. Typical instantaneous velocity vector plots for both the xy–plane and the xz-plane. These planes are shown for both the 0.5 and the 3.0 mm vortex generators in the first and second rows of the subfigures, respectively.

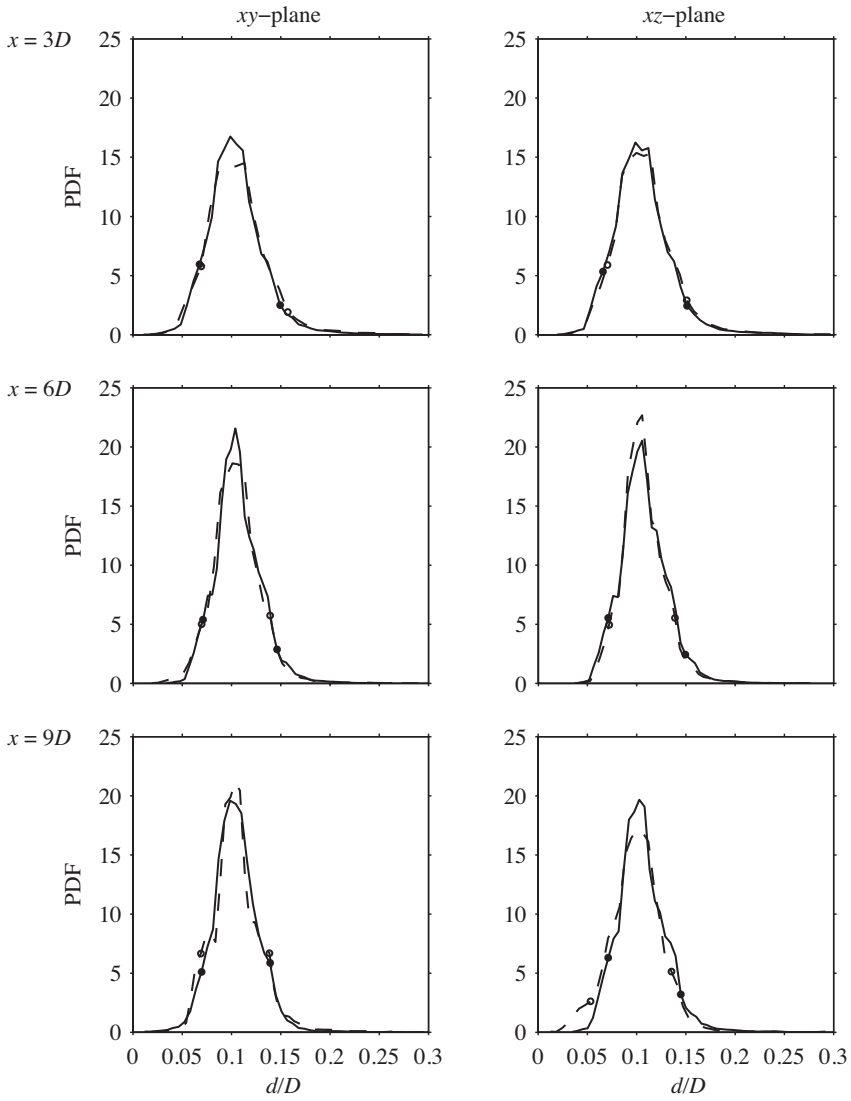

FIGURE 9. The diameter range of the vortices. Dashed and solid lines represent the 0.5 and the 3.0 mm vortex generator, respectively. The lowest and highest 5% of the parameter value for the 0.5 and the 3.0 mm vortex generator are marked by (○)– and (●)–symbols, respectively.

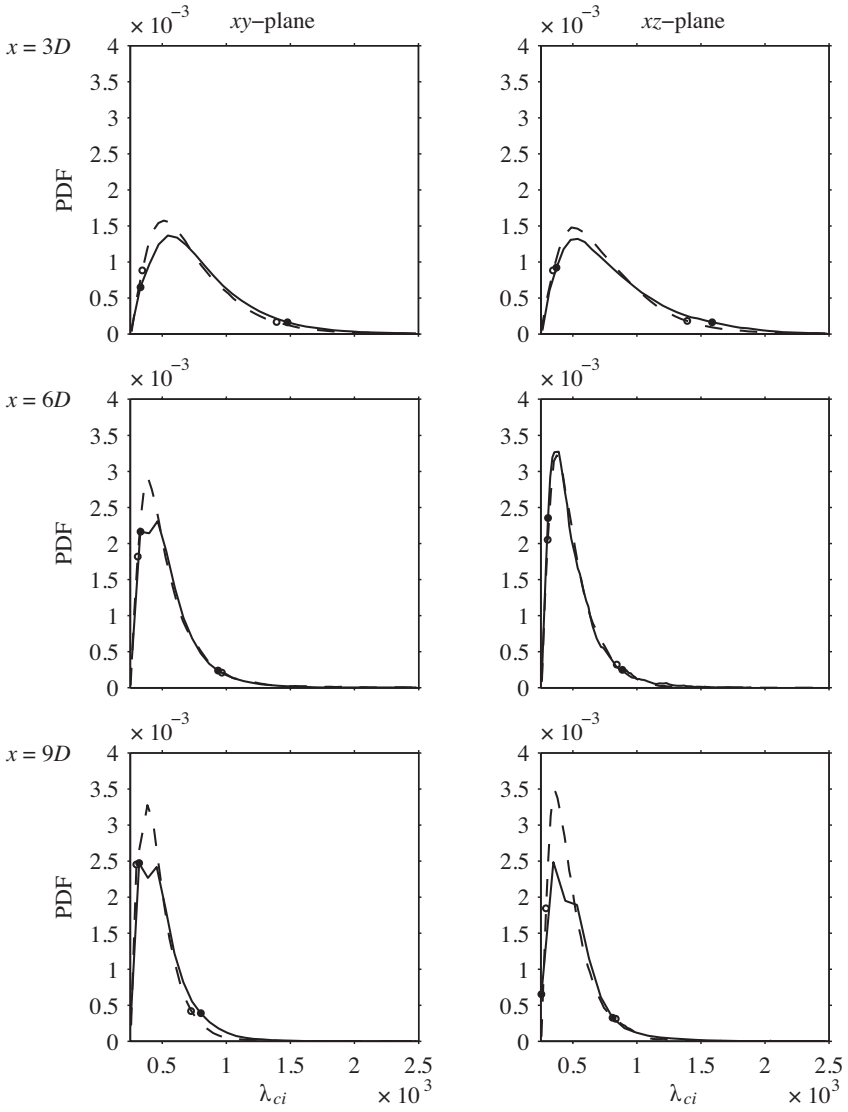

FIGURE 10. The strength range of the vortices. Dashed and solid lines represent the 0.5 and the 3.0 mm vortex generator, respectively. The lowest and highest 5% of the parameter value for the 0.5 and the 3.0 mm vortex generator are marked by (∘)– and (•)–symbols, respectively.

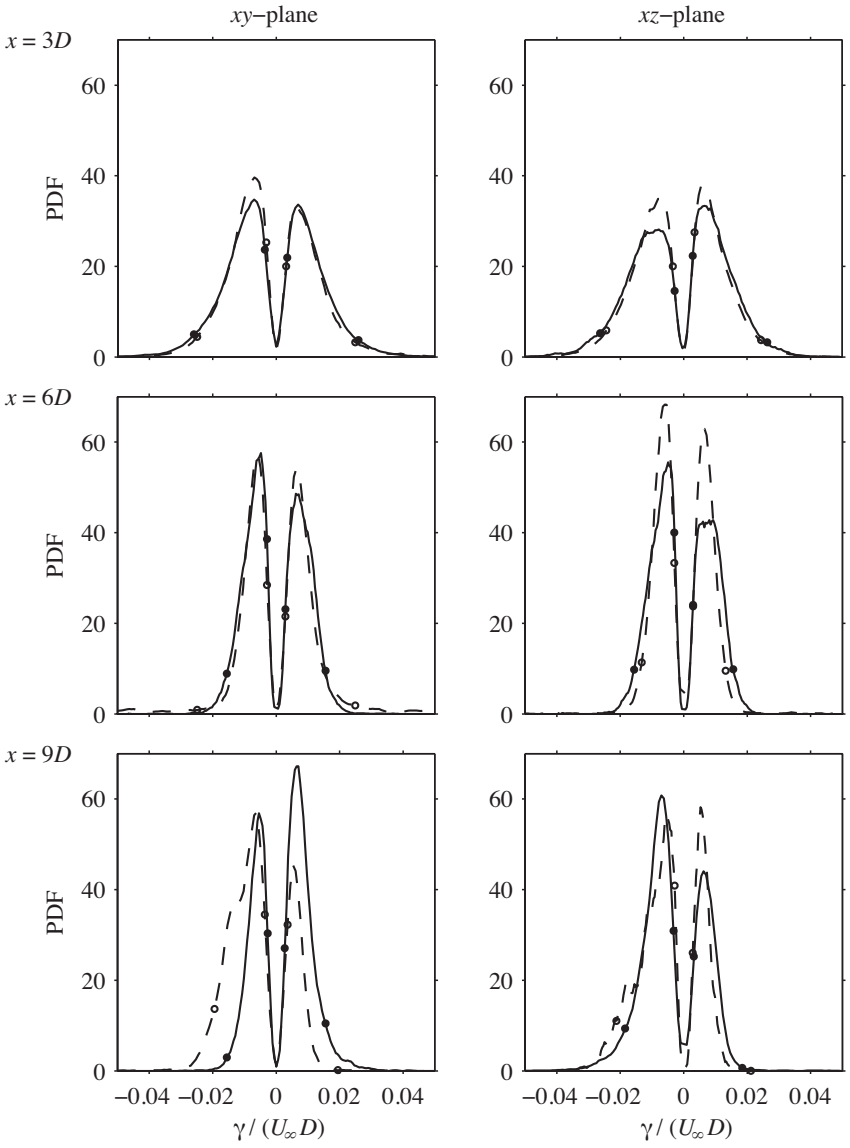

FIGURE 11. The circulation range of the vortices. Dashed and solid lines represent the 0.5 and the 3.0 mm vortex generator, respectively. The lowest and highest 5% of the parameter value for the 0.5 and the 3.0 mm vortex generator are marked by (○)– and (●)–symbols, respectively.

Figure 9 shows the streamwise evolution of the Probability Density Functions (PDFs) of the vortex strength for the two different vortex generator thicknesses as well as for the two different measurement planes. Dashed (with (•)–symbols) and solid (with (○)–symbols) lines correspond to the 0.5 and the 3.0 mm vortex generator, respectively. The symbols indicate the lowest and highest 5% of the parameter value. Note, that the PDFs have been normalized such that the area under the curves equal unity. This means that PDF height differences are also relevant to be compared. Figure 9 shows that the most common vortex diameter essentially stays constant around $0.1D$, independent of the the vortex generator thickness, the plane considered, or the downstream distance. The latter is a confirmation that the finally analyzed area of the velocity field, after the cut out due to reflections, is large enough since the PDFs in the xy–plane and the xz–plane are similar to each other. The number of detected vortices is however reduced in the downstream distance (cf. table 1), which they should since the vortices lose strength through viscous dissipation. The range of vortex diameters of significant relevance, i.e. within the 5% smallest and 5% largest vortices, is in average $0.07 \lesssim d/D \lesssim 0.14$.

In figure 10 the PDFs of the vortex strength is shown in the same way as in figure 9. For the xy–plane and the most upstream location ($x/D = 3$) one may observe a small shift of the PDF, corresponding to the 0.5 mm thick vortex generator, towards lower vortex strengths when compared with the stiff vortex generator. However, already at the next downstream location the most common vortex strength is the same for the two vortex generator thicknesses. At the most upstream location it is clear that the number of strong vortices is larger compared to the $x/D = 6$ and 9 locations. One may conclude that the fastest decay of vortex intensity take place right after the position of generation, which is in line with general knowledge about streamwise vortex evolution and the exponential decay of the vortex strength (see e.g. Lögdberg *et al.* 2009).

The circulation (γ) is also a measure of the vortex strength, as just discussed in relation to figure 9, but its sign also gives information about the rotational direction of the vortex. Positive and negative circulations correspond to counter clockwise (CCW) and clockwise (CW) rotational directions, respectively. In figure 11 the PDFs of the vortex circulation, normalized by $U_\infty D$, are plotted in the same way as in figures 9 and 10. Here, one may observe that the most common vortex strength is independent of the rotational direction, since the peak locations on the $\gamma/(U_\infty D)$ axis does not change. It should be mentioned that there is an asymmetric distribution of positive and negative vortices, but, which most likely is attributed to small misalignments when setting up the PIV image frames to be captured. This can also explain the most downstream location ($x/D = 9$) of the xy–plane, where the deviation is largest when comparing the flexible and the stiff vortex generators.

5. Summary and conclusions

In an effort to reduce emissions from internal combustion engines, an additive can be injected in the exhaust emissions. To enhance the mixing a vortex generator can be installed, however such a device can also be a source of acoustic noise. Recent results have shown that flexible vortex generators may reduce the level of noise compared to stiff ones. In the present paper a direct comparison of the generated fluid structures between a stiff and a flexible vortex generator in a pipe is made. The differences are quantified by means of small-scale flow structure changes and mean velocity profile changes between a stiff and a flexible vortex generator.

The vortex generator can be seen as a wing with a low pressure on the lee-side and a high pressure on the oncoming flow-side. This pressure difference induces strong and steady vortices for small to moderate angles of attack, which become unsteady for higher angles of attack or for flexible and vibrating wings where vortex shedding become the dominating flow phenomenon. These vortices complicate the flow description from a mean velocity point of view. However, the main conclusion drawn is that there is hardly any difference of the mean velocity distribution between the two different vortex generators.

The vortex size is set by the dimensions of the vortex generator, i.e. a physically small vortex generator will generate small vortices and *vice versa*. Since the size of the vortex generator is the same between the 0.5 and the 3.0 mm thicknesses the generated vortex diameter range was not expected to be significantly changed. However, the vortex strength seems to be somewhat affected by the flexibility of the 0.5 mm vortex generator thickness. This is revealed in a small shift of the PDF, corresponding to the 0.5 mm thick vortex generator, towards lower vortex strengths when compared with the stiff vortex generator.

It is shown that there are no major changes in the mean velocity field nor the strength, circulation and size of the generated vortices in the pipe. This result suggests that the mixing process is equally rapid for the flexible vortex generator as the stiff one, but with the advantage of having reduced the noise level.

Acknowledgements

We would like to thank Prof. Mats Åbom and Mikael Karlsson for hosting us and giving us running time in the MWL pipe flow facility. Andreas Holmberg at the Marcus Wallenberg Laboratory is acknowledged for his assistance during the actual PIV experiments and for running the pipe flow facilitly. The MWL technicians Kent Lindgren and Danilo Prelevic have been invaluable for the experimental setup. Furthermore, the authors would like to thank the Swedish Research Council, VR, for their financial support under grant number 621-2005-5757. The Göran Gustafsson foundation is also acknowledged.

References

Adrian, R. J., Christensen, K. T. & Liu, Z.-C. 2000 Analysis and interpretation of instantaneous turbulent velocity fields. *Exp. Fluids* **19**, 275–290.

Chong, M. S., Perry, A. E. & Cantwell, B. J. 1990 A general classification of three-dimensional flow fields. *Phys. Fluids* **2**, 765–777.

Karlsson, M., Holmberg, A., Fallenius, B. E. G., Franson, J. H. M. & Åbom, M. 2008 Experimental determination of the aero-acoustic properties of an in-duct flexible plate. *AIAA Paper 2008–3057, 14th AIAA/CEAS Aeroacoustic Conference* .

Lögdberg, O., Fransson, J. H. M. & Alfredsson, P. H. 2009 Streamwise evolution of longitudinal vortices in a turbulent boundary layer. *J. Fluid Mech.* **623**, 27–58.

Zhou, J. Adrian, R. J., Balachandar, S. & Kendall, T. M. 1999 Mechanisms for generating coherent packets of hairpin vortices in channel flow. *J. Fluid. Mech.* **387**, 353–396.